Phytoplankton Dynamics in the Subarctic Northeast Pacific Ocean During the 2019 Marine Heatwave

by

Sile Kafrissen

B.Sc. Honours, University of Victoria, 2019

A Thesis Submitted in Partial Fulfillment
of the Requirements for the Degree of

MASTER OF SCIENCE
in the School of Earth and Ocean Sciences

University of Victoria

We acknowledge and respect the lək^{w}əŋən peoples on whose traditional territory the university stands and the Songhees, Esquimalt and W̱SÁNEĆ peoples whose historical relationships with the land continue to this day.

Phytoplankton Dynamics in the Subarctic Northeast Pacific Ocean During the 2019 Marine Heatwave

by

Sile Kafrissen

B.Sc. Honours, University of Victoria, 2019

Supervisory Committee

Dr. Diana E. Varela, Supervisor

School of Earth and Ocean Sciences

Dr. John Dower, Departmental Member

School of Earth and Ocean Sciences

Dr. Rana El-Sabaawi, Outside Member

Department of Biology

Abstract

Marine phytoplankton are responsible for nearly 50% of all the primary productivity on Earth, and their response to climate change and anomalous climatic events impacts biogeochemical cycling. During the summer of 2019, the NE Pacific Ocean experienced a warming event that caused sea surface temperature anomalies of up to 4 °C. These types of events, called marine heatwaves (MHW), are becoming more common globally but their effects on pelagic primary producers are not yet well understood. In September 2018 and August-September 2019, temperature, salinity, nutrient concentrations, primary producer biomass, and uptake rates of carbon (ρC) and nitrogen (ρNO_3) were measured along the Line P transect in the NE Pacific. Additionally, in August-September 2019, nitrate (NO_3) and silicon (Si) uptake kinetic experiments were performed at five Line P stations in addition to five stations on the west coast of Vancouver Island to assess potential physiological limitation in phytoplankton from NO_3 and Si. In 2019, temperatures in the euphotic zone along Line P were higher and the water column was more stratified at all stations than in 2018. Concentrations of dissolved NO_3 and silicic acid ($Si(OH)_4$) were anomalously low in 2019 and nutrient depletion extended approximately 500 km further offshore than in 2018. The Line P station closer to the shelf (P4) had a considerable reduction in chlorophyll-a (chl-a), biogenic silica ($bSiO_2$) and the contribution of diatoms to the entire phytoplankton assemblage. From P4 to P20, the assemblage was dominated by small-celled phytoplankton (<5 um) in both years, but there was a relative increase in 2019. There were particularly unusual observations at the most oceanic station (P26) where the contribution of diatoms, concentrations of chl-a and $bSiO_2$, and ρC, and ρNO_3 were anomalously high in 2019 compared to regional averages. In 2019, the uptake of $Si(OH)_4$

appeared to be substrate limited at the majority of stations while only station CS02 on the west coast of Vancouver Island appeared to have physiological limitation by NO_3. Based on Michaelis-Menten uptake kinetics, half saturation constants (K_m) ranged from 0.01-0.13 for NO_3 and 2.33-18.3 for $Si(OH)_4$, suggesting that assemblages are less efficient at Si uptake than NO_3 uptake in the NE Pacific. Results from this study are consistent with observations from the other warming anomalies including the 2015 “blob” and the 1997/1998 ENSO event in the NE Pacific Ocean. The similarities observed during these ocean warming events suggest that phytoplankton in the NE subarctic Pacific may become increasingly susceptible to nutrient limitation, particularly from $Si(OH)_4$, with increased stratification. Future investigations should focus on co-limitation studies of Fe and $Si(OH)_4$, uptake rates of regenerated nitrogen sources, timing of bloom onsets, total annual biomass and trophic interactions with zooplankton during MHW events.

Table of Contents

List of Tables

List of Figures

Acknowledgments

First, I would like to thank my supervisor, Diana Varela, for the many opportunities and the guidance that she has provided for me. The last seven years working in her research lab have shaped my career path and the trajectory of my life. Thank you to my committee members John Dower and Rana El-Sabaawi for being patient, helpful, and supportive during my research.

I would like to thank all members of the Varela Lab who assisted with field work, sample collection and processing including Michael Livingston, Brandon McNabb, Shea Wyatt, Rebecca Crawford, and Olivia Melville. A special thanks to Karina Giesbrecht who mentored me in the lab for my first years in oceanographic research and continued to be a support for many years during my research.

The collection of samples would not have been possible without the help of numerous scientists at the Institute of Ocean Sciences who assisted in the collection of my samples and provided many helpful ancillary data for this thesis. In particular, thanks to Marie Robert, Mike Arychuck, Mark Belton, Akash Sastri, Moira Galbraith, Hugh Maclean, and Ian Perry who helped organize and facilitate cruises and were helpful and instructive watch leaders. Additional thanks to the captain and crew of the CCGS John P Tully who assisted in sample collection and kept us safe at sea. Special thanks to James Watling, Spencer Webber, Max Knight, Shauna Quinsey, Jonny Gardner, Kevin Cyr, Hannah Hollyoak, and Mike Carere. Thank you for being the best Tully crew and even better friends to me over the past four years.

During my time at UVic there were many friends and colleagues who supported me both in my research and personal life. Thank you to Robyn Taves for being my number one supporter and for being the best bunk mate at sea. Thank you to Matt Miller, Brett Jameson, Moronke Harris, and Camille Giuliano for providing enlightening conversation about my research and helping me to continue on in my studies.

Without the support of my family I would not have been able to pursue my degree. Thank you to my parents Clare Dwyer and Erik Kafrissen, my step mother Liseanne Cadieux, and my siblings Kai, Bridie, and Isaiah. A special thanks to James Watling, who not only supported me through my degree but through the many losses that occurred during my research.

Lastly, I would like to acknowledge the funding sources for my degree. My research has been supported by the Natural Sciences and Engineering Research Council (NSERC) Discovery Grant awarded to Diana Varela. I also received funding from the University of Victoria in the form of a University of Victoria fellowship.

Chapter 1: General Introduction

1.1 A brief overview of phytoplankton physiology

Most aspects of our lives are linked to primary productivity. Terrestrial, aquatic and marine autotrophs are responsible for the air we breathe, the materials we use to build our houses, and the food we eat; even the fuel that powers our cities, industries and cars is derived from their remains (Falkowski et al., 2003). Of these primary producers, marine phytoplankton are an integral and critical part of global systems, influencing the atmosphere, lithosphere, and biosphere and accounting for about 50% of the global oxygen production and carbon (C) uptake (Field et al., 1998). Primary production by phytoplankton is estimated to support nearly 50% of global population via fisheries production (Hollowed et al., 2013). Phytoplankton are comprised of about 20,000 described species in 8 phyla but among the more common groups are Diatoms (Bacillariophyceae), Dinoflagellates (Dinophyceae), Cyanobacteria (Cyanophyceae), Silicoflagellates (Dictyochales) and Coccolithophores (Coccolithophyceae). Within and among the groups, there are variations in growth rates, nutrient requirements, life cycles, ecosystem function, size and stoichiometric relationships (Bonachela et al., 2016; Falkowski, 1994).

Like plants, all phytoplankton require a suite of basic nutrients and other inorganic constituents to grow, and may become limited if any of these essential nutrients become depleted. Liebig's Law of Minimum can be applied to phytoplankton and states that growth will be limited by the nutrient that is most depleted in an ecosystem (Bristow et al., 2017) but this principle becomes more complex when we examine the functions and uptake mechanisms of these nutrients. Macronutrients such as carbon (C), nitrogen (N) and phosphate (PO_4^{3-}) are required in relatively large quantities to build organic molecules while other micronutrients, such

as iron (Fe), zinc (Zn) and cadmium (Cd), are important for physiological processes related to C and N uptake (Baeyens et al., 2018) but are generally needed in trace amounts. Fe, for example, is required for the synthesis of chlorophyll as well as multiple electron transport proteins involved in CO_2 reduction (Street & Paytan, 2005). Sufficient concentrations of both micro and macronutrients are important for facilitating phytoplankton growth and need to be considered when addressing nutrient dynamics. In areas where micronutrients, such as Fe, do not limit growth, they often do not noticeably influence the chemistry and structure of phytoplankton blooms, and these assemblages are influenced more by the availability of macronutrients. When micronutrients are limiting, they often have a dramatic effect on physiological processes that influence the assemblage composition and rates of primary productivity (Greene et al., 2003; Hutchins & Bruland, 1998).

When micro or macronutrients are limiting, or are present at very low concentrations, smaller celled phytoplankton tend to dominate the assemblages as they have a competitive advantage over large-celled phytoplankton under these conditions. Due to the larger surface area to volume ratio, small-celled phytoplankton can, on average, more efficiently acquire nutrients than larg- celled phytoplankton (Shuter, 1978; Hein et al., 1995). When assemblages are dominated by small picoplankton (<2 μm), the majority of nutrient regeneration and cycling happens within the microbial loop and energy transfer to higher trophic levels is lower (Finkel et al., 2010; Pomeroy, 1974). Picoplankton-dominated assemblages can also result in a weakening of C sequestration in deep waters via the biological pump (Finkel et al., 2010; Pomeroy, 1974). Decreasing body size has been proposed as a universal trend of global warming (Gardner et al., 2011; Yvon-Durocher et al., 2011) and may result in smaller celled phytoplankton assemblages, due to competitive advantages of smaller species.

The requirement of C, N, and P is ubiquitous; all phytoplankton need them in order to grow. However, some phytoplankton have specific requirements for additional macronutrients. One of the most abundant groups, diatoms, require silicon (Si) to form their siliceous shells, called frustules. Diatoms take up Si from the surrounding water in the form of silicic acid ($Si(OH)_4$) and deposit it in the form of biogenic silica or biogenic opal ($bSiO_2$) (Kroger & Poulsen, 2008). Diatoms tend to dominate $bSiO_2$ precipitation in the waters of marine ecosystems (Hildebrand, 2003; P. Tréguer et al., 1995) and therefore, examining marine $bSiO_2$ production and cycling can be used as a proxy to specifically investigate diatom processes and their contributions to an ecosystem. Since diatoms tend to be large and heavy, due to their SiO_2 frustules, the growth and proliferation of diatoms can lead to ecosystem effects such as higher C and Si export.

Phytoplankton have complex photosynthetic systems that are influenced by temperature, pH and light availability. Two of the most important enzymes involved in photosynthesis are nitrate reductase (NR) which is important for the uptake of NO_3 (Beevers & Hageman, 1969), and ribulose bisphosphate carboxylase-oxygenase (RuBisCO) which is responsible for CO_2 uptake (Wildman, 2002). The function of these two enzymes will impact the uptake and kinetic efficiency of phytoplankton assemblages. These enzymes have complex interactions with the environment and other physiological processes and can show a high level of diversity in the catalytic efficiency between phytoplankton groups (Coyne et al., 2021; Helbling et al., 2011; Lomas & Glibert, 2000; Young et al., 2016). While both enzymes have been observed to have increased activity with increasing temperature, they also compete with one another for reductant (electrons) created during photosynthesis. So, while a phytoplankton cell may be subjected to increased substrate and temperature, C or NO_3 uptake (and growth) may still be light limited.

These varied physiological and biogeochemical interactions that influence phytoplankton productivity make it complicated to answer questions about how productivity will be impacted by environmental changes. Experimentation and observation should be used simultaneously along with a suite of ancillary measurements when attempting to understand changes in phytoplankton dynamics in global ocean systems.

1.2 Diatoms in the subarctic northeast Pacific Ocean

Diatoms are a successful and prolific group of phytoplankton that account for about 20% of the world's primary productivity, link the biogeochemical cycles of C, N and Si, and dominate many high productivity ecosystems, such as the coastal Northeast (NE) Pacific Ocean and the Western subarctic Pacific (Malviya et al., 2016; Nelson David M. et al., 2012; Obayashi et al., 2001; P. Tréguer et al., 1995; Tréguer & De La Rocha, 2013). Diatoms play an important role in global C export and sequestration as their large, heavy, mineral frustules sink relatively rapidly and can lend ballast to aggregations and fecal pellets (Allen et al., 2005; Baines et al., 2010; Ducklow et al., 2001; Kemp et al., 2000; Smetacek et al., 2012). Although they require relatively large amounts of Si to grow, they have been shown to exhibit extreme flexibility in their extent of silicification depending on their environment and nutrient availability (Baines et al., 2010; Hildebrand, 2003). Due to their significant contribution to marine food webs and the biological C pump, investigating diatom's interactions with the environment is important to understand their ecosystem function on both local and global scales.

The oceanic subarctic NE Pacific is considered a high-nutrient low-chlorophyll (HNLC) zone where diatoms are heavily limited by bioavailable Fe and tend to bloom only in late summer once microzooplankton grazing has decreased the numbers of small-celled phytoplankton which are able to outcompete diatoms for any Fe that is available (Zhang et al.,

2021). It has been demonstrated that under Fe limitation, diatoms increase their cellular content of Si which leads to a higher export of Si out of the water column (Hutchins & Bruland, 1998; Mosseri et al., 2008; Takeda, 1998). While the exact mechanisms that cause this increase in silicification are still unknown, there has been evidence that both the cell specific uptake of Si and the half saturation constant may be affected by Fe (Huttchins et al., 1999; De La Rocha et al., 2000; Quéguiner, 2001). Additionally, in HNLC zones such as the subarctic NE Pacific, diatoms may even become co-limited by Fe and Si (Brzezinski et al., 2022; Dugdale et al., 1995) and should be termed high-nitrate low-silicate low-chlorophyll zones (HNLSLC). In these areas, the extent to which Si may limit diatom growth is important to investigate, particularly in the context of a changing ocean.

1.3 Marine heatwaves

As climate change progresses, ocean waters around the world are warming and becoming more stratified (IPCC, 2019). As part of this trend, there has been an increase in the frequency and severity of extreme climatic events such as marine heatwaves (MHW) (IPCC, 2012). MHWs are a phenomenon defined as an anomalously warm event where high temperatures last for more than five days and are within the 90^{th} percentile of the 30-year climatic average for the region (Hobday et al., 2016). Devastating ecological effects of MHWs have been observed around the world, including in the Mediterranean Sea (Garrabou et al., 2009; Marbà & Duarte, 2010), Australia (Benthuysen et al., 2014; Wernberg et al., 2013) and the North Atlantic (Mills et al., 2013). In the last decade, the NE Pacific has experienced MHW events in 2013-2015 and in 2019 (Chen et al., 2021; Di Lorenzo & Mantua, 2016). While physical drivers of these MHWs, as well as their effects on coastal ecosystems, have been investigated in several previous studies (Amaya et al., 2020; Di Lorenzo & Mantua, 2016; Nielsen et al., 2021; Ross et al., 2021; Wyatt et al.,

2022), there is little research about how phytoplankton may be affected. Due to the taxonomical, physiological and functional diversity of phytoplankton, it is very difficult to represent them in ecosystem models and predict how extreme environmental events may affect them (D'Alelio et al., 2016). *In situ* measurements of nutrient concentrations, phytoplankton biomass and taxonomy, and pelagic primary productivity during these MHW events are crucial to our understanding of how phytoplankton assemblages and their production may shift with future climatic changes.

Since the 1950s recurring marine heatwave (MHW) events have been observed in the NE Pacific (Xu et al., 2021). While these events are not unprecedented, the frequency, duration and amplitude of these warming events may be increasing (Xu et al., 2021). Two major MHW events have been recorded in the last decade in the subarctic NE Pacific. In the winter of 2013/2014 warm water masses began to develop in the subarctic Pacific in the path of the North Pacific current (Di Lorenzo & Mantua, 2016). The warm water spread over the Gulf of Alaska and record-breaking sea-surface temperatures (SST) were recorded in the NE Pacific where the anomalies were as high as 4° C (Di Lorenzo & Mantua, 2016; Peña et al., 2019). The warm conditions persisted into the spring of 2015 causing devastating ecological effects, particularly in coastal ecosystems where the physiological stress on animals and plants resulted in failed spawning, and high mortality rates (Bond et al., 2015; Cheung & Frölicher, 2020; Di Lorenzo & Mantua, 2016). This event has since been named "the blob".

The 2015 blob was caused by lower than normal heat loss from the surface waters of the NE Pacific primarily due to atmospheric forcing. Development of an El Niño in 2014/2015 coupled with changes in the Aleutian Low system caused a decrease in the speed of subtropical North-Easterly trade winds. A decrease in NE-W wind activity causes lower than normal heat

loss from the surface ocean, decreases in mixing, and lower evaporation caused by wind activity (Amaya et al., 2020). This atmospheric event is usually a precursor to strong El Niño conditions and can further increase SST in a feedback loop. Evidence of this was seen in sea level pressure (SLP) during this time that appeared to follow patterns of the North Pacific Gyre Oscillation (NPGO) and Pacific Decadal Oscillation (PDO) that often lead to increased ocean temperatures (Bond et al., 2015; Di Lorenzo & Mantua, 2016).

In the summer of 2019, observations of SST and SLP suggested the resurgence of blob-like conditions in the subarctic NE Pacific (Amaya et al., 2020; Chen et al., 2021). An atmospheric ridge developed that weakened the Aleutian Low and associated north-easterly winds. The effects was a decrease in both Ekman transport of cold waters from higher latitudes and surface ocean mixing (Amaya et al., 2020; Bond et al., 2015). Additionally, during 2019, low-altitude cloud fraction was anomalously low for the region which would also increase the insolation received in the surface ocean (Amaya et al., 2020). Once again, SST and SLP anomalies were observed as another marine heatwave began to develop. The 2019 marine heatwave is characterized as a 4-peak heatwave with the first temperature anomaly peak occurring in November 2019, although anomalies began much earlier in the year (Chen et al., 2021). During the summer of 2019, temperatures began to increase, resulting in temperature anomalies up to 4 °C in the NE Pacific (Amaya et al., 2020). While the 2019 MHW seemed to develop in much the same way as the blob, some researchers noted that the ecosystem effects were not nearly as devastating in coastal areas (Ross et al., 2021). However, there has not been significant comparison of the effects on phytoplankton dynamics and assemblages as of yet.

1.4 The subarctic Northeast Pacific Ocean: study site

The studies presented in this thesis took place in the subarctic NE Pacific Ocean during the summer of 2018 and the summer of 2019 in two oceanographic locations; along a transect that runs from SW corner of Vancouver Island to the Alaskan Gyre (Line P program), and along the western coast of Vancouver Island (La Perouse program). In the subarctic NE Pacific, the North Pacific or Subarctic Current flows eastward and bifurcates at approximately the latitude of southern Vancouver Island to become the Alaskan Current (flowing northward) and the California Current (flowing southward). These major currents, and several associated smaller currents dictate most of the physical and chemical oceanography in the region. The Line P transect consists of 26 main oceanographic stations running from the mouth of the Juan de Fuca Strait, off the Coast of Vancouver Island (P1), to Ocean Station Papa (Stn. P or P26) in the Gulf of Alaska (50°N and 145°W) (Freeland, 2007). Station P26 and many of the other offshore stations are considered to be within the Alaska Gyre (AG) system (Figure 1.1). The AG is bounded by the Alaska Current in the east, the Alaskan Stream in the north and west, and by the Subarctic Current to the south (Thomson, 1981).

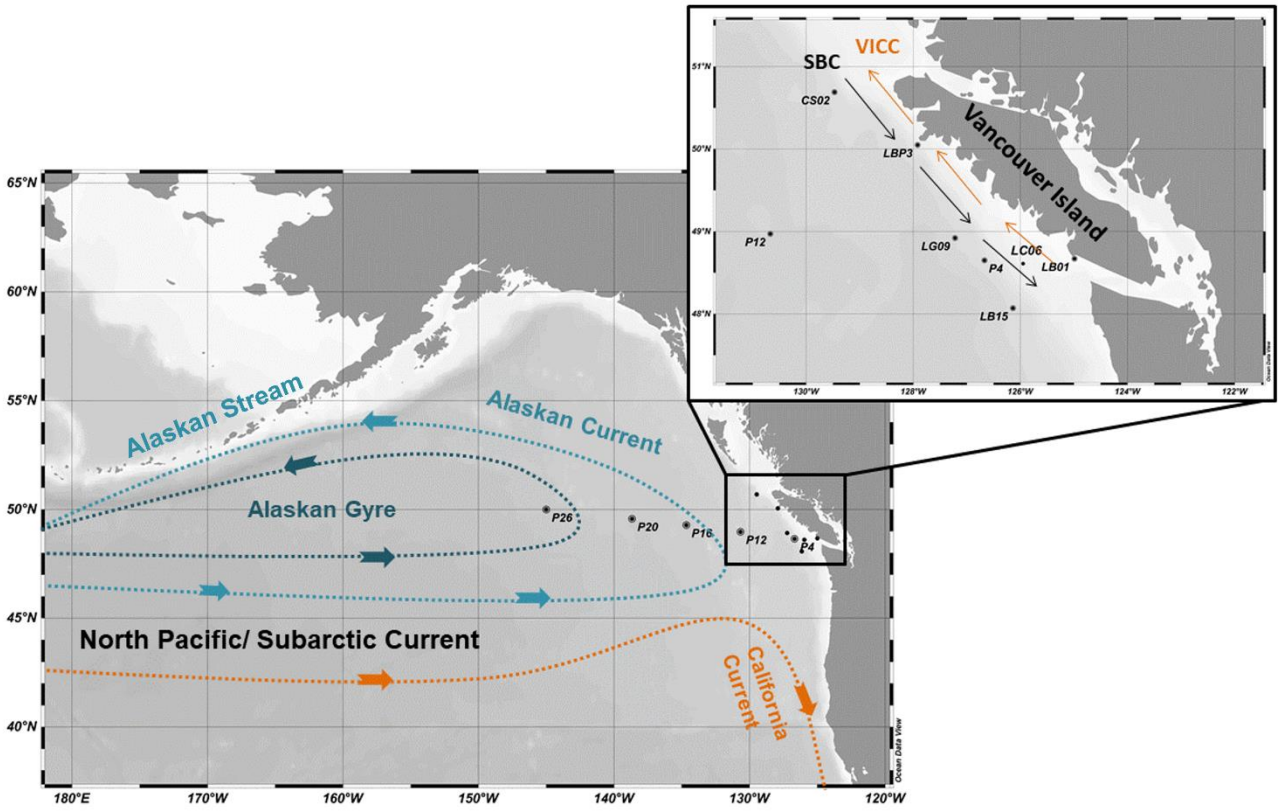

Figure 1.1. Major currents in the subarctic Northeast Pacific and along Vancouver Island (inset). Stations that were sampled during this study along Line P and the west Coast of Vancouver Island are indicated with black circles. In the inset, the currents displayed are the Vancouver Island Coastal Current (VICC) and the Shelf-break Current (SBC).

The AG is highly influenced by local atmospheric forcing. A persistent low pressure system, the Aleutian Low, dominates the area in the winter (building in intensity from about August to January). This low pressure system can lead to both upwelling within the gyre, supplying nutrient-rich waters to the surface, and downwelling in some areas along the North American coastline (Crawford & Thomson, 1991; Gargett, 1991; Thomson, 1981). Additionally, surface runoff in coastal regions and high levels of precipitation in the NE Pacific as a whole result in low surface salinities, a shallow mixed layer, and a shallow well-stratified halocline within the gyre (Tabata, 1975). These conditions can provide the stability that favours an increase in primary productivity, however, limitation from Fe (Martin & Fitzwater, 1988),

coupled with high grazing by zooplankton (P. Boyd et al., 1996; Frost, 1991), result in overall low biomass along most of the offshore portion of the transect (Varela and Harrison 1999, Harrison et al., 1999, Peña & Varela, 2007). Due to Fe limitation, the Subarctic NE Pacific is considered a high-nitrate low-chlorophyll (HNLC) zone where primary producer biomass during the growing season is lower than expected based on nitrate (NO_3) concentrations. Diatom limitation from Si(OH)4 has also been sporadically observed in the gyre (Dugdale & Wilkerson, 1998; Whitney et al., 2005).

There is a strong gradient in chl-a, density, salinity and nutrient concentrations along the Line P transect (Cullen et al., 2009; Ribalet et al., 2010; Roche et al., 1996; Whitney et al., 1998; Wyatt et al., 2022). Stations at the beginning of the transect (near-shore of P4) are located on or very close to the Vancouver Island shelf and are more influenced by coastal processes. Moving seaward, off the shelf (P4-P12), there is an annually persistent zone where Fe-poor, NO_3-rich open-ocean water mixes with Fe-rich, nitrate-poor coastal water (Ribalet et al., 2010). This mixing zone of NO_3 and Fe often leads to growth of small-celled phytoplankton communities (Ribalet et al., 2010) seaward of P4. Seaward of P12, there is a decrease in primary producer biomass and productivity, since phytoplankton become more Fe limited (Roche et al., 1996). From ~P16 onward, Fe is primarily delivered to the stations by atmospheric deposition (Bishop et al., 2002; Hamme et al., 2010) and by nearshore originating mesoscale eddies that can sometimes entrain Fe-rich waters and deliver them to offshore systems (Batten & Crawford, 2005; Brown et al., 2012; Cullen et al., 2009; Lippiatt et al., 2011). These eddies fertilize sections of the NE Pacific NO_3-rich low-Fe open ocean and can, at times, promote higher productivity in offshore environments. However, even with occasional fertilization, stations

seaward of P4 are characterized as having small-cell dominated ecosystems with generally low biomass (Harrison et al., 1999; Peña & Varela, 2007; Varela & Harrison, 1999a).

The southwest coast of Vancouver Island represents the widest part of the western Canadian continental shelf (Crawford & Thomson, 1991). Along the inner shelf, close to the shore there are several dominant deep and surface currents which have seasonal fluctuations, but result in a sustained year-round northward flow (Crawford & Thomson, 1991). Strong bottom currents (~80-100 m depth) flow north/northwest, parallel to the shore, and are part of the northward flowing Davidson Current (or California Undercurrent) (Crawford & Thomson, 1991). There is also a buoyant, surface current, the Vancouver Island Coastal Current (VICC), that runs northward, hugging the coast of southern Vancouver Island (Freeland et al., 1984; Ianson et al., 2003) (Figure 1.1). This current is the result of significant freshwater input from the Juan de Fuca Strait, that creates a horizontal pressure gradient and is influenced by Coriolis forces in such a way that results in a northward flow (Ianson et al., 2003). Overall, these northward flowing waters, originating from surface runoff, are macronutrient and Fe-rich, and are important for fueling productivity along the coast of Vancouver Island. In addition to these prevailing currents, coastal eddies in the summer can have a significant effect on the productivity and surface mixing on the coast by keeping plankton entrained, close to the surface, and by further mixing nutrients into the surface waters (Crawford & Thomson, 1991).

Slightly offshore, along the shelf break, there is a strong surface current (upper ~300 m) which flows southward in the summer and facilitates coastal upwelling in this region (Freeland et al., 1984; Ianson et al., 2003). This “shelf-break” current is driven mainly by the prevailing southward winds in the area, which are associated with the North Pacific High pressure system that dominates in the summer (Figure 1.1). The cold, upwelled, nutrient-rich waters mix with

nutrient and Fe-rich waters from coastal runoff (Cullen et al., 2009; Ribalet et al., 2010) to create perfect conditions for primary producers. Additionally, the wide shelf around Vancouver Island may also facilitate productivity by keeping phytoplankton entrained, and giving blooms time to develop (Hickey & Banas, 2008). These conditions facilitate highly productive ecosystems dominated by large-celled phytoplankton, such as diatoms (Taylor & Haigh, 1996; Harris et al 2009). These coastal stations are also highly influenced by the winter downwelling and summer upwelling that occurs along the Vancouver Island coast (Ianason et al., 2003; Franco et al., 2021). These large scale processes are instrumental in dissolved nutrient delivery to the euphotic zone, deep water ventilation, and mixing of the surface waters.

The productive, diatom-dominated systems of coastal Vancouver Island are in contrast to the Line P transect where primary producers are heavily Fe-limited and under high levels of grazing by microzooplankton. During an extreme event such as a MHW, these systems may be affected very differently due to the differences in physical, chemical and biological oceanographic characteristics. For complex and variable oceanographic zones such as the BC continental margin, spatial and temporal comparisons are both essential to generate a complete picture of ways that systems may shift and how localized changes can influence the overall productivity of the larger system.

1.5 Thesis objectives and organization

To better understand how phytoplankton will be impacted by future climate changes there are two useful avenues of research to be investigated. Firstly, the comparison of data collected during MHW events to long running time series will be the most effective way to assess changes in these systems. However, comparison on shorter timescales (year to year) may also be useful to

recognize more instantaneous changes that may occur while other climate factors are the same. Comparisons to past MHW events or warming periods will be useful here as well. Secondly, the use of novel or under-used methods to assess productivity and physiology of the assemblage during MHWs will be important for understanding the mechanisms that may link changes in environment to changes in productivity or assemblage structure. The goal of this thesis is to examine potential impacts of the 2019 Pacific MHW on phytoplankton biomass and dynamics by comparison to past warming events and by examining phytoplankton dynamics from summers preceding and during a MHW.

Chapter 2 of this thesis examines the differences in primary productivity and biomass, nutrient concentrations and physical water properties throughout the euphotic zone along the Line P transect between a pre-MHW summer (2018) and a summer during a MHW (2019). This chapter uses data collected at the five major Line P stations as well as supplementary rosette and CTD data from all stations along the transect provided publicly by the Department of Fisheries and Oceans.

Chapter 3 presents a spatial study of nitrate (ρNO_3) and Si (ρSi) uptake kinetics during the 2019 MHW and examines the extent of nutrient limitation that may occur during these extreme events. This chapter presents data from a wider spatial study area that includes five oceanographic stations along the western coast of Vancouver Island in addition to the major Line P stations. This chapter focuses on measurements from the mixed layer alone and comparison of spatial differences in the NE Pacific during the 2019 MHW.

Chapter 4 provides general conclusions, based on data from chapters 2 and 3, concerning how pelagic primary producers are impacted by MHW events in the NE Pacific and suggests potential avenues for future research.

Chapter 2: Impacts of the 2019 Pacific marine heatwave on phytoplankton production in the subarctic northeast Pacific.

2.1 Introduction

The Line P program is one of the oldest and most well-established long term oceanographic monitoring programs (Freeland, 2007). The Line P transect runs from the west coast of Vancouver Island to P26 in the Alaskan Gyre, along the way passing through natural gradients in nutrients, temperature, salinity, and water column stability (Whitney et al., 1998; Whitney & Freeland, 1999) that lead to varying levels of primary production and biomass (Obayashi et al., 2001; Peña & Varela, 2007; Varela & Harrison, 1999). While near-shelf of P4, there can be high rates of productivity fueled by large-celled diatoms, the majority of the stations are characterized by small-celled assemblages and low primary productivity due to Fe limitation (Peña & Varela, 2007; Roche et al., 1996; Varela & Harrison, 1999). While some near-shore stations may become macronutrient limited in late summer, productivity along the oceanic part of the transect is mainly controlled by supply of Fe, grazing by microzooplankton, and light availability (Landry et al., 1993; Peña & Varela, 2007; Roche et al., 1996; Varela & Harrison, 1999; Whitney & Freeland, 1999). Most macronutrients do not usually fall below limiting concentrations due do abundant wind-fueled mixing and lower biological drawdown (Boyd et al., 1996; Martin & Fitzwater, 1988; Whitney & Freeland, 1999).

In 2019, the NE Pacific experienced a four-peak MHW that resulted in temperature anomalies of up to 4 °C (Amaya et al., 2020; Chen et al., 2021). MHW events such as this one are becoming more frequent as climate change progresses (Barkhordarian et al., 2022; Oliver et al., 2019; Ross et al., 2021) and their impacts on primary producers will be important to address

to understand the potential changes that may occur in these large marine systems. Often, MHWs are triggered by a decrease in wind activity that leads to warmer and more stratified water columns and a resulting decrease in nutrients delivered to the euphotic zone (Amaya et al., 2020; Barkhordarian et al., 2022; Bond et al., 2015; Di Lorenzo & Mantua, 2016). In large areas of the ocean, where nutrients are usually replete, these decreases in available nutrients during MHWs will impact primary producers. Globally, there have been many proposed effects of warming oceans including reduction in average phytoplankton cell size, decrease in overall primary productivity, increase in regenerated primary productivity, decreased in dissolved nutrient concentrations, and changes in seasonal timing of plankton production (Laffoley & Baxter, 2016). However, locally, these effects are important and may vary depending on the oceanographic setting and the ecological interactions of the native species.

In September of 2018 and August of 2019, physical properties of the water column, dissolved nutrients, primary producer biomass, and rates of productivity were measured along Line P to examine the differences during a pre-MHW summer (2018) and a MHW summer (2019). Comparisons are also made to historical MHWs to understand possible effects of increased ocean warming in the Subarctic NE Pacific.

2.2 Materials and Methods

2.2.1 Sampling and hydrography

Sampling during September 2018 and August 2019 was conducted aboard the CCGS John P Tully using a conventional rosette system equipped with 24 ten-litre Niskin bottles and a SeaBird SBE 911-Plus conductivity, temperature, depth (CTD) probe equipped with

photosynthetically active radiation (PAR) and oxygen sensors. Sampling was conducted at five major stations along the transect (Table 2.1; Figure 1.1).

Table 2.1. Names, locations, sampling dates and physical characteristics for Line P stations sampled in September 2018 and August 2019.

Station	**Latitude**	**Longitude**	**Date Sampled**	**Bottom Depth**	**Chl-a Max Depth**	**Mixed Layer Depth**
	N	W	DD-MM-YY	m	m	m
P4	48.65	126.67	14-09-18	1300	15	16
			16-08-19		37	19
P12	48.97	130.67	15-09-18	3300	5	43
			17-08-19		39	18
P16	49.28	134.67	16-09-18	3550	40*	26
			19-08-19		34	21
P20	49.57	138.67	18-09-18	3890	25*	28
			20-08-19		39	23
P26	50.00	145.00	21-09-18	4300	5*	33
			24-08-19		35	29

* indicates stations that had approximately uniform chl-a concentrations throughout the mixed layer.

During the 2018 cruise, six “light” depths were sampled within the euphotic zone corresponding to 100, 50, 30, 15, 1 and 0.1% of the surface PAR.During the 2019 cruise, samples were only taken from the 50% light depth and the chlorophyll-a (chl-a) maximum. The 50% depth usually corresponded to about 5 m below the surface, and was representative of

phytoplankton assemblages in the mixed layer. The chl-a max depth was normally between 1-15% light depths. All sampling depths are included in Appendix I (Table A1).

All receiving containers and bottles were acid cleaned and rinsed three times with seawater prior to filling from the Niskin bottles. Seawater samples were processed immediately after collection and stored properly until analysis after the cruise.

For this study, the measurements of salinity, temperature, density Sigma-t (σ_t), pressure/depth, and PAR were obtained from the CTD. The mixed layer depth (MLD) was defined as the depth at which the difference in σ_t (kg m^{-3}) was ≥ 0.125 in comparison to the surface value (Levitus et al., 1982).

2.2.2 Dissolved nutrient concentrations

At each depth, in both 2018 and 2019, seawater samples were collected for NO_3^-, PO_4^{3-}, and Si(OH)4 concentrations. For NO_3^- and PO_4^{3-}, triplicate water samples (15 mL) were syringe-filtered through a combusted 0.7 µm (nominal porosity) glass-fibre filter into acid washed, 15-mL polypropylene centrifuge tubes and immediately frozen at -20 ˚C until analysis back in the UVic laboratory. Samples for $Si(OH)_4$ were syringe filtered through a 0.6 µm polycarbonate filter into acid washed, 15-mL polypropylene centrifuge tubes and stored at 4 ˚C until analysis at UVic. Concentrations of NO_3^- and PO_4^{3-} were determined using an Astoria Nutrient Autoanalyzer (Astori-Pacific, OR, USA) following the methodology outlined by Barwell-Clarke & Whitney (1996). Concentrations of $Si(OH)_4$ were determined using the manual molybdate blue colorimetric method described by Brzezinski & Nelson (1986). The limits of detection (LoD) for NO_3^-, PO_4^{3-}, and $Si(OH)_4$ were 0.1, 0.03, and 0.3 µM respectively.

In 2018, additional samples were collected for the measurement of dissolved ammonium (NH_4^+) and dissolved urea. Triplicate samples (50 mL) for analysis of urea were syringe filtered through

a combusted 0.7 µm (nominal porosity) glass-fibre filter into acid washed, 50-mL polypropylene centrifuge tubes and immediately frozen until analysis at UVic. Urea samples were analyzed colorimetrically following the diacetylmonoxime procedure (Mulvenna & Savidge, 1992). For the measurement of NH_4^+, triplicate seawater samples were collected directly into 50 mL glass culture tubes and analyzed immediately on the ship following the fluorometric method set forth by Holmes et al. (1999). Dissolved urea and ammonium data are presented in Appendix I.

2.2.3 Chlorophyll-a concentrations

In 2018 and 2019, seawater samples for total chl-a analysis (250-500 mL) were gently vacuum filtered onto 0.7 µm (nominal porosity) glass-fiber filters, placed in foil envelopes and stored, in the dark at -20˚C until analysis at UVic. Chl-a concentrations were determined using the acetone extraction and acidification method (Strickland & Parsons, 1972; Yentsch & Menzel, 1963).

Fluorescence of the acetone solution containing the extracted chl-a was measured before and after acidification with 1.2 N hydrochloric acid on a Turner 10-AU fluorometer. The concentrations of total chl-a were calculated from the measurements made before (Fo) and after (Fa) acidification using equation (1). The coefficient (τ) of equation (2.1) was derived from a calibration of the Turner 10-AU fluorometer with known pure chl-a standards from *Anacystis nidulans*.

$$\text{Chl} - \text{a}\ (\mu g L^{-1}) = \frac{\tau}{\tau - 1} * (\text{Fo} - \text{Fa}\ ) * 0.814 * \left(\frac{\text{Vol.Acetone extracted}}{\text{Vol.Seawater filtered}}\right) \qquad (2.1)$$

Samples were always extracted into 10 mL acetone (Vol. Acetone extracted) and working coefficients were τ= 2.038 in 2018 and 1.998 in 2019.

For the measurement of size-fractionated chl-a, separate seawater samples of 250-500 mL were filtered consecutively through a 20 µm polycarbonate membrane filter, a 5 µm

polycarbonate membrane filter and then through a 0.7 µm (nominal porosity) glass fibre filter. All three filters were stored at -20° C until analysis at UVic. Samples were analyzed following the same procedure as total chl-a. In this thesis, results from the >20 µm size fraction and the 20-5 µm size fraction were combined and presented as one >5 µm size fraction. Individual data from the size fractions are presented in Appendix I (Table A3).

2.2.4 Biogenic silica concentrations

In 2018 and 2019, triplicate seawater samples for the measurement of $bSiO_2$ (0.5-1 L) were gently vacuum filtered onto 0.6 µm polycarbonate membrane filters. Filters were folded, placed in foil envelopes, and stored at -20° C until analysis at UVic. At UVic, filters were placed in 15 mL polycarbonate centrifuge tubes and dried for 48 hours at 60° C. Material on filters was digested with 4 mL of 0.2 M NaOH for 30-45 min in a water bath at 95 ˚C (Brzezinski & Nelson, 1995). After digestion, samples were neutralized with 0.1 N HCl and cooled rapidly in an ice bath. Samples were centrifuged to separate out undigested lithogenic SiO_2, and colorimetric analysis of $bSiO_2$ was performed on the supernatant. The transmittance of the samples, standards, and reverse-order reagent blanks were read at 820 nm using a Beckman DU 530 ultraviolet-visible (UV/Vis) spectrophotometer (Brzezinski & Nelson, 1989, 1995).

2.2.5 Particulate carbon and nitrogen concentrations

In 2018 and 2019, measurements for particulate carbon (PC) and nitrogen (PN) were obtained from samples incubated for nitrate (ρNO3) and carbon (ρC) uptake rates (see section 2.2.6 below). Therefore, the particulate measurements presented here are from after the 24-h incubation period but ambient particulate C and N concentrations can be back-calculated by subtracting the total uptake of C or NO_3 from the corresponding particulate value. The

differences between after-incubation PC and PN data and back-calculated ambient values were not significantly different (<9 %) than the measurement error for PC (CV=4.13%) and PN (CV=8.1%).

2.2.6 Carbon and nitrogen uptake rates

In 2018 and 2019, seawater from each depth was collected into acid washed, clear, 1 L polycarbonate bottles. To each of the bottles, stable isotopic tracers of $Na^{15}NO_3$ (98+% ^{15}N purity, Cambridge Isotope Laboratories) and $NaH^{13}CO_3$ (99% ^{13}C purity, Cambridge Isotope Laboratories) were added to achieve approximately 10% of ambient NO_3 and dissolved inorganic carbon (DIC) concentrations (or limit of detection). Bottles were placed in a shipboard incubator with seawater flow to maintain constant surface seawater temperature. The incubator was equipped with acrylic tubes wrapped in neutral density, coloured photo-film that achieved the same light quantity and quality from where the samples were collected. The 1-L sample bottles were placed into the appropriate light-depth tube and incubated for 24 hr. After incubation, samples were gently vacuum filtered directly onto combusted 0.7 (nominal porosity) glass fiber filters and stored at -20 °C until processing at UVic. One additional 1 L sample was collected from each station and was used as the "blank" sample. This sample was also spiked with stable isotopic tracers to achieve 10% ambient NO_3^- and DIC but was not incubated and was immediately filtered after addition. The "blank" samples provided natural isotopic values of ^{13}C and ^{15}N used in the calculation of uptake rates.

At UVic, all samples were dried at 60 °C for 48 h and packed into foil pellet for analysis at the Stable Isotope Facility at University of California Davis. Analyses were performed for ^{13}C and ^{15}N enrichment, and total C and N content by continuous flow isotope ratio mass spectrometry and elemental analysis, respectively. To perform these analyses, UC Davis uses

either an Elementar Vario EL Cube or a Micro Cube elemental analyzer (Elementar Analysensysteme GmbH, Hanau, Germany) interfaced to either a PDZ Europa 20-20 isotope ratio mass spectrometer (Sercon Ltd., Cheshire, UK) or an Isoprime VisION IRMS (Elementar UK Ltd, Cheadle, UK). NO_3 uptake (ρNO_3) rates were calculated using equations (3) and (6) of Dugdale & Wilkerson (1986). C uptake (ρC) rates were calculated using equation (6) of Hama et al. (1983).

In 2018, additional experiments were conducted to measure ammonium (ρNH_4^+) and urea nitrogen (ρUrea-N -N) uptake at the 5 major stations along Line P. Sample collection and incubation for all six light-depths was conducted following the same procedures as ρNO_3^- but bottles were spiked with either $^{15}NH_4^+$ ($^{15}NH_4Cl$, 99+% ^{15}N purity, Cambridge Isotope Laboratories) or ^{15}N-Urea ($CH_4{}^{15}N_2O$, 98+% ^{15}N purity, Cambridge Isotope Laboratories). Samples were spiked with an aliquot of either isotope to achieve 10% atom enrichment or the limit of detection (approximately 0.1 µM when ambient values were at or below the limit of detection). Samples for ρNH_4^+ and ρUrea-N were filtered and processed following the same procedure outlined for ρNO_3^- and samples were sent to UC Davis for analysis using isotope ratio mass spectrometry. Full data for ρNH_4^+ and ρUrea-N are included in Appendix I (Table A4) but not discussed in this chapter.

The *f*-ratio represents the proportion of primary production that was derived from NO_3^- (i.e. new productivity) and was calculated differently in 2018 and 2019. In 2018, the measurements of ρNH_4 and ρUrea-N allowed for the calculation of the *f*-ratio based on all N forms following equation (2.2):

$$f\text{-ratio} = \rho NO_3 / (\rho NO_3^- + \rho NH_4^+ + \rho\text{Urea-N}) \qquad (2.2)$$

In 2019, because ρNH_4^+ and ρUrea-N were not measured, the f-ratio was calculated using only ρNO_3 and ρC following equation (2.3):

$$f\text{-ratio} = (\rho NO_3 * C{:}N) / \rho C \qquad (2.3)$$

Where C:N represents the particulate C to N ratio measured for each sample (not Redfield). For both 2018 and 2019, *f*-ratios were calculated using the depth-integrated uptake rates and therefore only one value was available for each station.

2.3 Results

Here I present a comparison of water-column physical characteristics, and phytoplankton and nutrient data for the different stations between the 2018 pre-MHW year and the 2019 MHW year. Samples were collected from the five main stations along Line P: P4, P12, P16, P20, and P26. However, for temperature, salinity, and dissolved nutrients additional publicly available data from the Department of Fisheries and Oceans Institute of Ocean Sciences are combined with data collected for this thesis to provide a more complete picture of water column characteristics throughout the entire Line P transect from P1 to P26.

In the results section, both PC and ρC are presented in units of µg to facilitate easier literature comparison. Both parameters are also presented in terms of µmol in Appendix I (Table A4).

2.3.1 Temperature and salinity

The mixed layer depth (MLD) along Line P was much less variable between stations in 2019 than in 2018 (Table 2.1). The average MLD for Line P was 29 ± 9.7 m in 2018 and 22 ± 3.8 m in 2019. In 2018, mixed layer temperatures were between ~12-16.6 °C for the entire transect and followed a general longitudinal trend of lower temperatures at P4, increasing temperatures toward P12 where the maximum was observed, followed by decreasing

temperatures between ~P16-P26 (Figure 2.1). The highest temperature was recorded at the surface of P12, at 16.6 °C. Over the entire transect, salinity was between 32.25-33.75 PSU in the upper 200 m (Figure 2.1).

During 2019, temperatures in the mixed layer were generally higher than in 2018 and the maximum temperature, 17.9 °C, was recorded at P4, rather than at P12 as in 2018. In 2019, the maximum temperatures within the mixed layer were higher than 2018 at all stations (Figure 2.1 A, B). Additionally, in 2019, landward of P12, lower salinity was measured in the upper ~100 m when compared to 2018 (Figure 2.1).

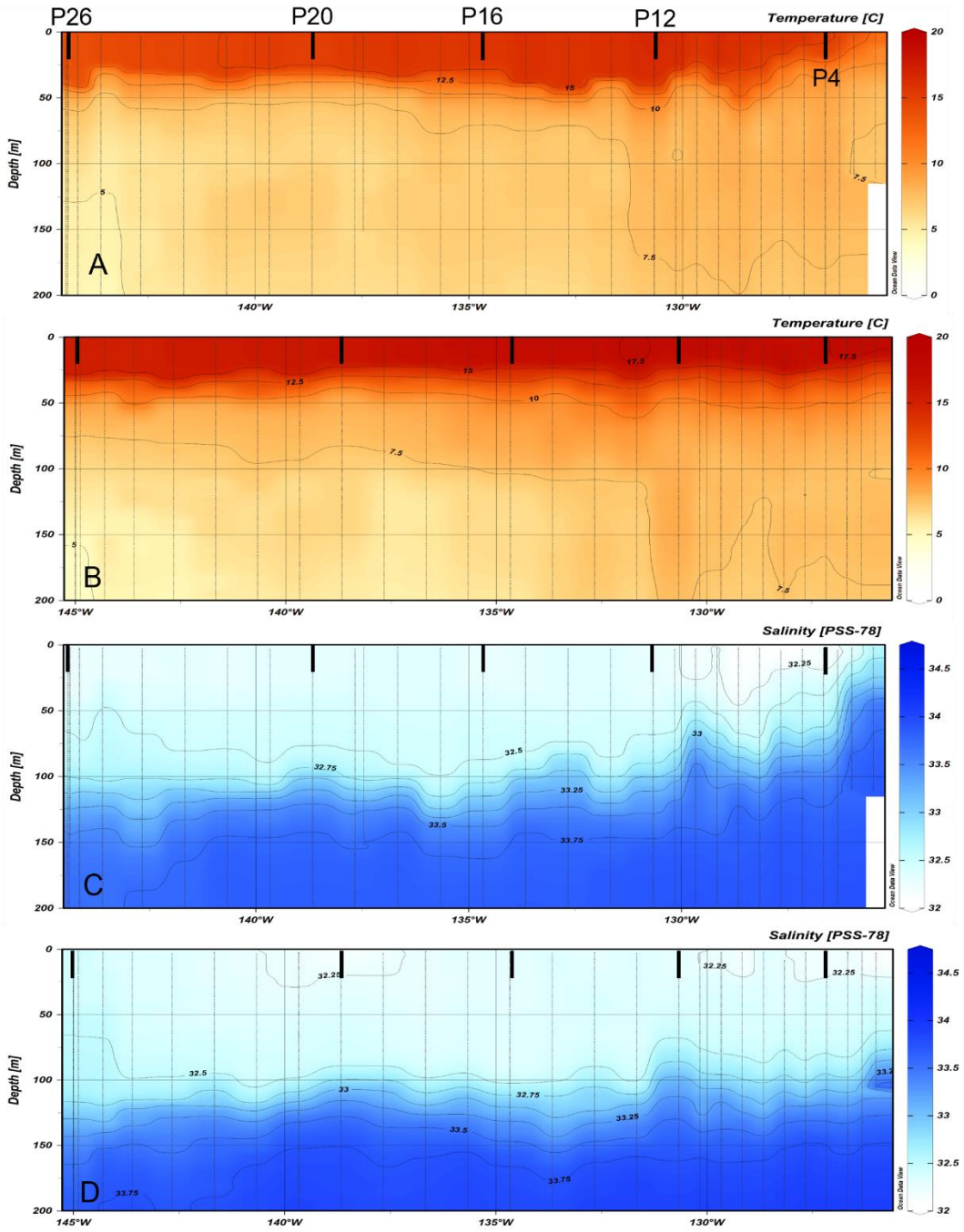

Figure 2.1. Temperature of the upper water column (0-200 m) of the Line P transect in A) 2018 and B) 2019 and salinity over the same range in C) 2018 and D) 2019. Full transect data was obtained from The Department of Fisheries and Ocean's Institute of Ocean Sciences Line P Time-Series. Black dots represent sampling depths from the CTD, colour shading and contours are linearly interpolated between samples. Black bars on the top of each panel represent major Line P stations, from right to left, P4, P12, P16, P20, and P26.

2.3.2 Dissolved nutrient concentrations

Dissolved nutrient data collected as part of this study (at the five major stations) is presented along with surface dissolved nutrient data from all Line P stations and two additional stations P2 and P8, to provide a more complete dataset.

In 2018, [NO_3^-] in the mixed layer were above the LoD (0.1 µM) for the majority of Line P stations, ranging from 0.1-15.5 µM. There was a pronounced shallow (0-20 m) zone of low [NO_3^-] (0.1-1 uM) from P4-P16 with NO_3^- increasing again after P16 to a maximum surface value of 8 µM at P26 (Figure 2.2 A). [NO_3^-] were the lowest at P12 and P16 where [NO_3^-] were <0.1 µM from the surface to ~20 m.

In 2019, surface (0-5 m) [NO_3^-] was below the limit of detection (0.1 µM) at all stations along Line P except P26 where NO_3 reached 0.98 µM (Figure 2.2). Similar to 2018, there was a shallow zone (0-20 m) of very low [NO_3^-] (0.1-1 µM) observed in 2019. However, in 2019, this zone had a much farther longitudinal extent, running the entire length of the transect (Figure 2.2).

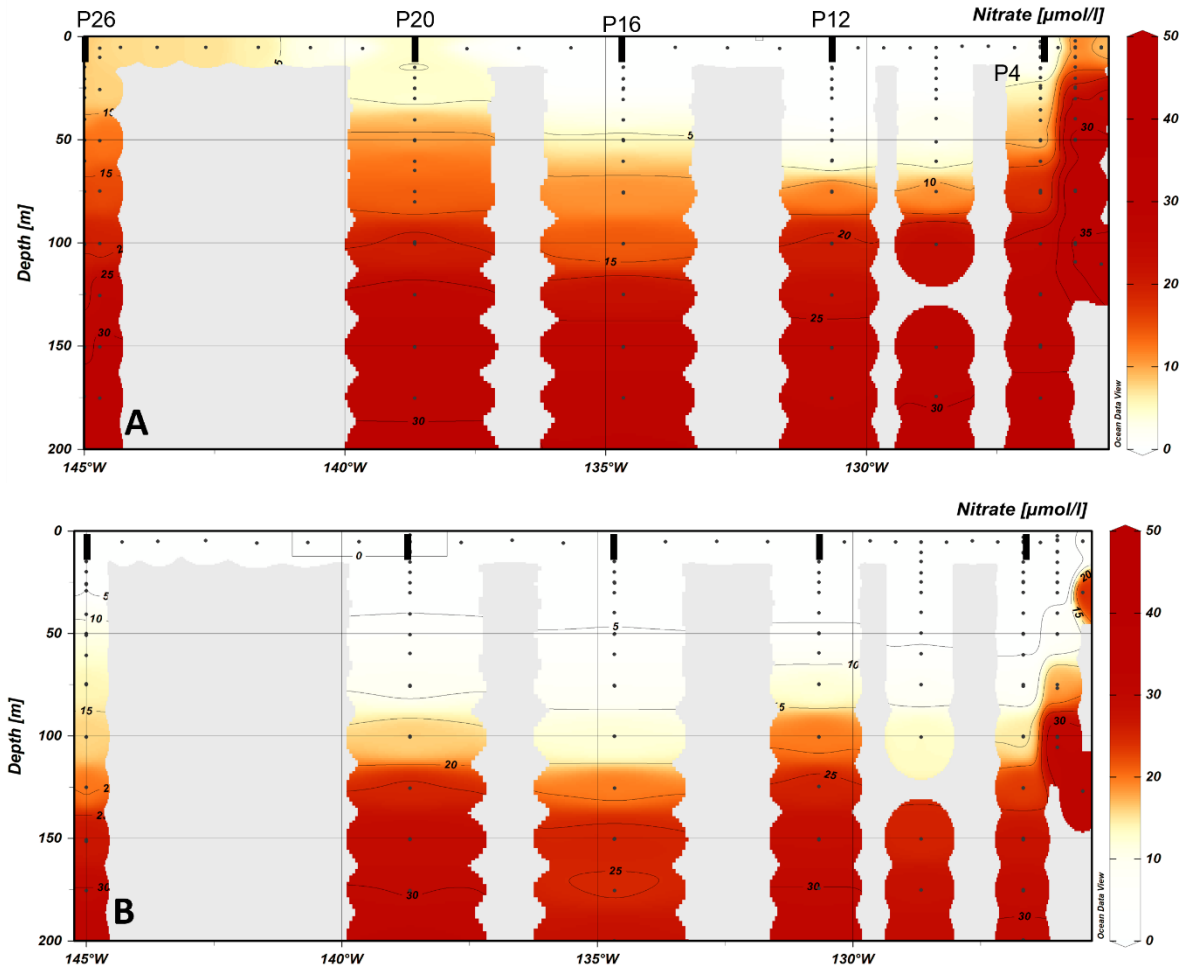

Figure 2.2. Ambient dissolved nitrate (NO_3^-) concentrations in the upper 200 m along the Line P transect in A) 2018 and B) 2019. Colour shading and contours represent [NO_3^-]. Date presented in this figure is a combination of data collected for this thesis from the 5 major stations, and data obtained from the Department of Fisheries and Oceans database (Government of Canada, 2019). Black bars on the top of each panel represent major Line P stations, from right to left, P4, P12, P16, P20, and P26.

In 2018, dissolved silicon ([$Si(OH)_4$]) in the euphotic zone followed a similar pattern of distribution to [NO_3^-] (Figure 2.3 A). [$Si(OH)_4$] were higher (8-16 µM) at P4, decreased at P12 and P16 (<0.3-3 µM) and increased again towards P20 and P26 (5-18 µM). The lowest [$Si(OH)_4$] (<0.3 µM) was measured in the surface (0-20 m) at P16 while the highest [$Si(OH)_4$] was measured below the MLD at 80 m at P26 (18 µM). At all stations except P16, euphotic zone [$Si(OH)_4$] were above the LoD (0.3 µM). In 2019, [$Si(OH)_4$] in the mixed layer was low (0.3-1.23 µM) for the majority of the Line P transect. P4, and P12 had low but detectable [$Si(OH)_4$] in

the mixed layer at 1.23 and 0.48 µM, respectively. $[Si(OH)_4]$ in the mixed layer were below the LoD (0.3 µM) at P16 and P20 (Figure 2.3 B). The highest mixed layer $[Si(OH)_4]$ was measured at P26 (7.7 µM). Overall, $[Si(OH)_4]$ in the mixed layer were lower at all stations in 2019 than in 2018. Longitudinally, the zone of lowest $[Si(OH)_4]$ was centered around P16 in 2018 while in 2019 the zone of low $[Si(OH)_4]$ extended from P4-P20.

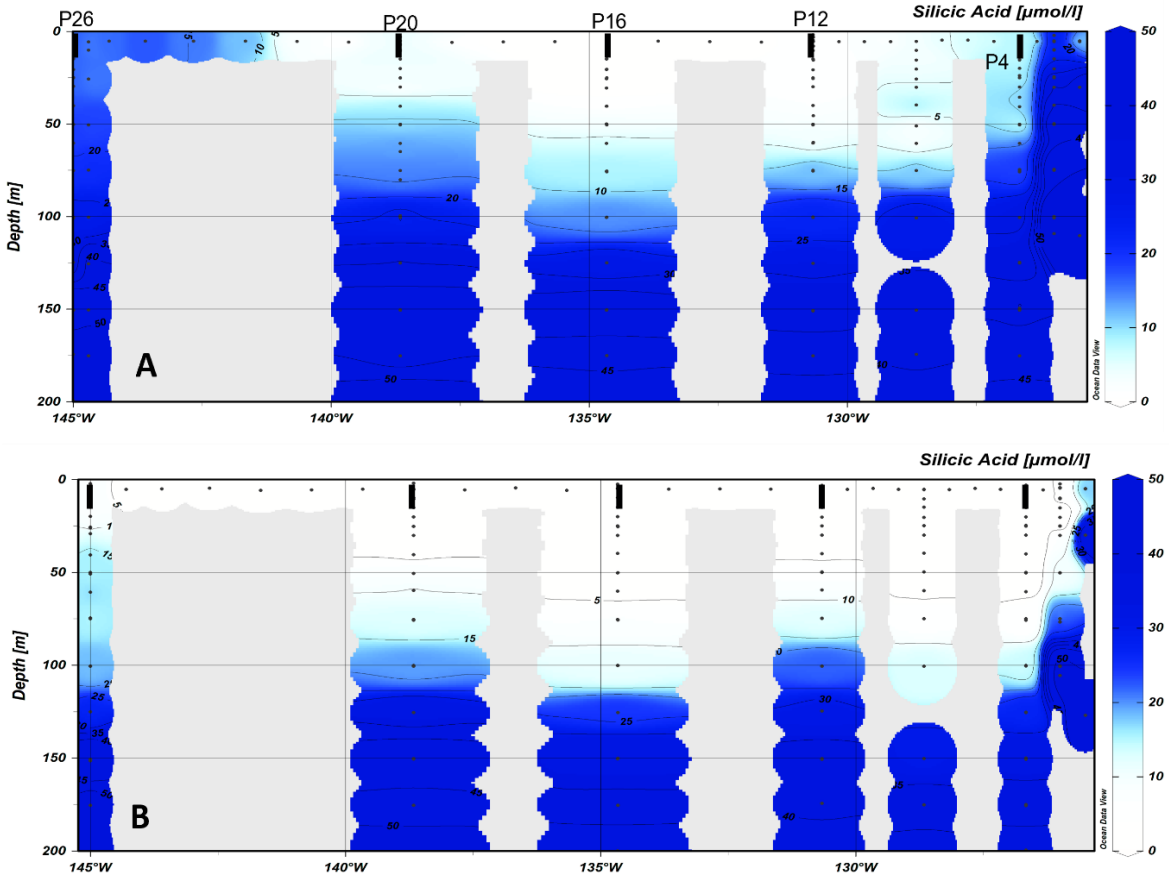

Figure 2.3. Ambient silicic acid ($Si(OH)_4$) concentrations in the upper 200 m along the Line P transect in A) 2018 and B) 2019. Colour shading and contours represent $[Si(OH)_4]$. Data presented in this figure are a combination of data collected for this thesis from the 5 major stations, and data obtained from the Department of Fisheries and Oceans database (Government of Canada, 2019). Black bars on the top of each panel represent major Line P stations, from right to left, P4, P12, P16, P20, and P26.

In 2018, dissolved phosphate ([PO_4^{3+}]) in the mixed layer was above the LoD (0.03 µM) for all stations measured (Figure 2.4 A). [PO_4^{3+}] in the mixed layer followed almost the same longitudnal pattern as [NO_3^-] over the transect; [PO_4^{3+}] was higher at P4 (0.42 µM), decreased slightly at P12 and P16 (0.33 and 0.38 µM respectively), and then increased towards P20 (0.74 µM) with the highest mixed layer value measured at P26 (0.87 µM).

In 2019, [PO_4] also had a similar distribution to the other dissolved nutrients but showed much less longitudinal variation (Figure 2.4 B). All stations had detectable [PO_4] in the mixed layer but there was a shallow (0-20 m) zone of low [PO_4] (0.23-0.39 µM) that extended the entire length of the transect (Figure 2.4). The highest mixed layer [PO_4] was measured at P26 (0.39 µM) and the lowest [PO_4] was at P20 (0.23 µM). Overall, [PO_4] were lower in 2019 when compared to 2018. The highest mixed layer [PO_4] in 2019 (0.39 µM) was similar to the lowest value (0.38 µM) in 2018.

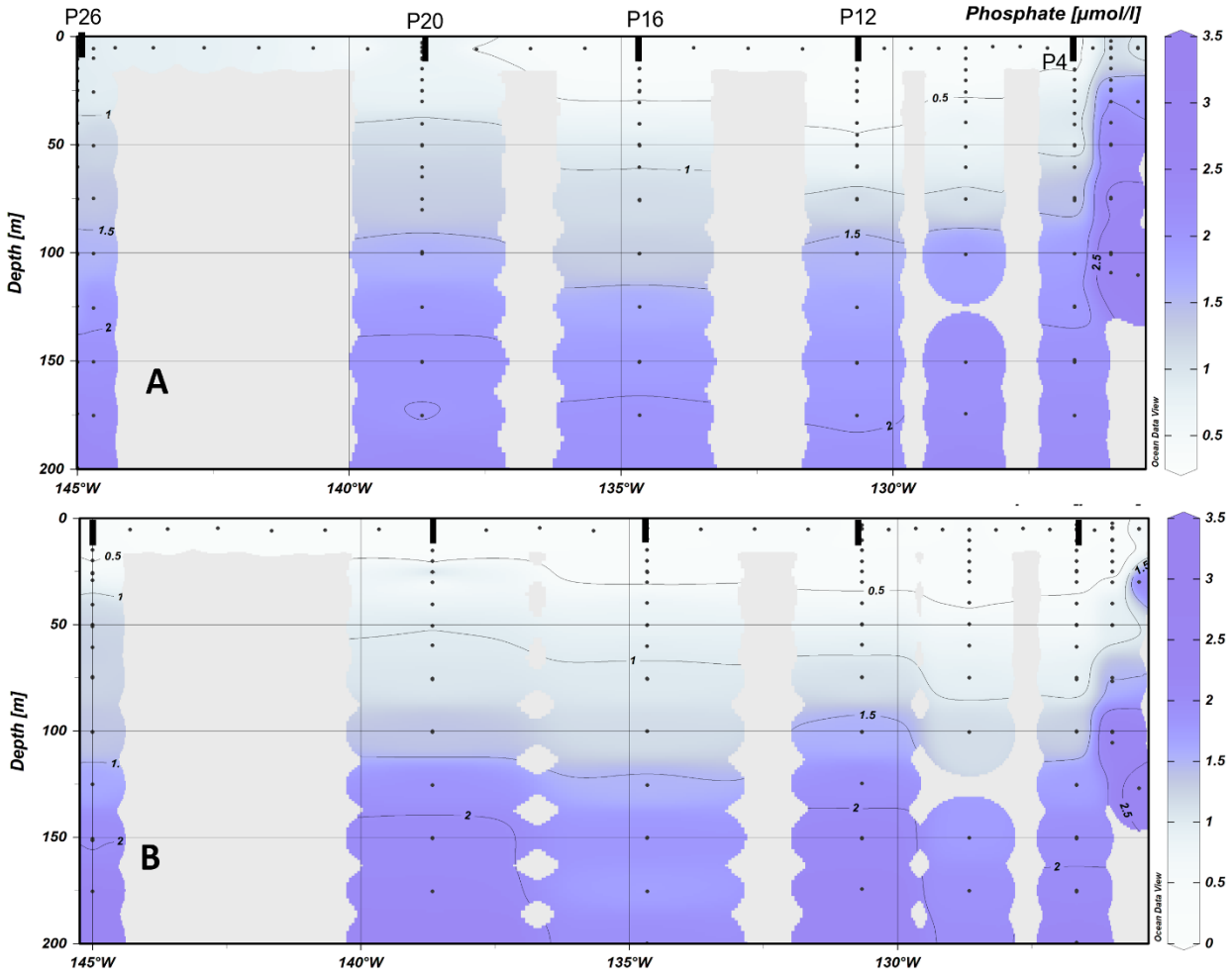

Figure 2.4. Ambient dissolved phosphate concentrations ([PO_4]) in the upper 200 m along the Line P transect in A) 2018 and B) 2019. Colour shading and contours represent [PO_4]. Data presented in this figure is a combination of data collected for this thesis from the 5 major stations, and data obtained from the Department of Fisheries and Oceans database (Government of Canada, 2019). Black bars on the top of each panel represent major Line P stations, from right to left, P4, P12, P16, P20, and P26.

2.3.3 Suspended particulate matter concentrations

2.3.3.1 Chlorophyll-a

In 2018, total euphotic zone chlorophyll-a (chl-a) concentrations were highest in the surface (0-20 m) at P4 with maximum concentrations of 1.17 µg L^{-1} (Figure 2.5). Chl-a was also relatively high (0.9 µg L^{-1}) at P12 but decreased at P16 to the lowest euphotic zone chl-a concentration (0.14 µg L^{-1}) and was low at all depths in the euphotic zone. Chl-a concentrations were slightly higher than P12 at the offshore stations with chl-a reaching 0.26 and 0.37 µg L^{-1} at P20 and P26, respectively.

In 2019, the highest chl-a concentrations were observed at P26 and P20 (1.21 and 1.16 µg L^{-1} respectively) at the chl-max depth and the lowest was observed in the mixed layer at P4 (0.1 µg L^{-1}). Chl-a was low in the upper 5 m (<0.5 µg L^{-1}) for all stations along the Line P transect and was similar to concentrations that were observed at the same depth in 2018, except at P4 where concentrations were much higher in 2018. However, chl-a was higher in 2019 at the chl-max depth for P16, P20, and P26 (Figure 2.5).

Overall, total chl-a was highest at the nearshore stations (P4 and P12) in 2018 but was highest offshore at depth (P26) in 2019. Additionally, in 2019, [chl-a] were higher at the chl-max depth for P16, P20 and P26, while in 2018, [chl-a] were highest above 15 m at all stations.

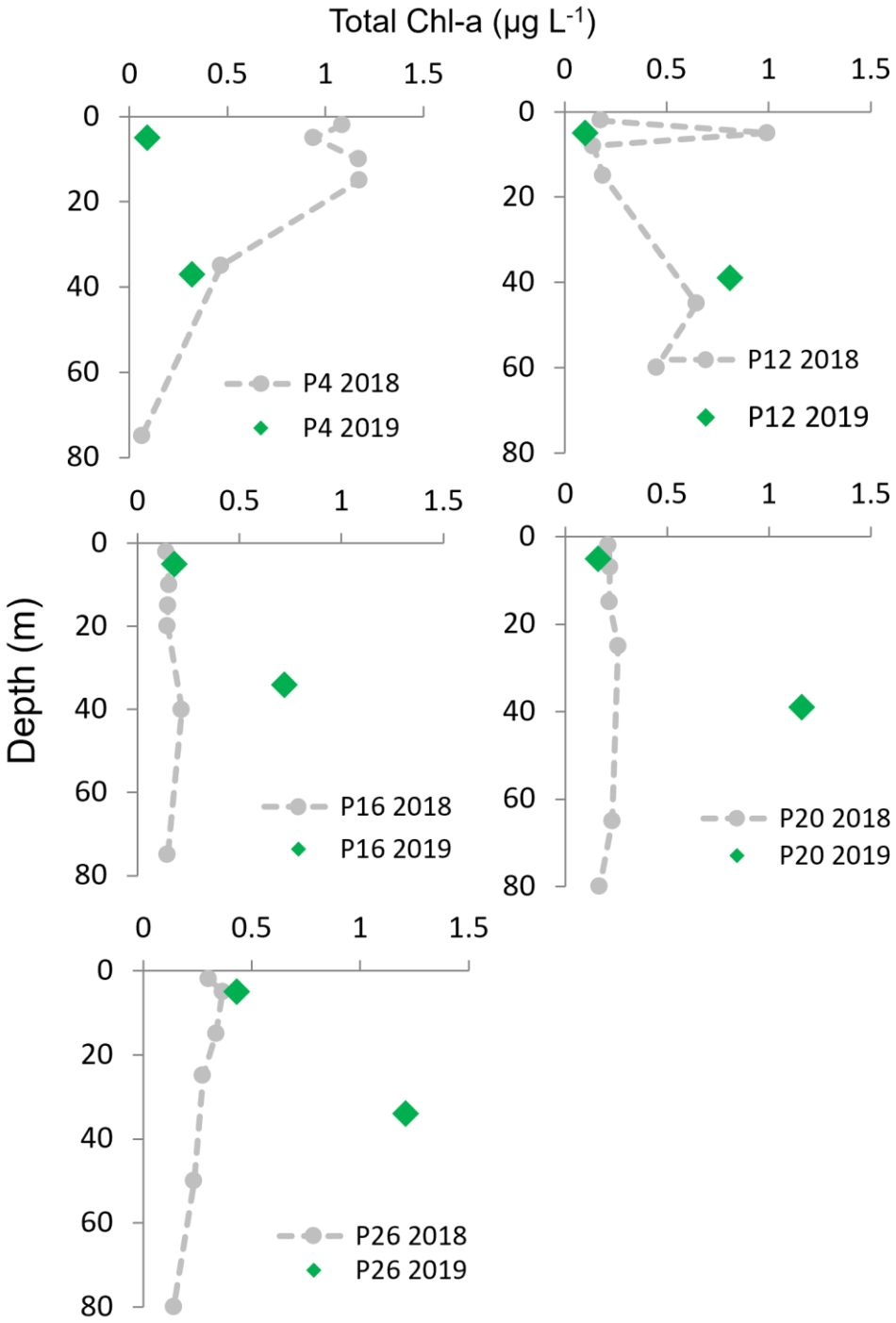

Figure 2.5. Total chl-a (µg L^{-1}) measured in the euphotic zone at the five main Line P stations in 2018 (light grey markers and dashed line) and 2019 (dark green markers).

Cells smaller than 5 µm contributed the majority of chl-a at all stations along Line P in both 2018 and 2019 (Figure 2.6). Relative to the other stations in 2018, P26 and P20 had higher chl-a from cells >5 µm in the euphotic zone but these values were still less than 50% of the total chl-a. In 2019, at P4 and P12, there was a dramatic decrease in total chl-a in the euphotic zone compared to 2018. In 2019, the contribution of cells >5 µm increased at both P20 and P26 relative to 2018. However, a similar increase was not observed at P4, P12, or P16.

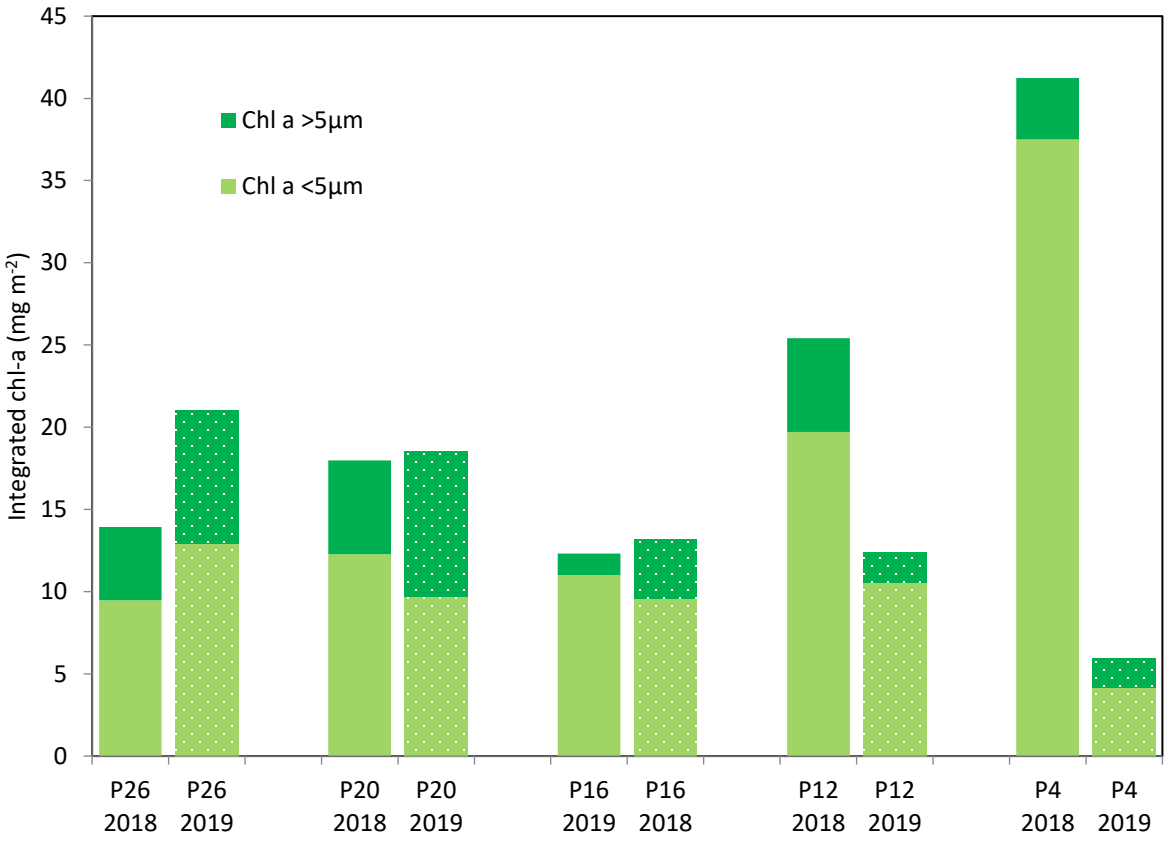

Figure 2.6. Depth-integrated size fractionated chlorophyll-a (chl-a) concentrations (in mg m^{-2}) at the five main stations along the Line P transect during 2018 and 2019. For 2018 data, integrations were performed between the surface and the 1% light depth (nearly equivalent to the chl-max depth for 2018 stations). For 2019 data, integrations were performed from 5m and the chl-max depth. The fractions presented are cells larger than 5 µm (Chl-a >5; dark green) and cells smaller than 5 µm (Chl-a <5; light green). Samples from 2018 are presented as solid bars, samples from 2019 are patterned bars.

2.3.3.2 Biogenic silica

In 2018, the highest euphotic zone [$bSiO_2$] was recorded at P26, reaching 0.57 µM in the upper 2 m (Figure 2.7). [$bSiO_2$] were lowest at P16 where concentrations were ≤ 0.1 µM through the entire euphotic zone. P12 also had extremely low (≤ 0.1 µM) [$bSiO_2$] through the euphotic zone with a small peak (0.187 µM) at 5 m depth. P4 and P20 had similar [$bSiO_2$] with maximum concentrations of 0.36 and 0.39 µM, respectively.

In 2019, [$bSiO_2$] at 5 m were lower than concentrations at the same depths in 2018 at all stations except P16 ([$bSiO_2$] = 0.38 µM at 5 m in 2019). [$bSiO_2$] were <0.4 µM at 5 m for all stations except P26 where $bSiO_2$=0.54 µM. However, [$bSiO_2$] were higher at all stations at the chl-max depth in 2019 compared to 2018. The highest [$bSiO_2$] observed in 2019 was at P26, reaching 1.24 µM at 34 m which was nearly 2.5 x higher than the maximum value observed at any station in 2018. P4, P12, and P20 also had significantly higher [$bSiO_2$] at the chl-max depth (0.94, 0.49, and 0.57 µM respectively) compared to the similar depth in 2018.

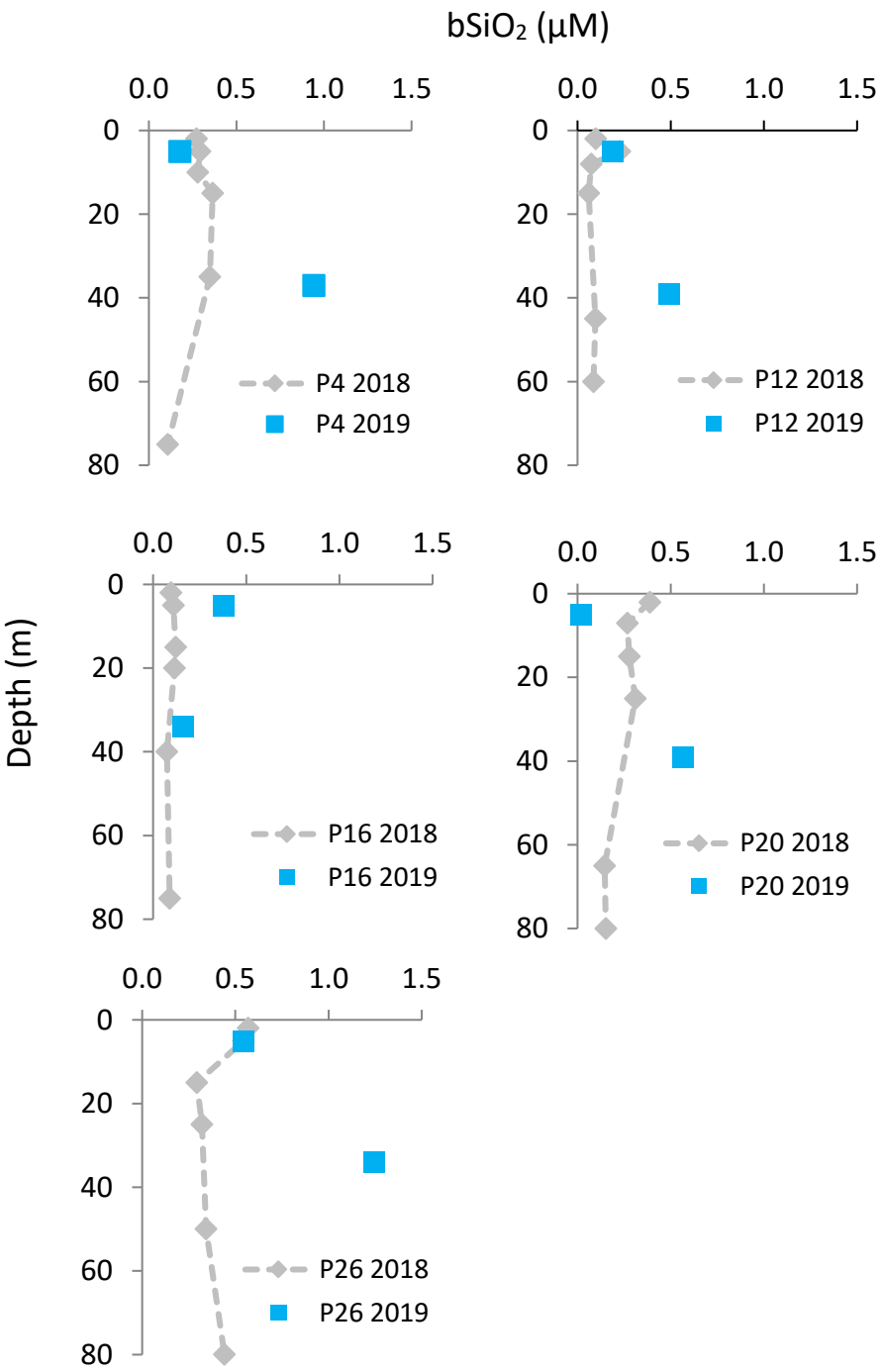

Figure 2.7. Particulate biogenic silica ($bSiO_2$) concentrations in the euphotic zone at the five main stations along the Line P transect in September 2018 (light grey markers and dashed line) and August 2019 (blue markers).

2.3.3.3 Particulate carbon and nitrogen

In the summer of 2018, the highest [PC] was measured in the upper 10 m of the euphotic zone at P4 (381.42 µg L^{-1}) (Figure 2.8). P4 and P12 showed some variation of [PC] with depth but P12, P16, and P20 had relatively homogenous [PC] throughout the entire euphotic zone. The lowest [PC] value recorded was at 8 m at P12 (92.7 µg L^{-1}) but similarly low values were recorded at P16, P20, and P26 throughout the entire euphotic zone. In 2019, [PC] were similar to 2018 values at all stations except P4 where [PC] were significantly lower than in 2018. The lowest and the highest [PC] values were recorded at P12 in 2019 (85.3 µg L^{-1} at 5m and 196.2 µg L^{-1} at 39 m) but values were not considerably different than those measured in 2018 (Figure 2.8).

In 2018, particulate nitrogen (PN) followed a similar pattern of longitudinal distribution as [PC]. [PN] were highest at P4, reaching a maximum of 5.3 µM, and the lowest [PN] (0.92 µM) was also measured at P12 (Figure 2.9) [PN] in the euphotic zone were relatively homogenous and were similar at P12, P16, and P20 (1-2 µM) with a slight increase at P26 to 2.6 µM (Figure 2.8) In 2019, [PN] showed a similar pattern of distribution to PC. While [PN] in the mixed layer was lower in 2019 than 2018 at all stations, there was higher biomass at the sub-surface chl-max at all stations except P4 (Figure 2.9).

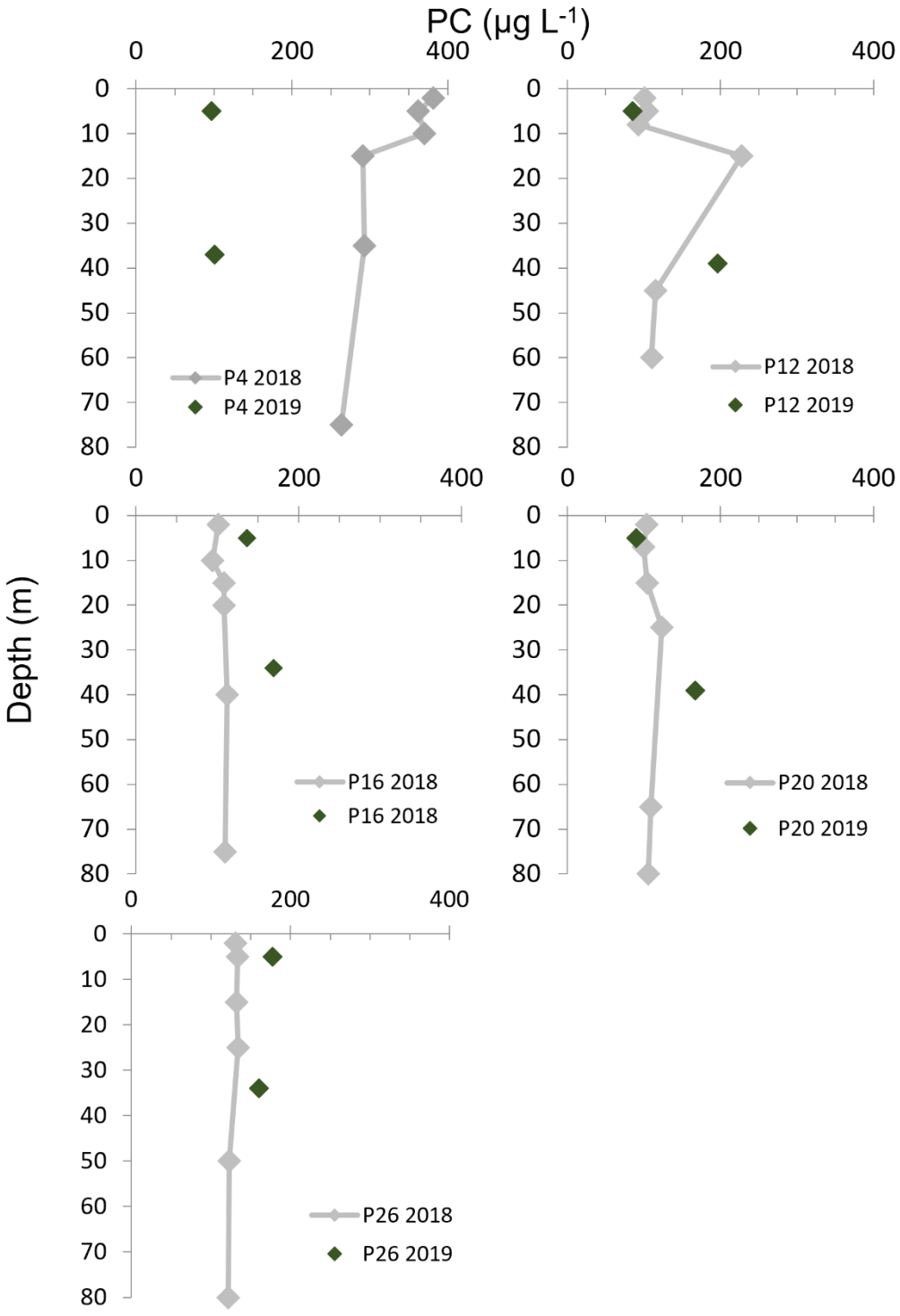

Figure 2.8. Particulate carbon (PC) concentrations in the euphotic zone at the 5 main Line P stations in September 2018 (grey markers and line) and August 2019 (black markers).

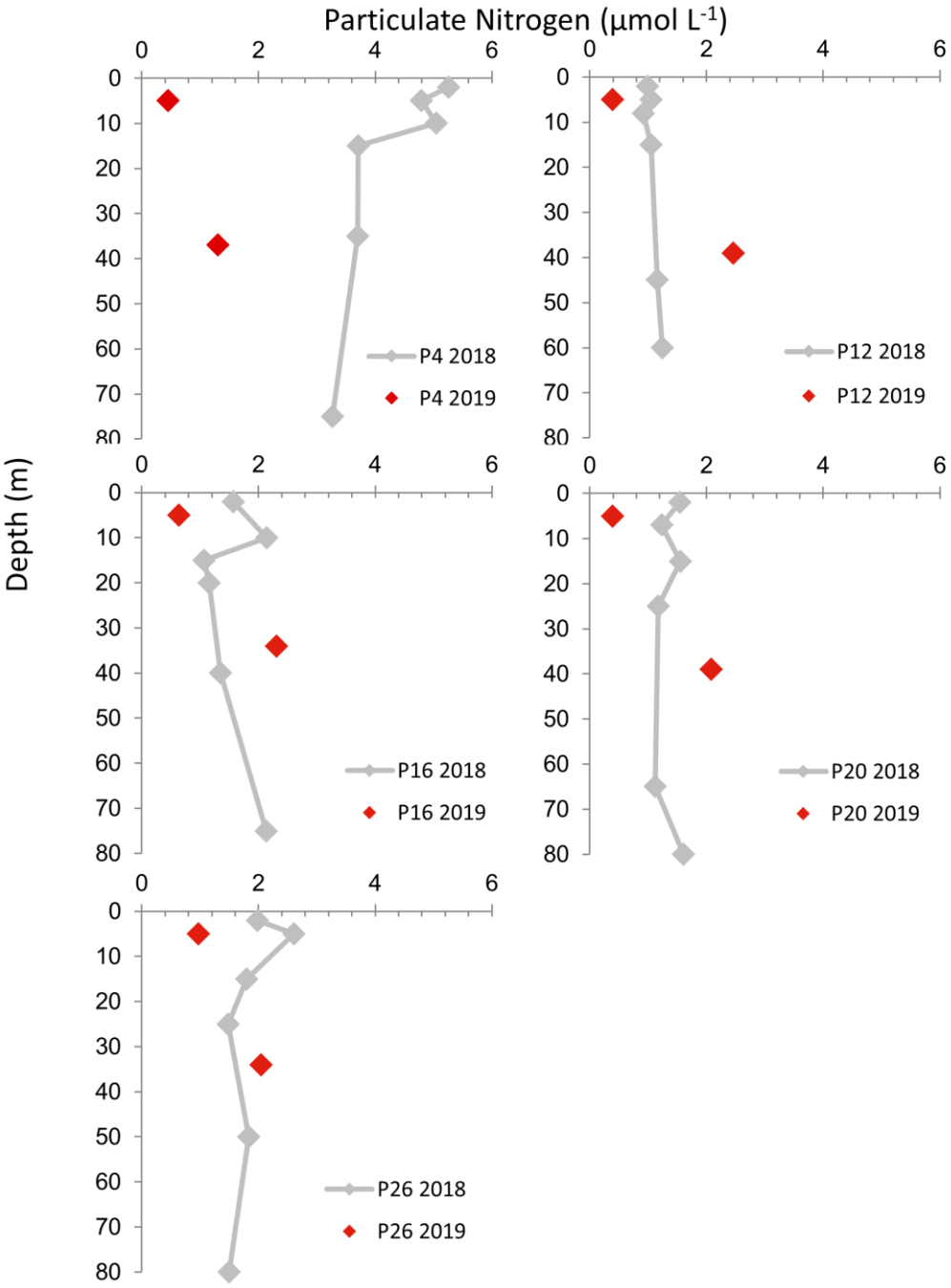

Figure 2.9. Particulate nitrogen (PN; µmol L^{-1}) concentrations in the euphotic zone at stations along the Line P transect in 2018 (grey markers and line) and 2019 (red markers).

2.3.4 Carbon and nitrogen uptake rates

In 2018, carbon uptake (ρC) rates in the euphotic zone were significantly higher at P4 than at all other stations. The four highest ρC values were measured in the upper 15 m at P4 (58-75 µg L^{-1} day^{-1}) (Figure 2.10). All other stations showed ρC <15 µg L^{-1} day^{-1} and had similar distributions throughout the euphotic zone. ρC was higher in the upper 40 m and decreased with depth at all stations.

In 2019, ρC was lower at in the mixed layer at P4 compared to 2018 but there was an increase in ρC in the mixed layer of P26 in 2019 compared to 2018. The highest ρC of 2019 (29.7 µg L^{-1} day^{-1}) was observed at the chl-max depth (39 m) at P12. This value was higher than the 2018 rate at a similar depth (4.34 µg L^{-1} day^{-1}) but was lower than the maximum value measured in 2018 at 2 m at P4 (75 µg L^{-1} day^{-1}). In 2019, ρC at P16 and P20 were not significantly different from the 2018 rates (Figure 2.10).

In 2018, nitrate uptake (ρNO_3) was highest at P4, reaching a maximum of 1.23 µmol L^{-1} day^{-1} at 15 m At all other stations, ρNO_3 was <0.2 µmol L^{-1} day^{-1} at all depths measured (Figures 2.11). In 2019, ρNO_3 was much lower at P4 than in 2018, with a maximum rate of 0.07 µmol L^{-1} day^{-1} measured at 5 m. The highest ρNO_3 was measured at 5 m at P26 (0.26 µmol L^{-1} day^{-1}) and was nearly five times lower than the maximum value measured in 2018 at P4 that was1.23 µM/day at 15 m depth. Much like ρC, between 2018 and 2019, ρNO_3 decreased at P4 but increased at P26 with all other stations having similar values between years.

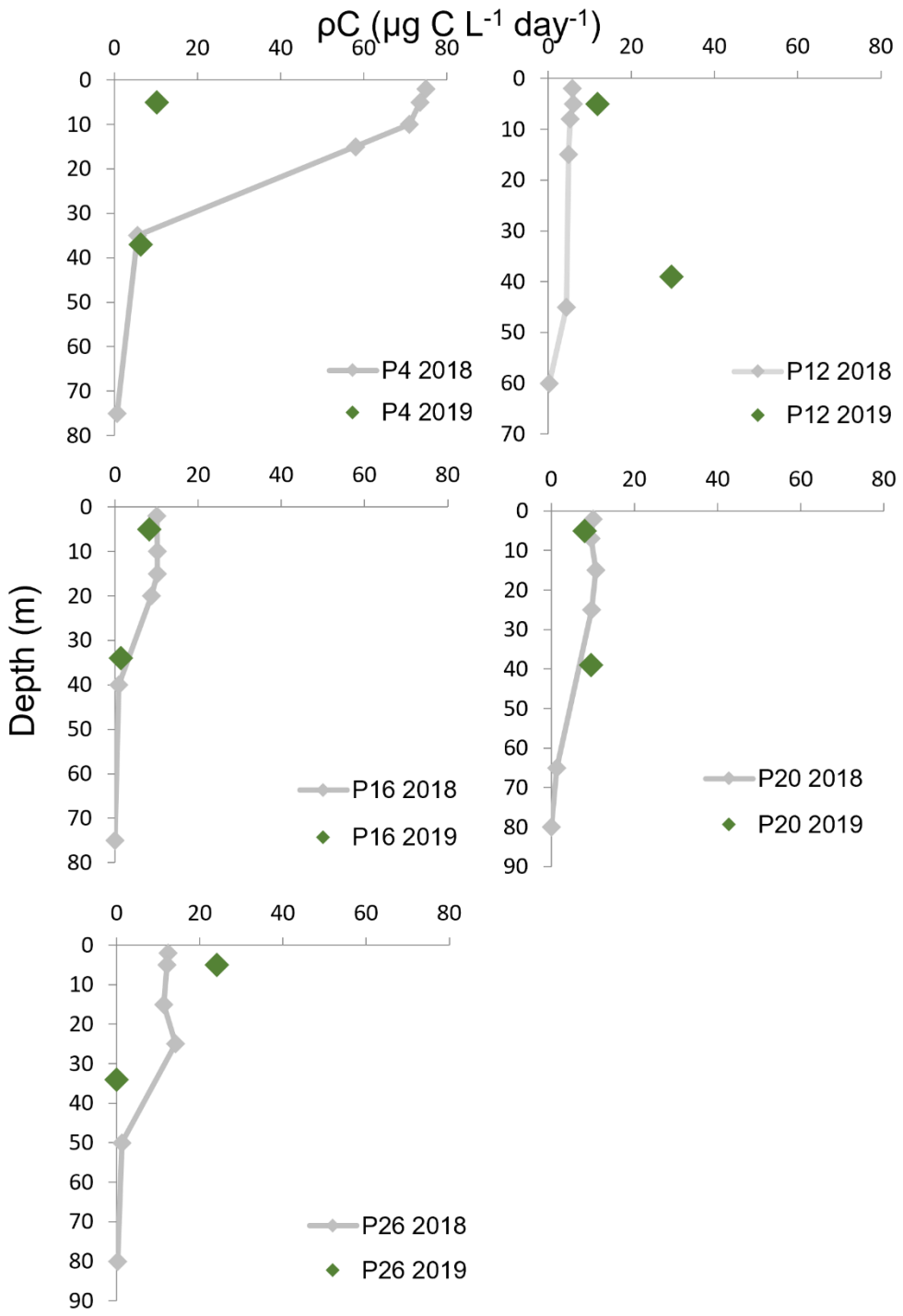

Figure 2.10. Rates of carbon uptake (ρC) at major Line P stations in 2018 (grey markers and line) and 2019 (green markers). Rates are represented as individual depth measurements in µg C L^{-1} day^{-1}.

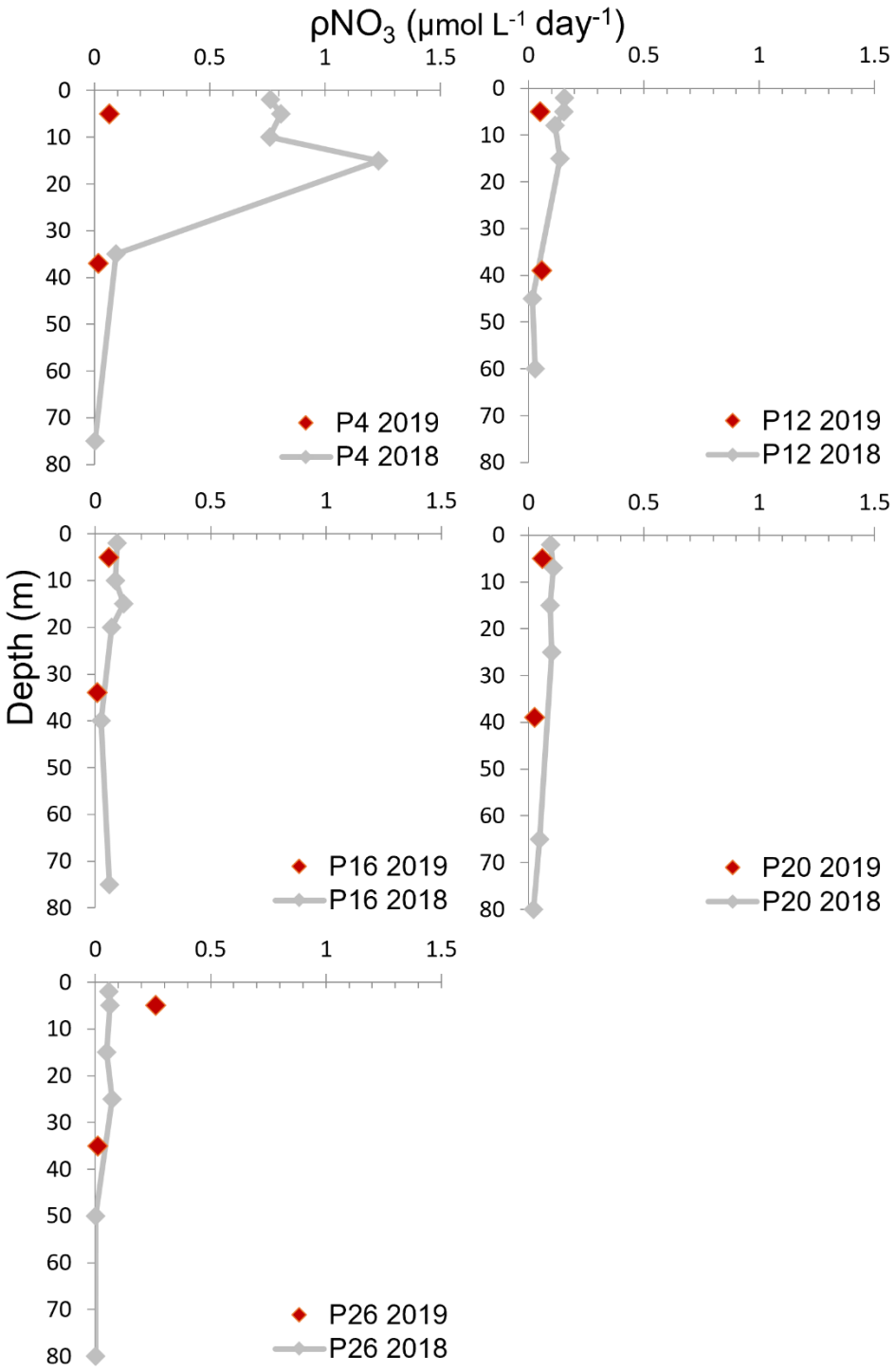

Figure 2.11. Rates if nitrate uptake (ρNO_3) in the euphotic zone at major stations along the Line P transect in 2018 (grey markers and line) and 2019 (red markers).

In 2018, all Line P stations, except P4, were dominated by regenerated productivity, (ρNH_4^+ + ρUrea-N) (Figure 2.12). Depth-integrated ρNH_4^+ contributed most to total depth-integrated N uptake at P12-P26 with ρUrea-N and ρNO_3^- contributing similar amounts at P12-P26. At P4, the total N uptake was dominated by NO_3^-. The highest total depth-integrated N uptake rate was measured at P4 (40.5 mmol m^{-2} day^{-1}) while the lowest was at P26 (8.12 mmol m^{-2} day^{-1}).

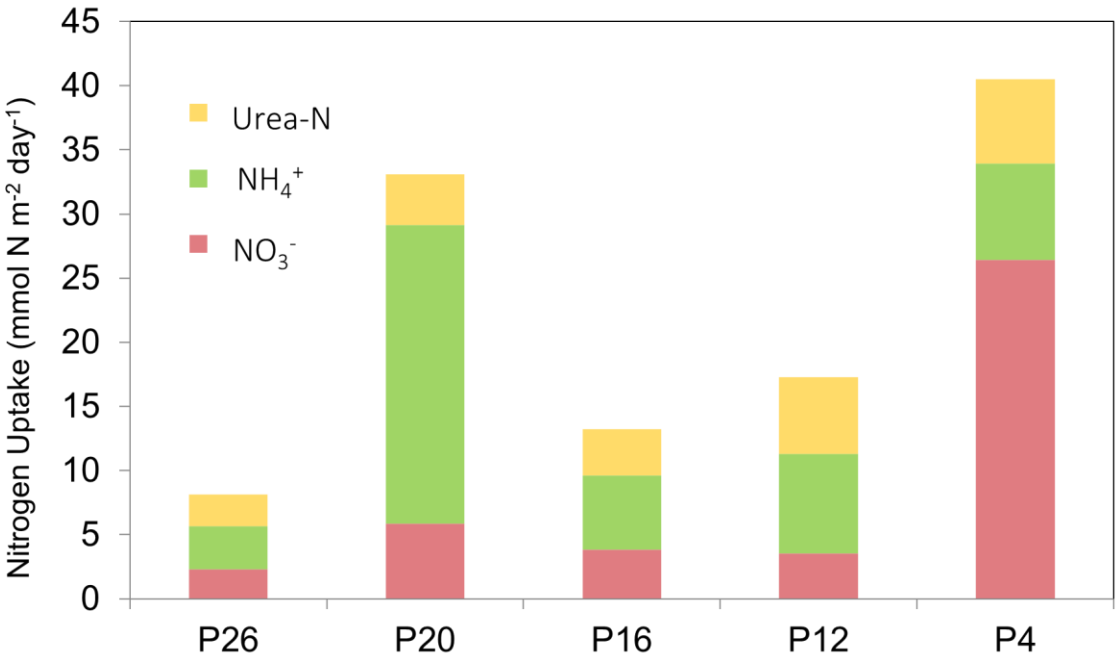

Figure 2.12. Depth-integrated nitrate (NO_3), ammonium (NH_4) and urea N uptake rates at the five major Line P stations in September 2018. Rates are depth-integrated euphotic zone values (from the surface to 0.1 % surface PAR).

In 2018, the integrated *f*-ratio was highest at P4 (0.62) where NO_3 uptake was dominant (Figure 2.13). At all other stations, the *f*-ratio was <0.31 with the lowest ratio occurring at P20 (0.18). In 2019, *f*-ratios were lower than or similar to 2018 values at both P4 and P12 (0.46 and 0.23, respectively). However, at P16-P20 the *f*-ratios in 2019 were considerably higher than in 2018 with the maximum occurring at P26 (0.90).

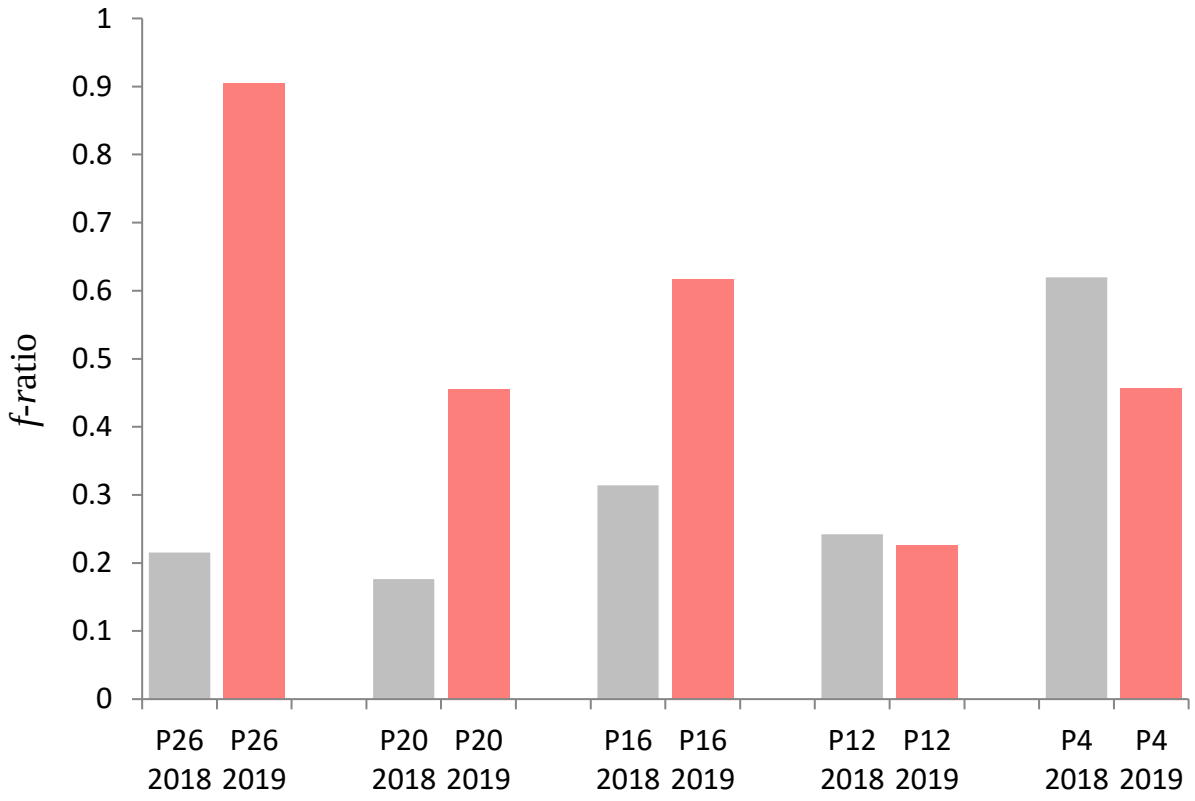

Figure 2.13. Depth-integrated *f*-ratios calculated at the 5 main Line P stations in September 2018 (grey bars) and August 2019 (red bars). Rates used to calculate *f*-ratios are depth-integrated euphotic zone values (from the surface to 0.1 % surface PAR).

In 2019, the exclusion of ρNH_4 and ρUrea-N from the *f*-ratio calculation likely led the *f*-ratio to be about 17-40 % higher than if all N species were included (Wafar et al., 1995). If *f*-ratios were overestimated by the maximum amount (40%) in 2019, *f*-ratios would still be higher than, but similar to 2018 values at all stations except P26 and P4. The P26 *f*-ratio in 2019 would still be much higher than the 2018 value and the P4 *f*-ratio in 2019 would be even lower. Based on these data, the most considerable difference that occurred between years was the switch from predominantly regenerated to new production at P26 and the switch to more regenerated production at P4 during summer 2019.

2.4 Discussion

2.4.1 Summary of results

During the 2019 MHW, there were several differences in physical, chemical, and biological characteristics of the water column when compared to the pre-MHW year of 2018. While temperatures in the euphotic were generally high in both 2018 and 2019, maximum temperatures were higher in 2019. In 2019, mixed layer depths were less variable along the Line P transect, indicating stronger stratification. Dissolved nutrients in the euphotic zone were lower in 2019 than in 2018 and the longitudinal area where nutrients were low extended much farther offshore than in 2018.

Chl-a concentrations in the upper 5 m were similar in 2018 and 2019, but in 2019 at stations P16-P26 there was a pronounced sub-surface chl-a maximum that was not observed in 2018. Concentrations of $bSiO_2$ at all stations were similar in the mixed layer for both 2018 and 2019. However, similar to chl-a there were subsurface maxima (at all stations except P16) that were considerably higher in 2019 than at the same depth in 2018. In both 2018 and 2019, P26 had higher [$bSiO_2$] than in all other stations. The most notable difference in [PC] and [PN] was observed at P4 where both particulate concentrations were significantly higher in 2018 than in 2019. This pattern was also observed in ρC and ρNO_3 where P4 showed significantly higher uptake rates in 2018 compared to 2019, but rates at all other stations were similar between years. The amount of productivity derived from NO_3 (new productivity) was much lower at P4 in 2019 than in the previous year but was much higher at P26 in 2019 compared to 2018. Overall, there was high $bSiO_2$ and new productivity at P26 in 2019, while there was a marked decrease in chl-a, $bSiO_2$ and new productivity at P4 in 2019.

2.4.2 Relationship between physical characteristics of the water column and pelagic production along Line P

Primary productivity in the ocean relies on a supply of nutrients to the sunlit surface waters. While both alluvial and aeolian inputs may be important in certain regions, most of the nutrient supply occurs as a result of deep water surface injection as well as horizontal advection (Falkowski et al., 1998; Lozier et al., 2011). Increases in ocean warming as well as changes to wind patterns are predicted to lead to a global increase in upper ocean stratification (Houghton et al., 2001; Sarmiento et al., 2004). This increase in stratification is also predicted to contribute to a global decline in primary productivity due to a decrease in nutrient resupply to surface waters (Behrenfeld et al., 2006). Simply, more stratified waters will require more energy to overturn and so nutrient resupply will not be as efficient, resulting in nutrient limitation (Lozier et al., 2011). However, the exact mechanisms and effects of stratification are much more complex and variable leading to a range of impacts on primary producers globally (Noh et al., 2022).

During 2019, there were several noticeable differences in the physical and chemical properties of the mixed layer along the Line P transect compared to both 2018 and climatic averages from 1981-2010. During MHW conditions, lower E-W wind activity can increase surface ocean stratification in two ways. Lower wind activity results in less heat loss and less evaporation from the surface ocean in the NE Pacific (Amaya et al., 2020; Bond et al., 2015), which causes surface waters to retain heat and remain less saline. Additionally, the decrease in wind activity results in less surface mixing and leads to a shallower mixed layer and a more stratified euphotic zone. The mixed layer depth along Line P was shallower and less variable in 2019 than in 2018 at all stations except P4 (Table 2.1, Figure 2.14). When examining density profile at all five of the main Line P stations, there are signs that stratification was more

pronounced in 2019 than in 2018 at the same station (Figure 2.14). Specifically at P4, density profiles indicate that summer upwelling may not have been as strong during the summer of 2019 which is evident by the more pronounced pycnocline around ~100m in 2019 (Franco et al., 2021). However, MLD can be variable over short time periods (days-weeks) and daily MLD may not be as representative of full seasonal averages (Ianson eta al., 2012).

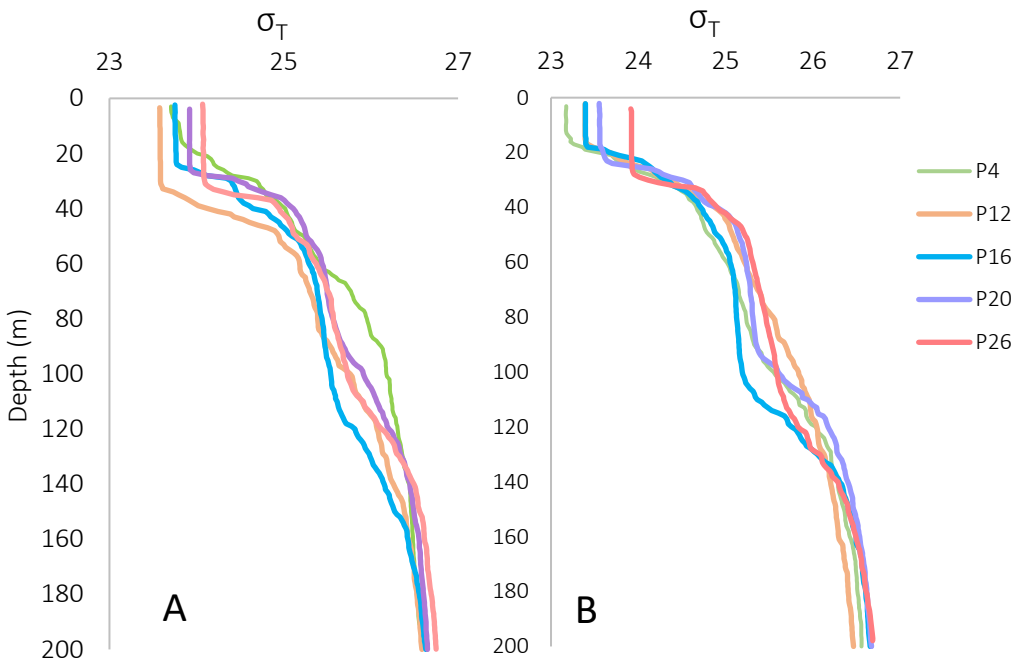

Figure 2.14. Density (σ_T) of the upper 200 m of the water column at major Line P stations in A) summer 2018 and B) summer 2019.

Mixed layer temperatures were higher along the majority of Line P in 2019 when compared not only to 2018 data, but to the 1981-2010 summer climatic averages (Figure 2.15). For example, while the temperature at 5 m depth at P4 in 2019 was 17.9 °C, the climate average from 1981-2010 in August at P4 is only 15.1 °C (Figure 2.15). While temperatures in summer of 2018 at 5 m depth were close to the average for the region, temperatures in 2019 were higher at every station, particularly between stations P2 and P6 showing anomalies of up to 4° C(Figure 2.15). These higher temperatures observed along Line P are consistent with observations during

other MHWs such as the 2015 “blob” and 1997/1998 El Niño (Amaya et al., 2020; Ross et al., 2021; Xu et al., 2021). Additionally, observations show that while surface and subsurface temperatures in 2018 were near average, both surface and subsurface temperatures in 2019 were higher than both the 1956-2012 and 1981-2010 averages (Boldt, 2020).

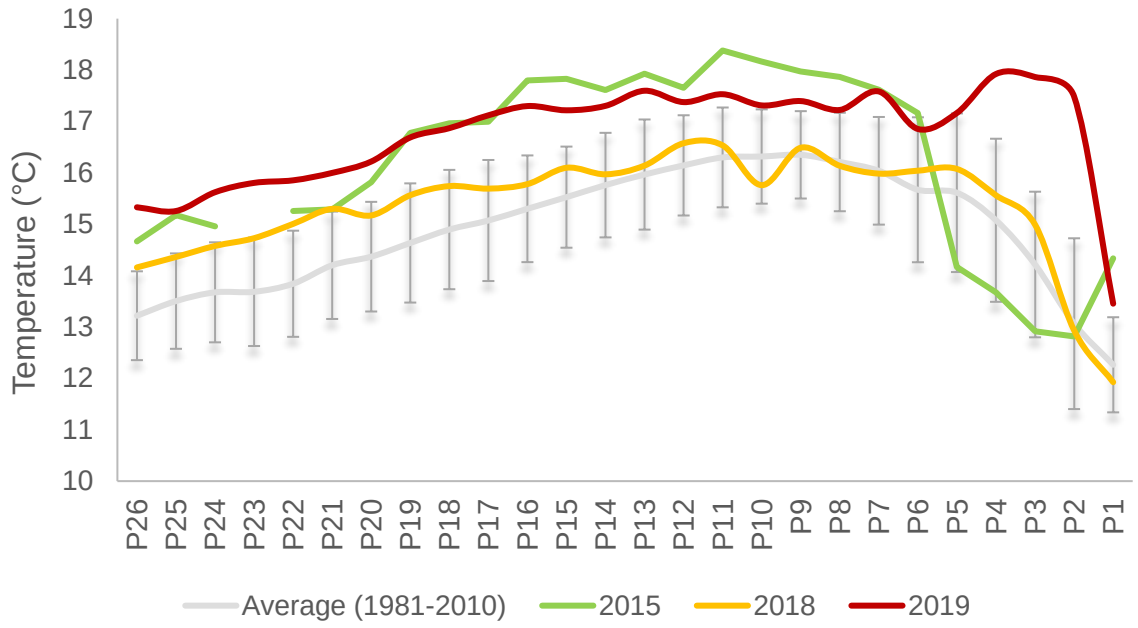

Figure 2.15. Average summer (August-September) sea temperature (°C) at 5 m depth measured along the Line P transect from 1981-2010 with error bars showing sample standard deviation. Both 2018 (orange line) and 2019 (red line) are plotted along with the 2015 marine heatwave, the “blob” (green line).

This increased stratification and higher temperatures may have two effects on the pelagic primary producers along Line P. Stratification and decreased mixing can result in less nutrient input from deep waters, which will ultimately limit the total production that can occur during the growing season. However, the increased water column stability may have some localized benefits along Line P, leading to increased light availability when phytoplankton are not mixed into deeper waters (Maldonado et al., 1999; Peña et al., 2019). This increase in light may lead to higher rates of primary productivity and the resultant increased rate of biological uptake of

nutrients. This benefit will only lead to an increase in total production if there are sufficient nutrients, and so it is limited in the extent of its effect. Additionally, the mechanisms by which light and nutrients "limit" primary production are different and so an increase in one will not always lead to an increase in productivity without a corresponding increase in the othger (Falkowski et al., 1992). Even with sufficient light, a decrease in the total inventory of nutrients can limit the total phytoplankton biomass produced (Falkowski et al., 1992, 1998). Thus, the overall effect of stratification will likely be a decrease in nutrient inventories along Line P due to lower mixing and potentially from increased initial uptake rates if more light is available or if the growing season starts earlier (Whitney & Welch, 2002).

2.4.3 Dissolved nutrients as a limiting factor for phytoplankton during the 2019 MHW

Previous research has shown that dissolved NO_3 and $Si(OH)_4$ in the surface waters of the majority of the Line P stations (mostly the oceanic end of the Line) rarely fall below detectable values, even in the late summer (Varela & Harrison, 1999; Peña & Varela, 2007; Whitney & Freeland, 1999). Very low macronutrient concentrations can, however, be regularly present along the more coastal end of the transect (~P1-P12) during the phytoplankton growing season, but this zone of nutrient depletion rarely extends past P16 (Varela & Harrison, 1999; Peña et al., 2019; Peña & Varela, 2007; Whitney & Freeland, 1999). This is consistent with observations from 2018, where both NO_3 and $Si(OH)_4$ were detectable at nearly all stations, with NO_3^- only falling below the LoD in the mixed layer of P12 and P16. However, in 2019, both NO_3^- and $Si(OH)_4$ concentrations were much lower in the mixed layer, and depletion was detected further offshore than normally observed.

Along Line P, micro and macronutrients are resupplied to the upper water column via mixing of deep water, normally during the winter months. When mixing decreases during

MHWs, there may be a signal in winter nutrient supply preceding the growing season when temperature anomalies start to build (Taves et al., 2022; Amaya et al., 2020). However, the 2019 MHW is characteristic as being a summertime MHW and winter nutrient concentrations in the water column in 2019 were not significantly different from 2018 or the regional averages. For example, [NO_3^-] during both winter 2018 and 2019 followed the same spatial trend, lower at P4 and increasing seaward to P26, and show nearly identical values at the five main stations for both years (Figure 2.16).

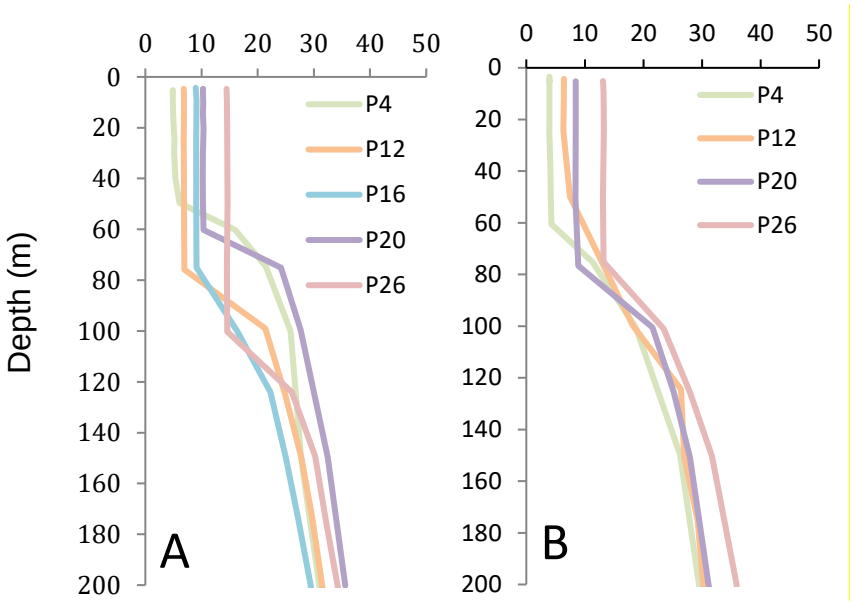

Figure 2.16. Dissolved NO_3 from the surface to 200 m in winter (February) of A) 2018 and B) 2019 at five major stations along the Line P transect. In winter 2019, P16 was not sampled and so data is not available. Data were obtained from the Department of Fisheries and Oceans Line P time-series public repository.

Nitrate concentrations from winter 2019 are similar to those of previous El Niño periods such as 1994 (Whitney et al., 1998) and 1997/1998 (Whitney et al., 2002). During these periods, nutrient limitation in the surface waters occurs after several seasons of poor nutrient repletion (Whitney et al, 1998). So, although winter nutrient concentrations may only be slightly lower than averages or those measured during la Niña conditions, depletion can become more extreme

each subsequent growing season, until the dissipation of the heat wave (with the onset of La Niña conditions for example).

Depletion of nutrients to the extent observed in 2019 can cause limitation of primary production in two ways. Physiological limitation of the *in-situ* phytoplankton population may occur if nutrient concentrations fall below a level that allows for the efficient uptake of dissolved nutrients. In order to assess if this type of nutrient limitation is occurring, enrichment experiments must be performed to see if uptake rates can be stimulated with the addition of the nutrient in question (see chapter 3). However, more simply, a reduction in the total inventory of nutrients will ultimately lead to less total biomass of the system (Falkowski et al., 1992, 1998). Based on the anomalously low nutrient data from 2019, it is likely that some nutrient limitation is occurring at certain Line P stations. However, a more in-depth analysis of each is required. Chapter 3 of this thesis will examine the extent of physiological limitation from both NO_3^- and Si that may be occurring in the subarctic NE Pacific during the 2019 MHW. Measurements of total yearly biomass as well as nutrient inventories should be a focus of future research, specifically during MHWs as it may inform whether the potential total production of a system will change.

2.4.4 Primary productivity and biomass during the 2019 MHW

In 2019, total chl-a in the mixed layer of P4-P20 was <0.2 µg L^{-1}, which is anomalously low for the region (Varela & Harrison, 1999; Peña & Varela, 2007, Peña et al., 2019). However, chl-a concentrations at the chl-max depth were often higher than those measured in 2018. Very low total [chl-a] were measured at many depths throughout the euphotic zone in 2018, which indicates that variability in the system is not solely linked to MHW events. In 2018, many stations along Line P had a homogenous depth distribution of chl-a through the entire euphotic zone and did not have a well-defined subsurface chl-max. This trend was observed in PC, PN,

and $bSiO_2$, with vertical distributions in 2018 being more homogenous whereas in 2019 particulates were more concentrated at the subsurface chl-a maximum. This shift in distribution of biomass to deeper subsurface chl-a maxima during times of higher stratification has been observed in other oceanic regions (Chen et al., 2022). Due to the lower nutrient availability in the shallower areas of the euphotic zone, phytoplankton may only be able to grow at depths where nutrients concentrations are higher (subsurface). Additionally, when phytoplankton grow at deeper depths, chl-a concentrations in cells must be increased to counter the lower radiation input (Bock et al., 2022). So, this observed increase in deep chl-a in 2019 may be due to both the restriction of phytoplankton to deeper, nutrient-rich waters and the physiological increase of [chl-a] per cell.

While the distribution of biomass did show some variation between 2018 and 2019, particularly with depth, both ρC and ρNO_3 were not considerably different between years. The only stations that had notable difference in primary productivity in 2019 were P4 and P26. At P4, both ρC and ρNO_3 were much lower in 2019 than in 2018 and there was a shift to regenerated productivity in 2019. The SST at P4 were the highest recorded over the entire study area, reaching nearly 18 °C, extremely high for the area, even in summer (Crawford et al., 2007; Iwabuchi & Gosselin, 2019). At P4, NO_3 was below detection (<0.1 µM) but $Si(OH)_4$ was still present at 1.23 µM in the mixed layer. Likely, this indicates that N and not Si was the limiting nutrient for assemblages at P4. At P26, there were also several anomalies in biomass and productivity in 2019 compared to both 2018 and historical measurements. While P26 traditionally has a low primary producer biomass, dominated by small-celled phytoplankton, in 2019, $bSiO_2$, total chl-a and chl-a >5 µm were all anomalously high. Additionally, there was an increase in both the surface ρNO_3^- and the *f*-ratio. Regenerated productivity is nearly always

higher at P26 and this shift to a new productivity dominated system has been rarely observed (Varela & Harrison, 1999; Peña & Varela, 2007). All dissolved nutrients measured were above the LoD at P26 so it is not likely that significant macronutrient limitation was occurring.

The lower dissolved NO_3, and C and NO_3 uptake rates that were observed at P4, as well as the higher biomass and productivity at P26 could be the result of a temporal shift in the growing season that has been observed during MHW events. In some cases, increased temperatures could lead to significant nutrient drawdown beginning earlier in the growing season, resulting in more extreme nutrient depletion and production earlier in the season. This is a phenomenon that has been observed during other warming events (Whitney & Welch, 2002; Wyatt et al., 2022) and has implications for how primary production and nutrients vary temporally over the season. In areas such as P4 where potential for production is high due to sufficient micronutrients, temperature-enhanced drawdown earlier in the year, without significant input from mixing, could lead to earlier and shorter overall growing seasons (Yamaguchi et al., 2022). This would be reflected by a decrease productivity and biomass in the summer compared to cooler years. At P26, warmer temperatures, coupled with a stable water column may actually lead to enhanced light availability and sustained productivity of large-celled, NO_3-fueled phytoplankton well into the summer (Peña et al., 2019).

While specific oceanic regions may respond differently, this shift in timing of productivity has the potential to decouple the trophic interactions of zooplankton and fish larvae that rely on phytoplankton and may lead to less productive systems overall (Durant et al., 2019; Yamaguchi et al., 2022). Future research in the NE Pacific focusing on timing of bloom onset, maximal uptake, and nutrient depletion will be very important for understanding these potential effects of MHWs.

2.4.5 Phytoplankton dynamics in 2019 compared to historical warming events

Although blob-like MHW events are a recently described phenomenon, warming events in the Northeast Pacific have occurred in the past in conjunction with well-established atmospheric cycles. Increased warming and stratification linked to El Niño, Pacific Decadal Oscillation (PDO), and North Pacific Gyre Oscillation (NPGO) has been observed for many years in the Line P region (Crawford et al., 2007; Peña & Varela, 2007). However, the intensity, the duration and extent of warming were more severe during the 2015 and the 2019 events than during other warming cycles, including the 1997/1998 El Niño (Amaya et al., 2020; Chen et al., 2021). For this reason, MHWs seem to have more severe effects when compared to other more predictable heating cycles.

While the 1997-1998, 2015, and 2019 MHW events had similar causes, these three MHWs differed in several key ways. Firstly, although the first temperature anomaly peak of the 2019 MHW occurred in November 2019, the increase in SST from May to August was unprecedented, meaning that unlike the 2015 blob, the 2019 MHW was intensifying during the summer, not the winter (Amaya et al., 2020). The 2015 blob had a large effect on coastal waters and inlets, leading to the failure of spawning by invertebrates, changes to larval fish abundance, and an increase in phytoplankton species associated with harmful algal blooms (Nielsen et al., 2021; Shanks et al., 2020; Zhu et al., 2017). However, during the 2019 MHW, temperature anomalies near the coast were lower than those observed in 2015 (Ross et al., 2021). Although coastal systems and deep-water fjords did not seem to be affected as drastically during the 2019 MHW (Ross et al., 2021), this and previous studies indicate that these two MHW events may have had similar effects to offshore pelagic primary producers (Peña et al., 2019).

The 1997-1998 El Niño warming event also had similar effects on temperature, nutrient distributions and primary producers in the NE Pacific. In 1997/1998, there was a large area of nutrient depletion in the NE Pacific that was much more expansive than the following year (Whitney and Welch, 2002). The area of NO_3^- and $Si(OH)_4$ depletion was approximately 250,000 km^2 greater than 1999 and nutrient drawdown occurred approximately one month earlier than is typical for the region (Whitney and Welch, 2002).

Increased stratification during both the 2015 and the 2019 MHWs led to intense nutrient depletion in regions that do not usually experience prolonged NO_3^- and $Si(OH)_4$ limitation (Peña & Varela, 2007; Whitney & Freeland, 1999). In 2015, the increased warming and lower wind activity led to enhanced stratification which inhibited the resupply of deep-water nutrients to the surface ocean (Bond et al., 2015; Di Lorenzo & Mantua, 2016; Peña et al., 2019). This resulted in a nutrient depleted surface area that stretched farther offshore than usual, and a decrease in phytoplankton biomass from ~P4-P20. Peña et al (2019) showed also an increase in the dominance of cyanobacteria during this event. As in 2015, the surface temperature anomalies along Line P in 2019 were highly pronounced and increased stratification likely inhibited nutrient resupply to the surface from mixing. Compared to non-MHW years, the zone where NO_3^- and $Si(OH)_4$ were below detectable levels extended much further offshore along Line P during both of these MHW events. In 2018 (a non-MHW year) the zone of low NO_3, $Si(OH)_4$, and PO_4 extended from ~126-135° W, while in 2019 this low nutrient zone extended from ~125° W to ~145° W. The extent of this nutrient depleted zone was similar in 2019 and 2015 (Peña et al., 2019) and suggests that in the future, similar nutrient depletion may occur during these events.

During both the 2015 and the 2019 MHWs, small-celled phytoplankton accounted for the majority of the total chl-a biomass from P4 to P20 (Peña et al., 2019). However, during both of these MHWs there was an increase in total chl-a and a contribution from cells >5 µm at the most oceanic station, P26, compared to other stations. Station P26 has been normally identified as a region dominated by small cells and low biomass of phytoplankton. Peña et al. (2019) theorize that during the 2015 MHW, stratification may have resulted in increased stability of the water column, leading to increased light availability and growth of larger phytoplankton cells (see section 2.5.2). Additionally, higher temperatures may have lead to increased growth efficiency of phytoplankton (Peña et al., 2019). The observation of higher $bSiO_2$, chl-a >5 µm, and a higher *f*-ratio at P26 in 2019 all suggest that similar mechanisms occurred during the 2019 MHW. While light availability may have increased during the MHW, surface dissolved [NO_3] and [$Si(OH)_4$] were also higher at P26 than all other Line P stations in 2019. This likely allowed primary production and biomass to remain higher at the end of the summer when sampling occurred. The overall effect of the 2019 MHW was similar to other historical ocean warming events that have been recorded in the NE Pacific.

2.5 Conclusions

When comparing oceanic conditions during the summers of 2018 and 2019, some differences in physical, chemical, and biological characteristics will undoubtedly be due to natural variation in the system and short sampling windows. However, trends become more robust when they are compared to previous MHW events. While 2019 alone may not provide a complete picture, similarities to conditions in 1997/1998 and 2013-2015 suggest that there are some processes that are affected by these extreme MHW events. Increased stratification, changes in phytoplankton assemblage composition, and dissolved nutrient concentrations seem to be

commonalities between all MHWs in the NE Pacific. It should also be considered that apart from these extreme events, average ocean temperatures are continuing to rise, meaning that even non-MHW years are much warmer than pre-industrial averages. So, while MHWs are extreme events, they are also an indication of potential "new normal" states for many areas of the ocean.

The overall effects of the 2019 MHW on phytoplankton are somewhat straight forward; a warm and stratified water column led to a nutrient-depleted surface ocean that appeared to produce less primary producer biomass while not significantly affecting instantaneous uptake rates. However, there were several anomalies, particularly at P4 and P26 that were more pronounced. P4 had a considerable decrease in both primary producer biomass and new productivity that coincided with low nutrients and very warm euphotic zone waters. P26, conversely showed an increase in $bSiO_2$, chl-a derived from large cells, and new productivity. The mechanisms that led to the observations in August 2019 are important to interpreting the measurements and assessing potential impacts. For example, was nutrient depletion simply due to decreased mixing, or was there increased biological drawdown earlier in the growing season, or both? Both have implications for the magnitude of C export as well as secondary production in the region, but, the latter may have more severe implications for the match-mismatch dynamics of trophic interactions in the region (Cushing, 1990; Durant et al., 2019). Simply, zooplankton and larval fish populations may sharply decline if they are not able to respond to earlier changes in prey abundance (Durant et al., 2019). The similarities that were evident between the 2019 MHW and warming events such as the 1997/1998 ENSO event (Whitney et al., 1998; Harris et al., 2009) and the 2015 blob (Peña et al., 2019) are a good indication that observed changes in nutrient concentrations, water column properties, productivity and biomass may be associated with warming events. These commonalities will likely be features of future

MHWs and should be studied in more detail. Specific attention should be given to stations at opposite ends of the transect, P26 and P4, where the magnitude of change appears to be most severe during these events.

Chapter 3: Kinetics of nitrate and silicon uptake rates in phytoplankton from the subarctic NE Pacific Ocean during the 2019 marine heatwave

3.1 Introduction

3.1.1 Kinetics of nutrient use by phytoplankton

All phytoplankton must take up dissolved nutrients from their environment for growth (Bristow at al., 2017). The rate and quantity of nutrient uptake is affected by many environmental and physiological parameters such as the concentration of the nutrient in the environment, the number of cellular transporters, the size and surface area to volume ratio of the cell, and the affinity of the transporter for the nutrient (Shuter, 1978; Button, 1983; Lindemann et al, 2016). If phytoplankton cells relied on passive diffusion alone, any increase in dissolved nutrients would lead to an increase in uptake due to increases in the chemical gradient over the cell membrane. However, nearly all microbes, including phytoplankton, employ active cellular transport in order to acquire enough essential nutrients to facilitate growth and reproduction. In this case, the "uptake rate" will not only be limited by the concentration of the nutrient but also by the number and efficiency of cellular transporters that facilitate uptake into the cell. The "uptake rate" can be viewed as a product of the nutrient concentration and affinity (Fisken at al. 2013; Lindemann at al. 2016). While both concentration and affinity may change, affinity is bounded by physiological parameters; usually, this is a functionally constant value for a particular organism or group. So, for phytoplankton with a set affinity, there will be some concentration of nutrient at which the "uptake rate" will be saturated (Michaelis and Menten, 1913; Lobban & Harrison, 1994; Lindemann at al, 2016).

Phytoplankton that have a higher affinity for nutrient uptake will reach this saturation more rapidly (i.e. steeper slope) at lower nutrient concentrations. This affinity can be estimated by calculating the substrate concentration that results in half the maximum uptake rate (1/2 V_{max}). This is referred to as the half saturation constant (K_s). Both absolute and specific uptake rates as a function of substrate concentration can be expressed by the Michaelis-Menten (MM) equation (3.1) (Michaelis and Menten, 1913; MacIsaac & Dugdale, 1969). For example, for specific uptake rate:

$$V = \frac{V_{max} * S}{K_m + S} \qquad (3.1)$$

Where *V* is the measured specific uptake rate (expressed in units of inverse time, e.g. h^{-1},day^{-1}), V_{max} is the maximum specific uptake rate, S is the substrate or nutrient concentration, and K_m is the half saturation constant. When used as part of the MM equation, K_m is often referred to as the Michaelis-Menten (MM) constant. By measuring ambient uptake rates at various substrate concentrations, the parameters K_m and V_{max} can be calculated from the MM equation. In the equation, specific uptake rate (V) can also be substituted with the absolute uptake (ρ, expressed in units of concentration per unit volume per time, e.g. µmol L^{-1} day^{-1}). While V_{max} is related to cellular specific uptake (or the intrinsic ability of a cell to take up a nutrient) in 1/time units; ρ_{max} is reflective of the total amount of a nutrient taken up by unit volume/mass (e.g. by an entire assemblage) and per unit time, and can be more useful for *in-situ* measurements.

Low K_m values are usually associated with high nutrient affinity (Button, 1983) and uptake rates that are saturated at lower concentrations. High K_m values indicate the phytoplankton have lower affinity for the nutrient and reach their V_{max} at a higher nutrient concentration. Often, K_m values are used to compare physiological differences in uptake affinity

(and hence growth) among phytoplankton species (Edwards et al., 2013; Fiksen et al., 2013; Lindemann et al., 2016). In addition, K_m of a natural phytoplankton assemblages can be used as a way to compare the affinity of nutrient uptake by assemblages in different oceanographic environments (Krause et al., 2012; MacIsaac & Dugdale, 1969; Nelson & Brzezinski, 1990). Phytoplankton assemblages with overall low K_m will reach maximum uptake at lower substrate concentrations and will be more efficient at using dissolved nutrients in the environment. In contrast, assemblages with a high K_m show less affinity for a nutrient and will only reach maximum uptake during times when dissolved nutrients in the water column are high. The latter assemblages will become nutrient limited sooner if nutrients fall below optimal concentrations. Additionally, assemblages with a higher V_{max} may result in higher overall biomass than those with lower V_{max}, assuming that other nutrients and environmental variables are optimal for growth. Like K_m, V_{max} is useful when comparing production of phytoplankton assemblages across different oceanographic regimes.

3.1.2 Nitrogen use by phytoplankton

Nitrogen (N) is a key element for phytoplankton in marine systems but it is often a limiting nutrient that can inhibit the growth of phytoplankton (Bristow et al., 2017). The extent to which N is limiting differs depending on both the physiological traits of the phytoplankton assemblage as well as the concentration of N in the water column. Although phytoplankton can use many different forms of oxidized and reduced N (Carpenter et al., 1972; Fisher & Cowdell, 1982), nitrate (NO_3^-) is often the most readily available and utilized N source. In systems with high nutrient turnover rate, regenerated forms of N such as ammonium (NH_4^+) and Urea (CH_4N_2O) may also play a significant role. Primary production that is derived from NO_3^- utilization is referred to as “new production” while production that used reduced forms of N is “regenerated

production". Measuring new production can be specifically useful as it has traditionally been used as a proxy for C export from a system (Eppley & Peterson, 1979). Assemblages with higher new production will, normally, export C from the surface waters much more effectively than those that rely on regenerated N, and so are particularly important for removing C from the atmosphere via the biological C pump.

The ratio of NO_3 uptake to total N uptake is referred to as the *f*-ratio; the higher the f-ratio, the more new production in a system. When the f-ratio is low, it indicates that phytoplankton are more dependent on regenerated forms of N such as NH_4^+ and urea. For these systems, processes such as grazing, decomposition, and bacterial activity will be important determining factors for how N is delivered to the system.

In plants and phytoplankton, N uptake is highly mediated by the enzyme nitrate reductase (NR) which reduces NO_3 to NO_2, a crucial step for N to be incorporated into cellular proteins. The activity of NR is thought to highly influence the efficiency of N uptake for most phytoplankton groups. Thus, even in NO_3-replete waters, sub-optimal conditions for NR can lead to overall lower kinetic efficiency and uptake of NO_3 (Beevers & Hageman, 1969; Lomas & Glibert, 2000; MacIsaac & Dugdale, 1969). For example, the activity of NR is highly influenced by bioavailable Fe concentrations as catalytic Fe is required for the reduction of both NO_3 and NO_2 (Salisbury and Ross, 1978; Morel, 1986, Raven, 1988). Under Fe limitation, NR activity in phytoplankton can be reduced by up to 50 percent (Timmermans et al., 1994). Additionally, factors such as temperature are important for enzyme activities and studies have shown NR activity increases with higher temperatures in cultures (Berges et al., 2002; Coyne et al., 2021; Gao et al., 2000; Lomas & Glibert, 2000) but the implications of this during MHWs are not well shown.

3.1.3 Silicon use by plankton

Diatoms (Bacillariophycea), silicoflagellates (Dictyochales), and even some cyanobacteria (Synechococcus) are algal groups that utilize Si. However, in most modern marine environments, diatoms are by far the dominant users of Si, predominantly by uptake of the dominant dissolved form, silicic acid ($Si(OH)_4$) (Stumm & Morgan, 1996; Kristiansen & Hoell, 2002; Martin-Jezequel et al, 2003;). Due to their obligate Si requirement, to build their silica (SiO_2) frustules, diatom growth can become limited if concentrations of $Si(OH)_4$ are low (Lewin, 1962). In the world's oceans, [$Si(OH)_4$] in the euphotic zone can vary by up to three orders of magnitude (Levitus et al., 1993) but Si uptake rates (ρSi) are nearly always undersaturated (Kristiansen & Hoell, 2002). However, these observed undersaturated ρSi rates may not always indicate limitation. Diatoms can alter their acquisition of Si and their silicification to accommodate low [$Si(OH)_4$], therefore, decreases in ρSi that correspond to low [$Si(OH)_4$] are not necessarily the result of Si limitation (Krause et al., 2012). Additionally, the V and K_s values for $Si(OH)_4$ (as well as other nutrients) can be altered significantly in response to the availability of micronutrients such as iron (Fe) and zinc (Zn), which is particularly important in HNLC regions where trace metals are limiting (Rocha et al., 2000; Laynaert et al., 2004).

While Si limitation does not affect all phytoplankton groups as N limitation does, in areas where diatoms are the dominant group, Si limitation often occurs before N limitation. Therefore, in these systems, the overall primary production can be limited by $Si(OH)_4$ rather than by NO_3^- (Bristow et al., 2017). This is particularly true for the HNLC regions of the NE Pacific, where Fe and $Si(OH)_4$ limitation have been previously assessed (Brzezinski et al., 2022; Rocha et al., 2000; Whitney et al., 2005). In order to determine whether Si limitation is occurring in natural assemblages, Krause et al. (2012) suggested using a ratio of ambient (V_{amb}) to maximum (V_{max}) uptake rates, in which V_{amb} is the uptake rate measured at the ambient concentration of $Si(OH)_4$.

A V_{amb} <25% of V_{max} (i.e. V_{amb}:V_{max} <0.25) indicates Si limitation (Krause et al., 2012). This proxy can be used to assess the extent of Si limitation in the oceanic subarctic NE Pacific, where diatoms are also under trace metal limitation that affects ρSi.

While enzymes such as NR and its effect on N incorporation are well studied in phytoplankton, transporters involved in the uptake of $Si(OH)_4$ are somewhat less well understood. A group of membrane associated proteins are thought to mediate $Si(OH)_4$ uptake in diatoms (Hildebrand et al., 1997; Thamatrakoln & Hildebrand, 2008). However, there is much less research on the potential effects that temperature will have on $Si(OH)_4$ uptake and incorporation. In some freshwater and marine diatoms, $Si(OH)_4$ uptake rates become greater at warmer temperatures (van Donk & Kilham, 1990) as does the extent of silicification (Blank et al., 1986). However, other studies with marine polar diatoms have found that Si uptake will decrease with temperature (Durbin, 1977). Therefore, it is probable that any response of Si uptake to changes in temperature will be region or species-specific and examination of *in-situ* Si uptake and incorporation will be useful in determining potential changes to Si kinetics and the Si cycle.

In August of 2019, I conducted on-board incubation experiments to measure NO_3^- and $Si(OH)_4$ uptake rates at increasing nutrient concentrations at ten locations from the Vancouver Island coast seaward to Ocean Station Papa (P26) in the Alaskan Gyre. From these experiments, I estimated V_{max} and K_m for NO_3^- and $Si(OH)_4$, which were used to assess the extent of nutrient limitation and efficiency of uptake during the 2019 MHW over a large area in the NE Pacific. Ambient nutrient concentrations, biological particulates and ambient C uptake rates were also measured at the same stations. Data that was collected during the summer 2019 Line P research cruise is also discussed in chapter 2 of this thesis.

3.2 Materials and Methods

3.2.1 Sampling and hydrography

Field work was conducted as part of the Department of Fisheries and Oceans' (DFO) La Perouse and Line P Oceanographic research programs. Sampling was conducted at five major stations along the Line P transect during August 2019, and at six stations on the West coast of Vancouver Island during the La Perouse cruise in September 2019 (Table 3.1). Stations are categorized as "on-shelf" if the bottom depth was <200 m, "off-shelf" if the water depth was between ~200-2000 m and "oceanic" if the bottom depth was >2000 m (Table 3.1). A complete suite of samples was collected at each station except at LB01 where uptake rate experiments were not conducted due to time constraints

Table 3.1. Station locations, sampling dates, and physical characteristics of stations sampled in 2019 during the summer Line P and La Perouse cruises.

Station	Latitude N	Longitude W	Date Sampled DD-MM-YY	Bottom Depth m	MLD m	Station setting
P4	48.65	-126.67	16-08-19	1300	19	Off-shelf
P12	48.97	-130.67	17-08-19	3300	18	Off-shelf
P16	49.28	-134.67	19-08-19	3550	21	Oceanic
P20	49.57	-138.67	20-08-19	3890	23	Oceanic
P26	50.00	-145.00	24-08-19	4300	29	Oceanic
LB01	48.67	-124.99	30-08-19	35	8	On-shelf
LB15	48.07	-126.14	31-08-19	1559	27	Off-shelf
LC06	48.61	-125.95	01-09-19	92	13	On-shelf
LG09	48.92	-127.22	02-09-19	2075	13	Off-shelf
LBP3	50.05	-127.92	03-09-19	168	10	On-shelf
CS02	50.69	-129.47	05-09-19	1896	6	Off-shelf

La Perouse and Line P cruises were conducted back-to-back and are therefore referred to as August-September 2019 cruise. For both regions, sampling was conducted aboard the CCGS John P Tully using a conventional rosette system equipped with 24 ten-litre Niskin bottles and a SeaBird SBE 19-Plus conductivity, temperature, depth (CTD) probe.

At each station, seawater samples were collected from the mixed layer (5 m; approximately 50% optical depth) and the chl-max depth. All samples were collected in clean containers, processed immediately after sampling and stored appropriately until analyses were performed at UVic.

3.2.2 Dissolved nutrients concentrations

Samples were collected, processed, and analyzed following the same procedure outlined in section 2.2.2.

3.2.3 Biological particulate concentrations

Samples were processed and analysed following the same procedure outlined in section 2.2.3 (Chlorophyll-a), 2.2.4 (Biogenic Silica), and 2.2.5 (Particulate carbon and N).

Particulate phosphorous (PP) was also measured during August-September 2019. A volume of 2.8 L of seawater was collected from the Niskin sampler into a clean, acid-washed polycarbonate bottle. The entire seawater sample was gently vacuum filtered onto a pre-combusted, 47 mm, 0.7 µm (nominal porosity) glass fibre filter and rinsed with sodium sulphate ($NaSO_4$) to prevent retention of dissolved phosphate onto the filter. Filters were placed into foil envelopes and kept at -80 ˚C until analysis. Particulate phosphorous was processed following the ash-hydrolysis digestion described by Lomas et al. (2010) to convert all particulate phosphorous to dissolved PO_4. Concentrations of dissolved PO_4 were measured by the dissolved phosphate colorimetric method described by Parsons et al. (1984) and Strickland & Parsons (1972).

Chl-a data are presented as both depth-discrete values (i.e. concentration at the 5 m depth), and depth-integrated values. Integration was done between the 5 m depth and the chl-max depth for both the <5 µm and the >5 µm size fractions.

3.2.4 Ambient carbon and nitrate uptake rates

Ambient C and NO_3^- uptake were measured at all stations except for LB01 where only particulates were measured. Samples were collected, incubated and processed following the same procedure outlined in section 2.2.6.

3.2.5 Ambient silicon uptake rate

At each station, except LB01, seawater samples were collected directly from the Niskin into ~300 mL clear, acid-washed, polycarbonate bottles. To each bottle, an aliquot of the radiotracer Si-32 (as 32Si(OH)4) was added to achieve an activity of 0.01 µCi/mL. Samples were incubated in the shipboard incubator following the same process as section 2.2.6.

After 24 h, samples were removed from the incubator and immediately filtered onto a 0.6 µM polycarbonate filter. All filters were dried for 24 h on a Teflon planchette before being covered with protective Mylar (polyethylene terephthalate) foil. Planchettes were then placed in plastic petri dishes and stored in a acrylic container until analysis. Samples were allowed to rest for a minimum of 120 days before analysis to allow for secular equilibrium between ^{32}Si and its daughter isotope ^{32}P (Krause et al., 2011)

Uptake rates of Si were determined by measuring the activity of ^{32}Si in particles on the filters using a Risø low-level gas flow beta multi-counter system, following the method outlined by Brzezinski & Phillips (1997) and Krause et al. (2011). Si production rates (ρSi) were calculated using the following equations from Brzezinski & Phillips (1997):

$$\left[\mathrm{bSiO_{2_{new}}}\right] = \left(\mu\mathrm{Ci}\ {}^{32}\mathrm{Si_{PSi}} / \mu\mathrm{Ci}\,{}^{32}\mathrm{Si_{tot}}\right) * \left[\mathrm{Si(OH)_4}\right] \quad (3.2)$$

$$\rho\mathrm{Si} = \left[\mathrm{bSiO_{2_{new}}}\right]/\mathrm{t} \quad (3.3)$$

Where µCi $^{32}Si_{Psi}$ is the activity of particulate ^{32}Si measured on the filter at the end of the incubation, µCi $^{32}Si_{tot}$ is the total activity of ^{32}Si added to the sample at the start of the incubation, $[Si(OH)_4]$ is the concentration of silicic acid at the start of the incubation (this is the ambient value plus any addition or enrichment to the sample), and t is the incubation time.

3.2.6 Nitrate kinetics

Seawater samples were collected directly from the Niskin bottles into seven separate 580 mL acid-washed, clear polycarbonate bottles. Samples were enriched with a solution of sodium nitrate ($Na^{14}NO_3$) to achieve 1, 2, 3, 4, 8, 12, and 20 µM NO_3 above the ambient NO_3 concentration. To each of the bottles, the stable isotopic tracer $Na^{15}NO_3$ was added to achieve approximately 10% of ambient (or ambient +enriched) NO_3. Samples were incubated following the procedure outlined in section 2.2.6 and uptake rates were also calculated following the same procedure as section 2.2.6. The maximum ρNO_3 (ρ_{max}) and the MM constant (K_m) were calculated by fitting the experimental data to the Michelis-Menten equation (MacIsaac & Dugdale, 1969) using RStudio v4.2.1 (R Core Team, 2022).

3.2.7 Silicon kinetics

Seawater samples were collected into seven ~300 mL clear, acid-washed, clear polycarbonate bottles. Samples were enriched with a $Si(OH)_4$ solution to achieve 1, 2, 3, 4, 8, 12, and 20 µM $Si(OH)_4$ above the ambient $Si(OH)_4$ concentration. To each bottle, an aliquot of the radiotracer Si-32 (as $^{32}Si(OH)_4$) was also added to achieve an activity of 0.01 uCi/mL. Samples were incubated following the same procedure as section 2.2.6.

After 24 hr, samples were processed and uptake rates calculated following the same procedure as section 3.2.5.

The maximum ρSi (ρ_{max}) and the MM half-saturation constant (K_m) were calculated by fitting the experimental data to the Michelis-Menten equation (M. Brzezinski et al., 1998; MacIsaac & Dugdale, 1969; Nelson et al., 2001) using RStudio v4.2.1 (R Core Team, 2022).

3.3.7 Taxonomic composition of phytoplankton assemblages

Seawater samples were collected directly from the Niskin bottles into clean 250 mL amber glass or plastic containers. Samples were spiked with a 1:1 mixture of buffered formaldehyde and Lugol's potassium iodine solution, and stored at 4° C until analysis. The Utermöhl method (Lund et al., 1958) and brightfield microscopy were used for identification and quantification of main phytoplankton groups. Between 50 mL and 100 mL were settled for each sample. Identification and counts were performed using an Olympus IX-71 inverted epifluorescence microscope. Phytoplankton cells were identified to the lowest possible taxon, and grouped into taxonomic categories. The categories were diatoms, dinoflagellates, ciliates and other flagellates, and coccoid cells <5 µm. Coccoid cells were those that were too small to be reliably identified and may represent a mix of several taxa.

Although not all dinoflagellates, other flagellates, and ciliates are strictly photoautotrophic, they were counted as part of the phytoplankton assemblage as many genera observed in the samples are known to be mixotrophic and contribute to nutrient uptake, photosynthesis and particulate concentrations at the phytoplankton trophic level (Dagenais-Bellefeuille & Morse, 2013; Stoecker et al., 1989).

3.3 Results

The following results focus on samples collected from the mixed layer (at 5 m) where kinetic experiments were performed. Full data sets which include all chl-max depth data are presented in Appendix II (Table A6). Data from summer 2019 along Line P is the same data discussed in chapter 2 of this thesis.

3.3.1 Temperature and dissolved nutrient concentrations

Seawater temperatures at 5 m reached a maximum of 17.7 °C at P4 in August-September 2019 (Figure 3.1). The temperatures were highest in the region between P4 and P16. This includes high temperatures measured at LG09 and LB15 which are at similar locations to P4. Stations on the southern Vancouver Island coast (LB01, LC06) had the lowest temperatures (12-13 °C) of all the stations sampled in August-September 2019.

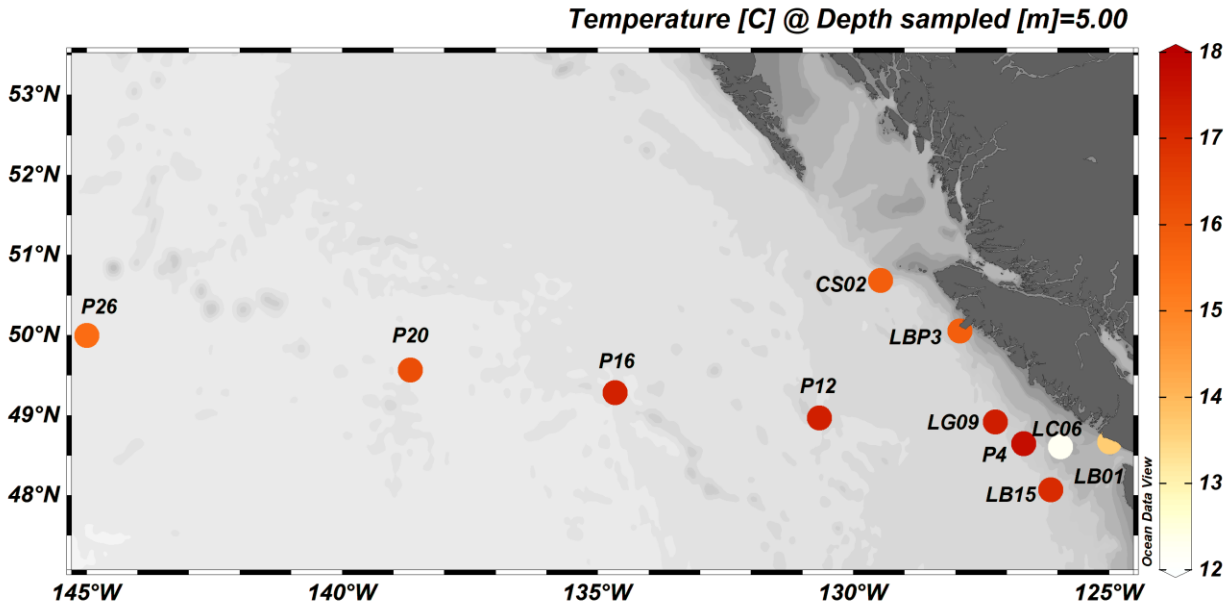

Figure 3.1. Seawater temperatures (°C) measured at 5 m for Line P and La Perouse stations in August-September 2019.

Dissolved NO_3, $Si(OH)_4$ and PO_4 followed similar patterns of distribution in August-September 2019 (Figure 3.2). NO_3 was highest (0.98 µM) at P26 and was low (<0.6 µM) but detectable at most on-shelf stations. NO_3 was below the LoD (0.1 µM) at LB15 and all Line P stations from P4-P20. $Si(OH)_4$ had a slightly more variable pattern of distribution compared to NO_3, and reached the highest levels (>40 µM) at LC06 and LB01. [Si(OH)4] were lower, but above the LoD at P26, P4, and CS02 (7.7, 1.2, and 9.2, respectively). All other stations had [$Si(OH)_4$] below the LoD (0.3 µM). [PO4] were very similar (0.2-0.4 µM) at all stations except at LB01 and LC06 were concentrations were elevated (1.6-1.7 µM).

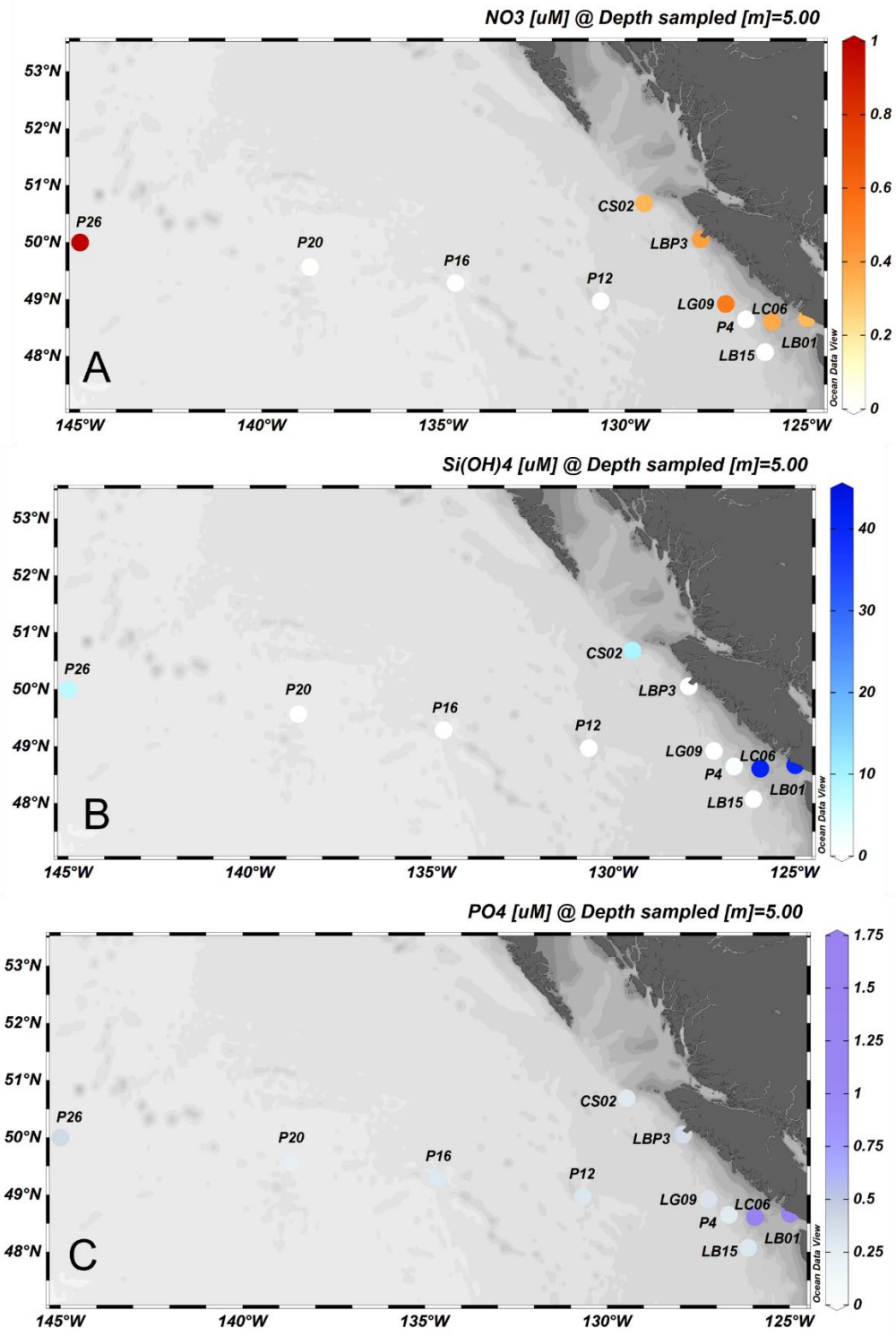

Figure 3.2. Dissolved A) NO_3, B) $Si(OH)_4$, and C) PO_4 from the mixed layer (5 m) at Line P and La Perouse stations in August-September 2019.

3.3.2 Biological particulate concentrations

All biological particulates in the mixed layer had similar patterns of longitudinal distribution over the study area. Total Chl-a, PC, and $bSiO_2$ were higher at the on-shelf stations, were comparatively lower between P4-P20, and then increased slightly at P26. This increase in biological particulates is not usually seen at P26 and represents an anomalous event. Total chl-a measured at 5 m was highest at LB01, LC06, and CS02 (2.88, 1.88, and 1.3 µg L^{-1}, respectively). P4 and P12 had the lowest chl-a observed in the entire study area at 0.09 and 0.1 µg L^{-1}, respectively (Figure 3.3 A).

PC and PN had nearly identical distributions (Figure 3.3 B and C) with more elevated concentrations of PC and PN at La Perouse stations compared to most Line P stations. CS02 had the highest PC (364.8 µg L^{-1}) and the second highest PN (0.9 µM). PC and PN had a somewhat variable longitudinal distribution along Line P. PC was very low at P4, P12 and P20 (97.1, 85.2, and 90.1 µg L^{-1}, respectively) and PN was similarly low (0.45, 0.39, and 0.39 µM, respectively). P16 and P26, had higher PC than other Line P stations (136.2 and 177.5 µg L^{-1}, respectively). P26, specifically, had the highest PN of all Line P and La Perouse stations at 0.97 µM.

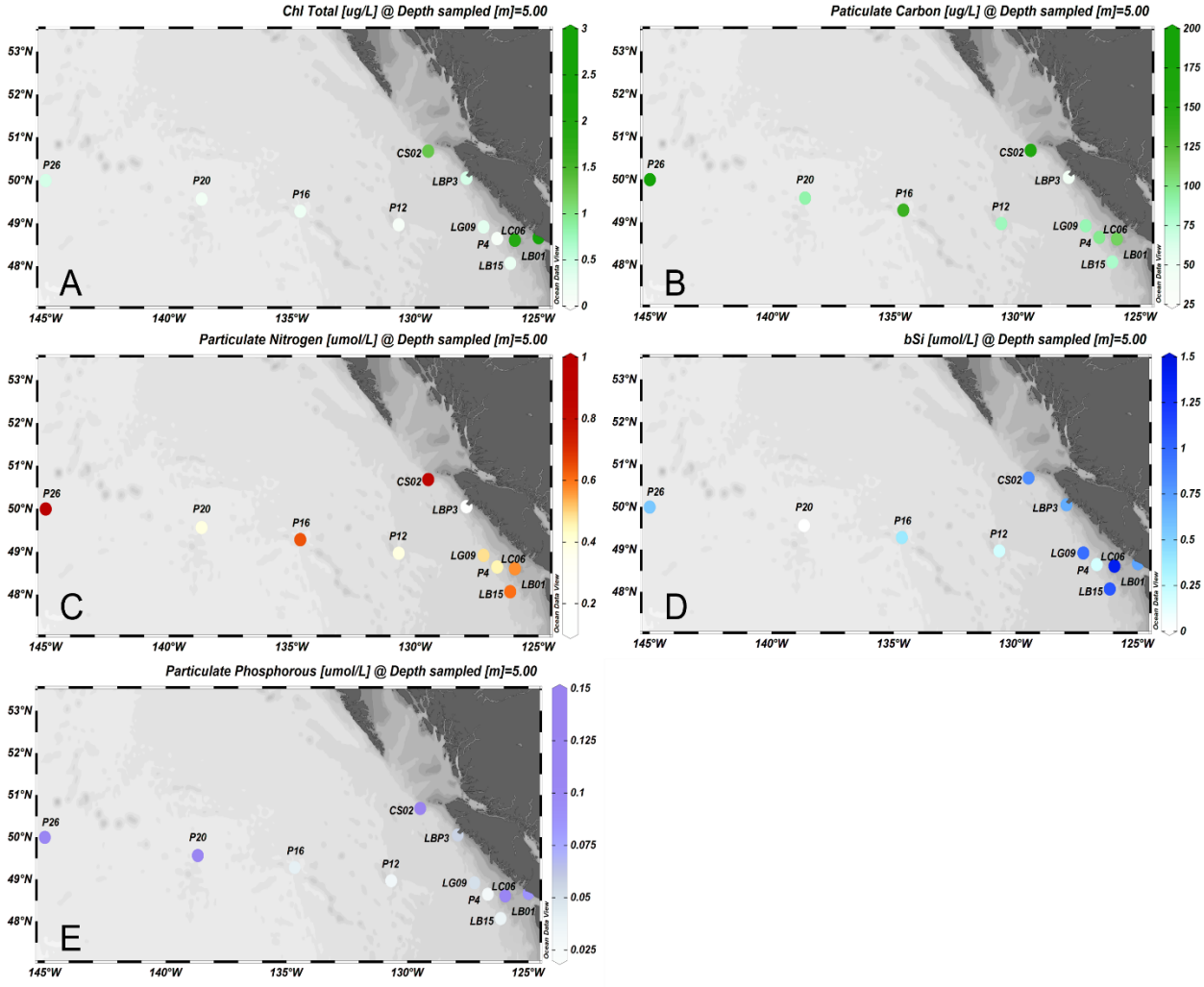

Figure 3.3. Biological particulates in August-September 2019 measured at 5 m at stations along Line P and La Perouse. Data presented are A) total chl-a (µg L^{-1}), B) Particulate Carbon (µg L^{-1}), C) Particulate Nitrogen (µmol L^{-1}), D) Biogenic silica (bSi) (µmol L^{-1}), and E) Particulate Phosphorous (µmol L^{-1}).

Ambient [$bSiO_2$] at 5 m depth were much higher at the La Perouse than the Line P stations overall (Figure 3.3 D) reaching maximum values of 1.40 µM at LC06. [$bSiO_2$] were similarly high at LB15 (1.10 µM) and LG09 (0.98 µM). Of all the Line P stations, P26 had the highest [$bSiO_2$] at 0.54 µM which is anomalous in the region based on historical data. The on-

shelf stations , inland of P4, normally have the highest biomass and production rates while P26 remains at relatively low concentrations of biological particulates.

Cells smaller than 5 µm contributed the majority of chl-a at most stations. Depth-integrated size- fractionated chl-a data (Figure 3.4) showed that cells <5 µm in diameter were much more dominant at all stations, including on-shelf stations, but contribution from cells >5 µm was nearly equal at oceanic stations P20 and P26. LBP3 was the only station where chl-a was significantly higher in the fraction of cells >5 µm.

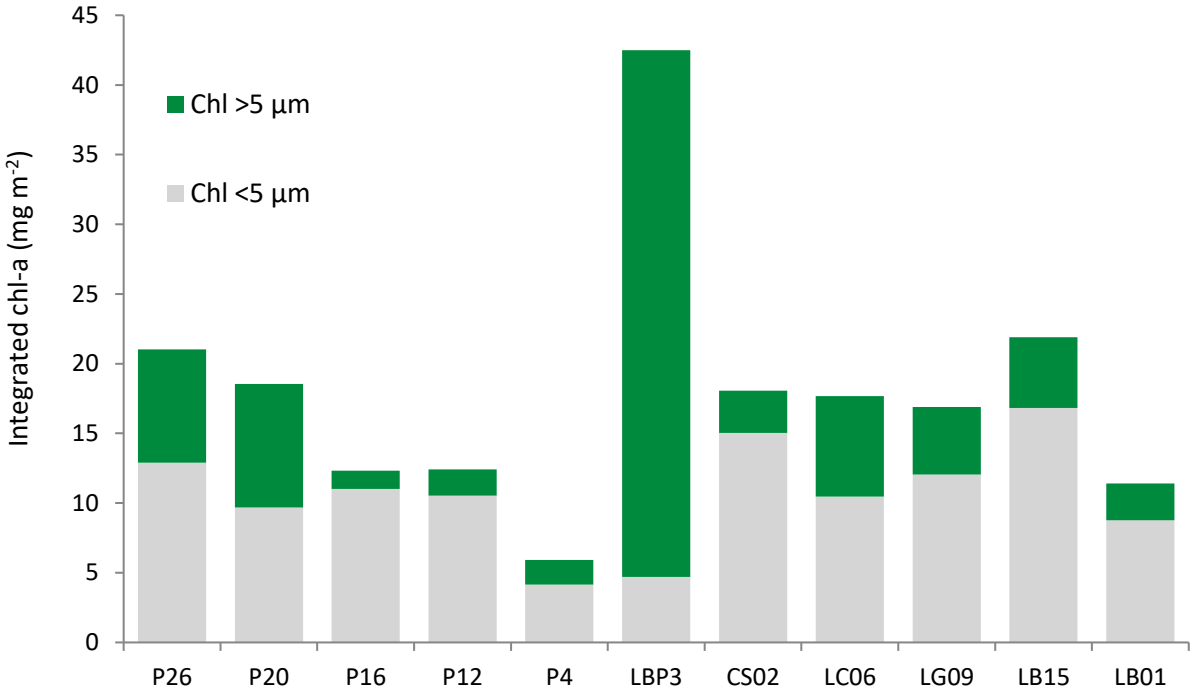

Figure 3.4. Depth-integrated size fractionated chl-a (mg m^{-2}) data from Line P and La Perouse stations in August-September 2019. Values are depth-integrated from 5 m to the chl-max depth of each station. On-shelf stations are LBP3, LC06, amd LB01, off-shelf stations are P4, P12, CS02, LG09, and LB15, oceanic stations are P16, P20, and P26.

3.3.3 Ambient carbon, nitrate and silicon uptake rates

Carbon uptake rates (ρC) in the mixed layer were highest at LC06, LBP3, and P26 reaching 59.3, 25.6, and 24.2 µg C L^{-1} day^{-1}, respectively (Figure 3.5 A). At all other stations, ρC was very similar (~8-12 µg L^{-1} day^{-1}) expect at CS02 where ρC was <1 µg L^{-1} day^{-1}.

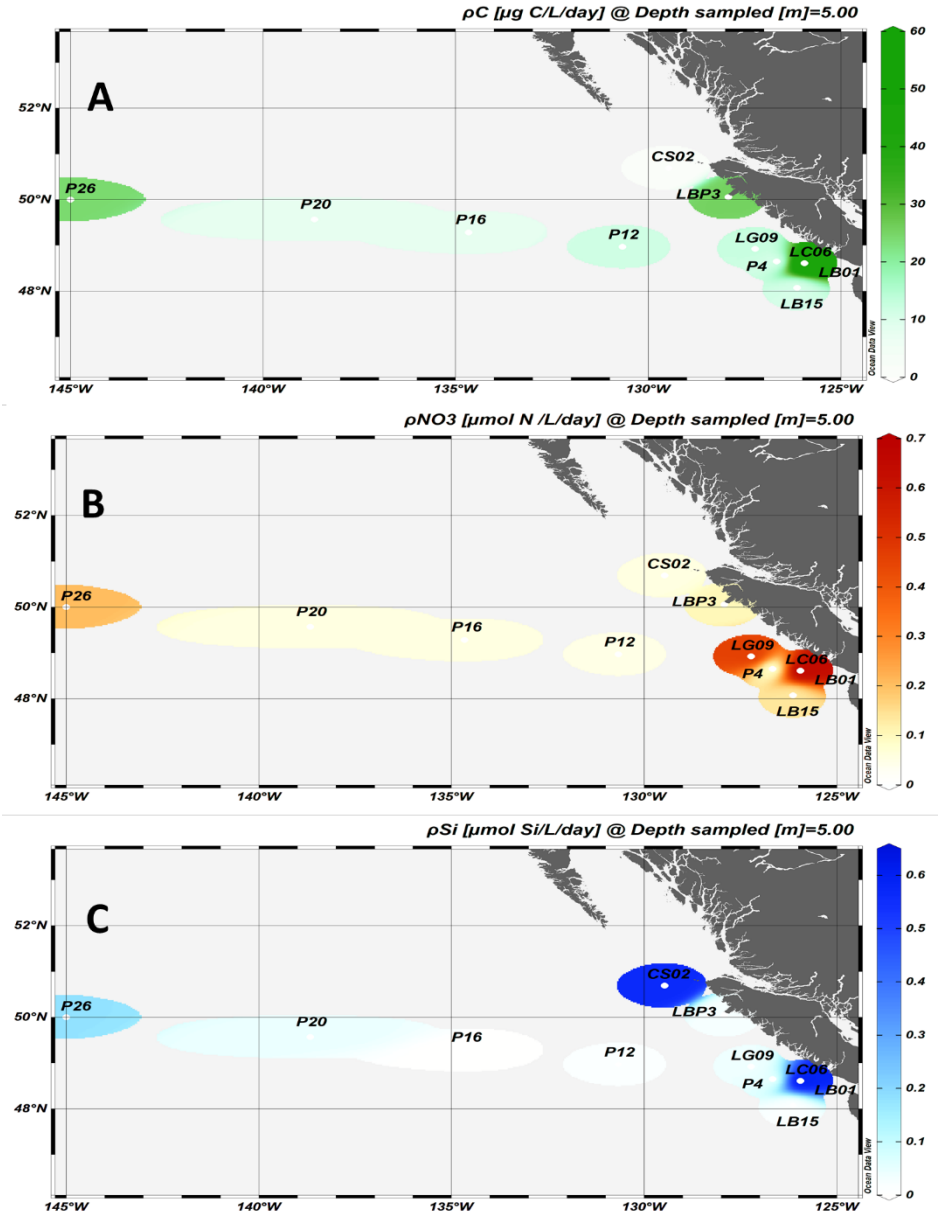

Figure 3.5. Ambient uptake rates of A) carbon (ρC), B) nitrate (ρNO_3), and C) silicon (ρSi) from 5 m at major Line P and La Perouse stations in August-September 2019.

Ambient ρNO_3 in the mixed layer was highest at LC06, LG09 and P26 where rates were 0.66, 0.47 and 0.21 µM day^{-1}, respectively (Figure 3.5 B). LB15 and LBP3 had similar rate of ρNO_3 (0.135 and 0.104 µM day^{-1}, respectively) and all other stations had very low NO_3 uptake <0.1 µM day^{-1}. Ambient ρSi was highest at La Perouse stations LC06 and CS02 (0.61 and 0.56 0.18 µM $day^{-1,}$ respectively). The next highest ambient ρSi was measured at P26, while rates were considerably lower than LC06 and CS02 at 0.18 µM day-1. Ambient ρSi rates were <0.1 µM day^{-1} at 5 m at all other stations in the Aug-Sep 2019 (Figure 3.5 C).

3.3.4 Nitrate uptake kinetics

Results from kinetic experiments conducted at La Perouse stations from the Vancouver Island coast indicated that ρNO_3^- increased with NO_3^- enrichement only at CS02 and LBP3 (Figure 3.6). All other La Perouse stations did not have any considerable increase in NO_3 uptake at any level of enhancement. Increases in ρNO_3 with enhancement (ie. the difference between ambient ρNO_3^- and maximum ρNO_3^-) ambient were large (> 0.5 µM day^{-1}) at CS02 but not at LBP3. Although ambient dissolved NO_3^- was below the LoD at all Line P stations, the only station that showed an increase in ρNO_3 with enhancement was P20. All other stations did not show a response to NO_3 enrichment (Figure 3.7).

The K_m and ρ_{max} for NO_3 uptake were calculated at all stations for both regions, except LG09 where uptake rates were not suitable for the fitting of a MM model (Table 3.2). La Perouse stations LC06 and CS02 had the highest K_m values of 4.68 and 0.83 µM, respectively. Similarly, most La Perouse stations had generally higher ρ_{max} values reaching 1.6, 0.8, ad 0.67 µM day^{-1} at LBP3, CS02, and LC06, respectively. Line P stations had lower K_m and ρ_{max} values with P12 having the lowest ρ_{max} for any station (0.08 µM day^{-1}) while the lowest K_m values (0.01 µM) were observed at P4, P16, and P26 (Table 3.2). The ratio of ρ_{amb}:ρ_{max} at all stations except CS02 was above the 25% , suggesting no significant NO_3 limitation (see section 3.1.3). CS02, however, had a ρ_{amb}:ρ_{max} of 10.45% which indicates that phytoplankton in the mixed layer at CS02 were NO_3 limited.

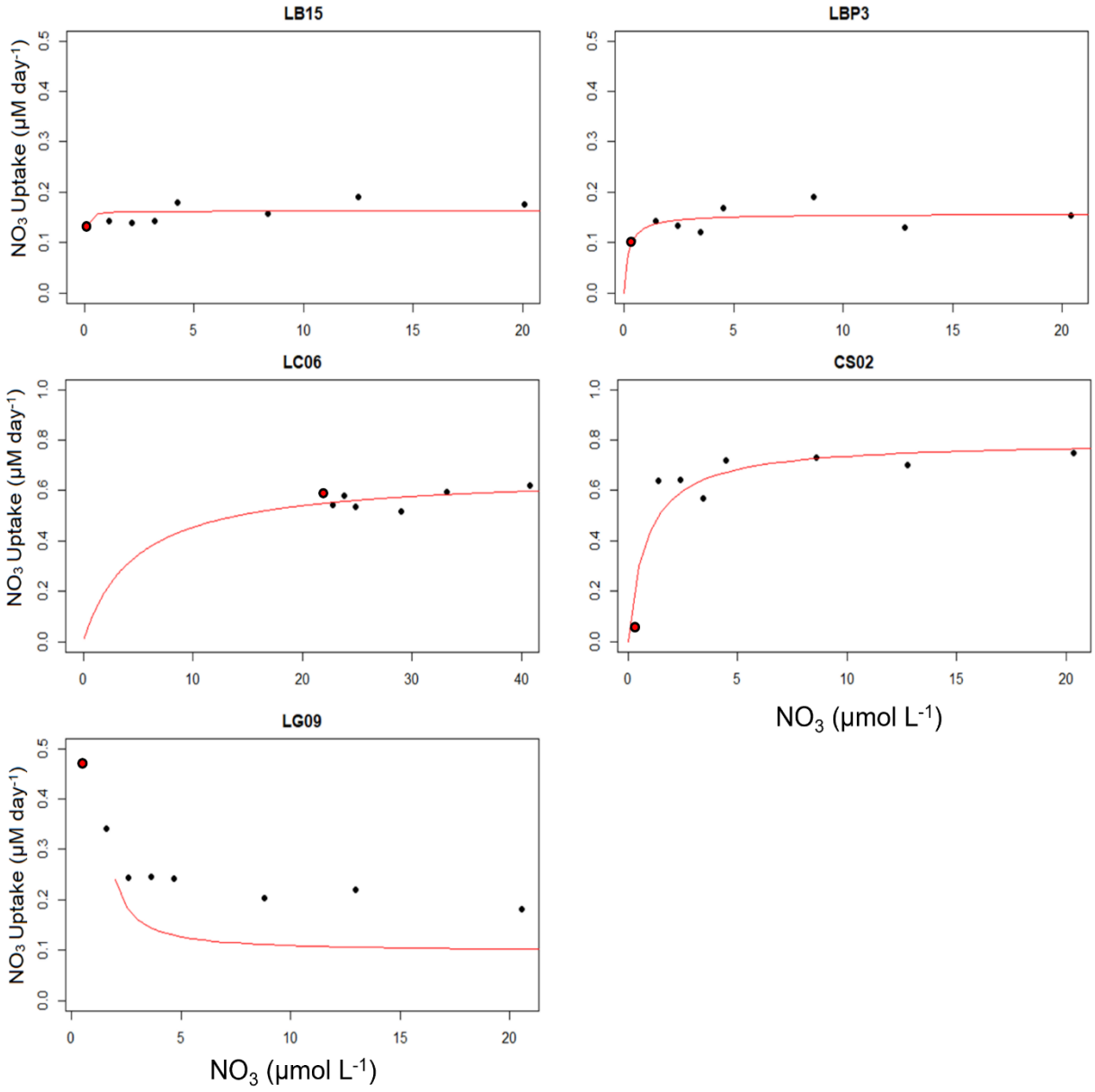

Figure 3.6. Results from nitrate uptake (ρNO_3) kinetic experiments at La Perouse stations during September 2019. Plots show NO_3 uptake rates (µM day^{-1}) at ambient value (red marker), all levels of enhancement (µM) (black markers) and modeled Michaelis-Menten curves fitted to the data (red lines; units of µM day^{-1}).

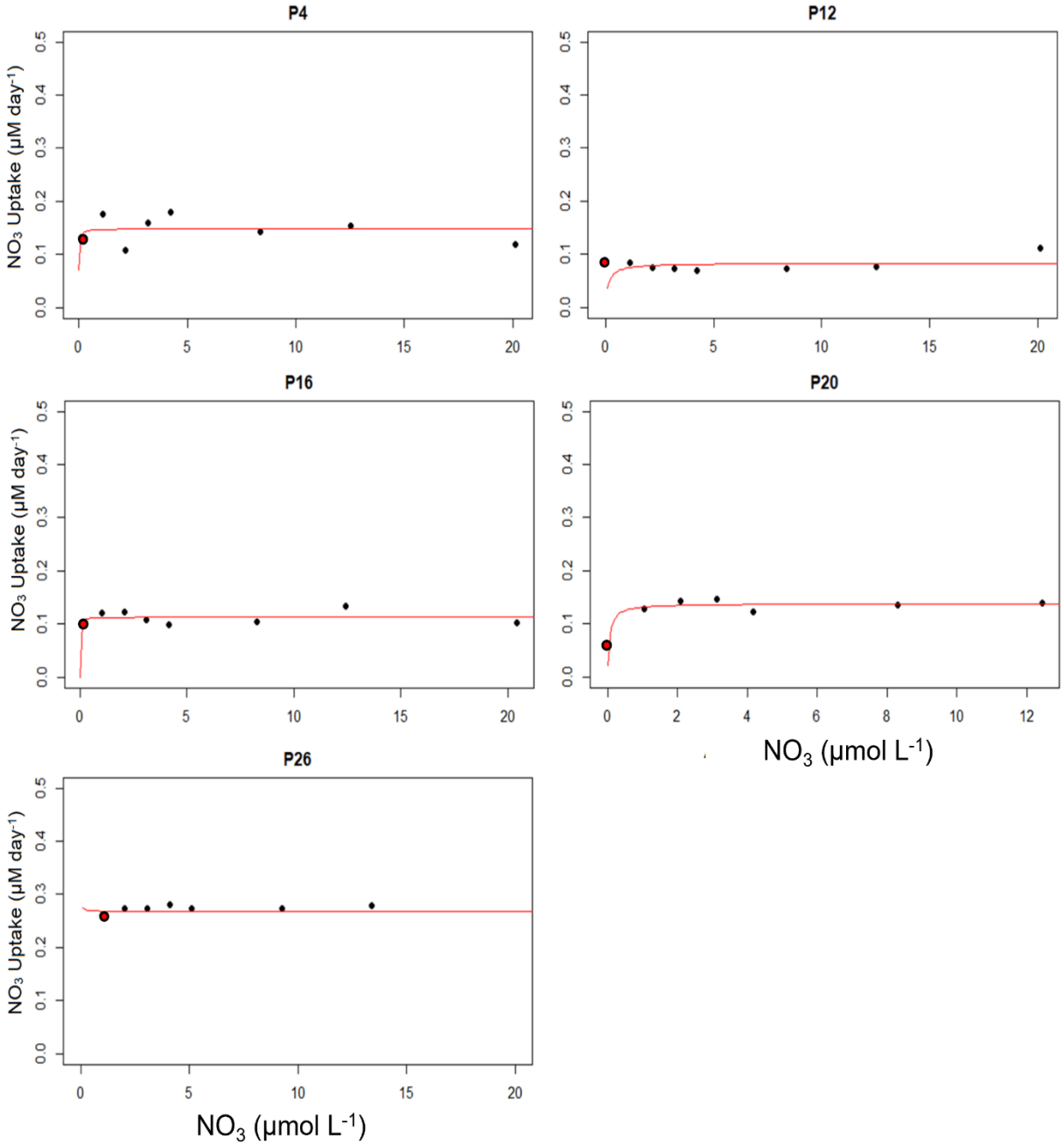

Figure 3.7. Results from nitrate uptake (ρNO_3) kinetic experiments at Line P stations during August 2019. Plots show NO_3 uptake rates ($\mu M\ day^{-1}$) at ambient (red marker), all levels of enhancement (µM) (black markers), and modeled Michaelis-Menten curves fitted to the data (red lines; units of $\mu M\ day^{-1}$).

Table 3.2. Maximum NO_3 uptake rate (NO_3 ρ_{max}), half saturation constants (NO_3 K_m) and ambient to maximum uptake ratios (ρ_{amb}:ρ_{max}) calculated from the MM-models fitted to the experimental data at La Perouse and Line P stations in August-September 2019. The station for which kinetic parameters could not be calculated is marked with NC (not calculated).

Station	NO_3 ρ_{max} μmol L^{-1} day^{-1}	NO_3 K_m μmol L^{-1}	ρ_{amb}:ρ_{max} %	Response to enhancement
P26	0.28	0.01	114.18	No increase
P20	0.14	0.053	130.12	Increase
P16	0.12	0.01	5961.27	No increase
P12	0.08	0.13	301.14	No increase
P4	0.15	0.01	148.58	No increase
CS02	0.80	0.83	10.45	Increase
LG09	NC	NC	NC	No increase
LB15	0.16	0.02	1088.12	No increase
LBP3	1.57	0.21	437.13	Increase
LC06	0.67	4.68	108.27	No increase

3.3.5 Silicon uptake kinetics

All La Perouse stations showed some increase in ρSi with Si enhancement to varying degrees. LB15, LG09, and LBP3 all appeared to be Si limited and had considerable increases in ρSi up to the 20 μM enhancement (Figure 3.8). These stations had very low ambient $Si(OH)_4$ and MM curves of both LB15 and LBP3 suggest that further Si enhancement would have resulted in further increases in ρSi. Although ambient [$Si(OH)_4$] in the mixed layer at LC06 were already >40 μM, there was some increases in ρSi with further enhancement (Figure 3.8). Station CS02 also had high dissolved [$Si(OH)_4$] >10 μM and although data allowed for fitting of the MM model, there was no substantial increase in ρSi between ambient (9 μM) and maximum (29 μM) concentrations of $Si(OH)_4$.

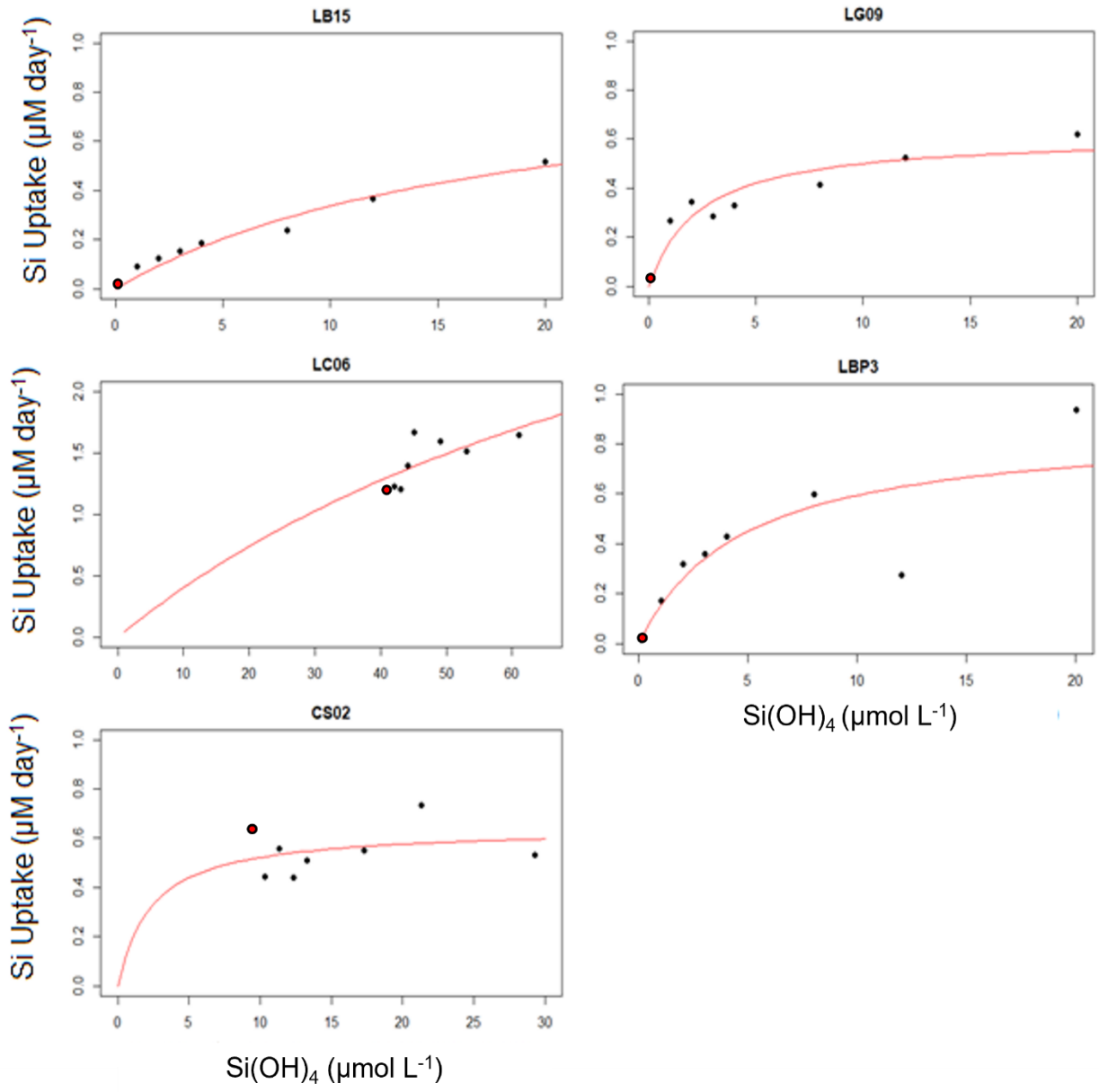

Figure 3.8. Results from $Si(OH)_4$ uptake kinetic experiments at La Perouse stations during summer 2019. Plots show $Si(OH)_4$ uptake at ambient values (red markers), all levels of enhancement (black markers), and modeled Michaelis-Menten curves (red lines).

Along the Line P transect, stations had a variable response to Si enhancement (Figure 3.9). P4 and P16 had no considerable increase in ρSi with enhancement except at the 20 µM concentration level. At both stations, ρSi was low and relatively consistent from ambient concentrations to the 12 µM enrichment, only increasing after an addition of 20 µM (Figure 3.9). P12 had no considerable increases with Si enhancement. P20 and P26 both had significant increased ρSi with enhancement (up to an order of magnitude at P20) and showed clear signs of Si limitation.

Maximum uptake (ρ_{max}) could be calculated at all stations except P20 and P4 because ρSi was not saturated at these two stations (Table 3.3). The measured ρ_{max} was highest at LC06, reaching levels of 1.65 day^{-1} but this may not represent the true ρ_{max} as uptake increased between the 40 and 60 µM $Si(OH)_4$ and no additional measurements was made with >60 µM $Si(OH)_4$. La Perouse stations had much higher ρ_{max} values compared to Line P stations overall. Of the Line P stations, P26 had the highest ρ_{max} measured at 0.38 µM day^{-1}. Half saturation constant (K_m) from the MM models could not be calculated at three stations, LC06, P4, and P20. LG09 and CS02 had the lowest Si K_m (2.33 and 2.34 µM, respectively) while LB15 and P26 had the highest (18.3 and 16.4 µM, respectively). For stations where ρ_{max} could not be calculated from the MM model, the ρSi from the 20 µM enrichment was used as ρ_{max} for the calculation of ρ_{amb}:ρ_{max} (Krause et al., 2012).

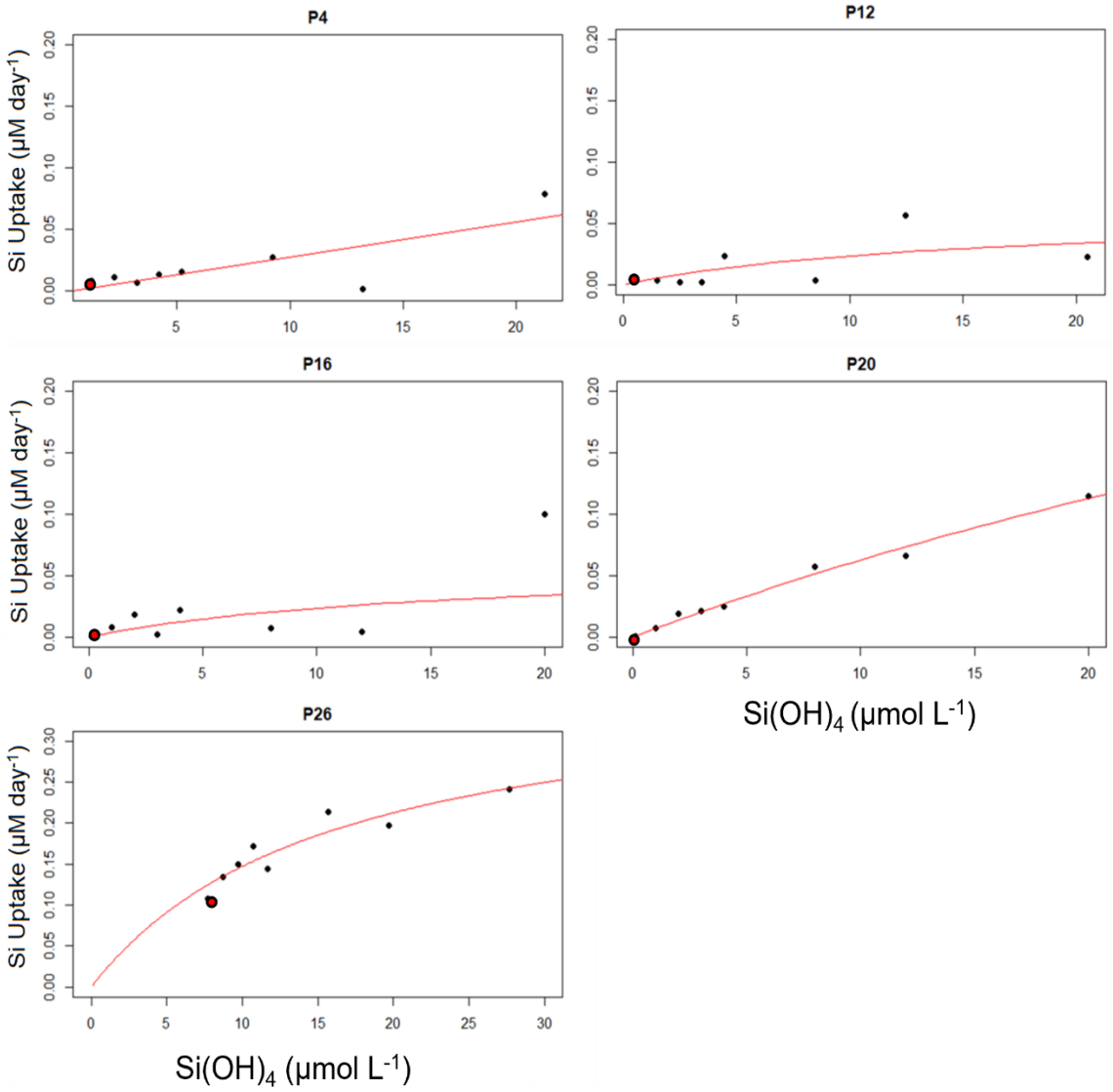

Figure 3.9. Results from $Si(OH)_4$ uptake kinetic experiments at Line P stations during summer 2019. Plots show $Si(OH)_4$ uptake at ambient values (red marker), all levels of enhancement (black markers), and modeled Michaelis-Menten curves (red lines).

Table 3.3. Silicon (Si) kinetic parameters calculated from the Michaelis-Menten models fitted to the experimental data at La Perouse and Line P stations in August-September 2019. Stations where either kinetic parameter could not be calculated are marked with NC (not calculated).

Station	Si ρ_{max}	Si K_m	ρ_{amb}:ρ_{max}	Response to enhancement
	μmol L^{-1} day^{-1}	μmol L^{-1}	%	
P26	0.38	16.04	34.5	Increase
P20	0.11*	NC	1.90*	Increase
P16	0.06	15.4	3.24	Increase
P12	0.06	15.5	5.81	No increase
P4	0.08*	NC	57.69*	Increase
LG09	0.62	2.33	8.60	Increase
LB15	0.95	18.3	2.26	Increase
CS02	0.64	2.34	102.63	No increase
LBP3	0.88	4.75	3.30	Increase
LC06	1.64*	NC	47.62*	Increase

* for stations where ρ_{max} could not be calculated from the MM function, ρ at the 20 μM enrichment was used for ρ_{max} (Krause et al., 2012).

3.3.6 Abundance and taxonomic composition of phytoplankton assemblage

Total phytoplankton abundance was highest at station LC06 at 4.9 x 10^6 cells L^{-1} and lowest at station P4 at 1.9 x 10^6 cells L^{-1} (Figure 3.10). On average, the off-shelf and on-shelf stations had higher contribution of diatoms and dinoflagellates than oceanic stations with LG09 having the highest number of diatoms per liter (Figure 3.10). Most Line P stations (P4-P20) had very low contribution of diatoms and were dominated by small coccoid cells (<5 μm). However, P26 was the only station with a higher numbers of diatoms (59% of the total assemblage), when compared to all other Line P stations, showing high contributions from both *Thalassiosira sp.* and *Nitzschia sp.*

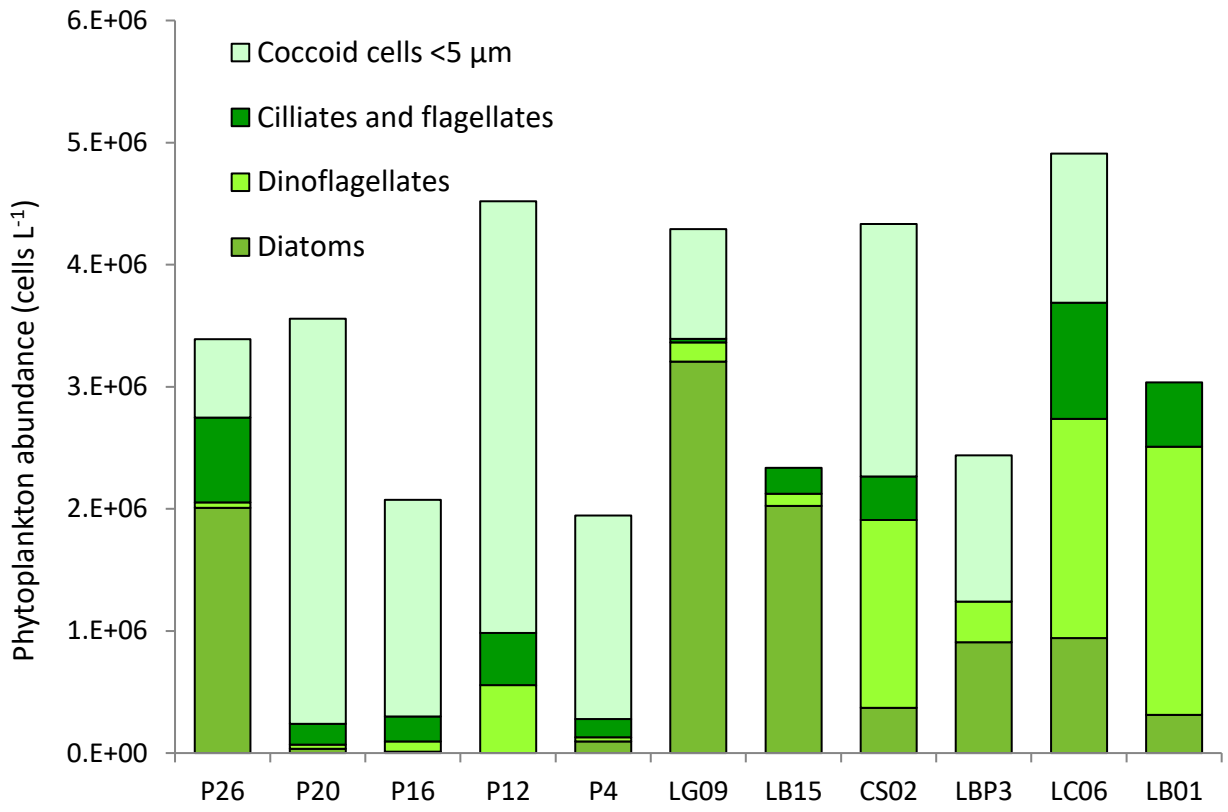

Figure 3.10. Abundance (cells L^{-1}) of major phytoplankton groups along Line P and La Perouse stations at 5 m during August-September 2019. On-shelf stations are LBP3, LC06, amd LB01, off-shelf stations are P4, P12, CS02, LG09, and LB15, oceanic stations are P16, P20, and P26.

Dinoflagellates were present in all samples with *Gyrodimium Protocentrum*, *Ceratium*, and *Alexandrium* as the most dominant genera. Dinoflagellates usually contributed between 0-15% of the total assemblage except at LB01, LC06, and CS02 where they made up 72%, 36%, and 35% of the total assemblage, respectively.Coccoid cells <5 µm, which may represent several taxa, were more numerous from P4-P20 where they contributed ~85-93% of the total assemblage. The contribution of ciliates and other flagellates was between 0-20% of the assemblage at all stations. The most common ciliate genus was the mixotrophic *Myrionecta*.

3.4 Discussion

3.4.1 Summary of results

In August-September 2019, temperatures in the mixed layer were high along Line P and the west coast of Vancouver Island compared to historical averages. The maximum temperature, ~18 °C, was recorded at P4 but temperatures were similarly high (17.5-18 °C) at surrounding stations LG09 and LB15 and these high temperatures extended offshore up to P16. For all stations, K_m values for NO_3^- were low (0.01-4.68 µmol L-1), suggesting affinity for NO_3^- was high. Additionally, ρ_{max} was not considerably different from ambient ρNO_3^- at most stations. In contrast, most stations did show an increase in uptake rates with enhancement of $Si(OH)_4$ and K_m values were substantially higher (2.33-18.3 µmol L-1) than those of NO_3^-. Phytoplankton assemblages along most of Line P were dominated by coccoid cells <5 µm, whereas La Perouse stations had a higher contribution from diatoms, ciliates and dinoflagellates. Notably, biological particulates and uptake at P26 was anomalously high compared to previous studies in the region. There was also a large contribution of diatoms and other cells >5 µm to the total chl-a and the phytoplankton abundance.

3.4.2 Temperature and nutrient distributions in the NE Pacific in summer 2019

During August-September 2019, the temperatures in the mixed layer along both Line P and La Perouse were above 12 °C at all stations. Temperature anomalies in the mixed layer at Line P stations were all positive and were up to 3°C at P4 compared to the 1981-2010 climatic averages at all stations (Crawford et al., 2007; Fisheries and Oceans Canada, 2019; see section 2.4). Temperatures were particularly high between P4 and P20 where they reached a maximum of 18 °C at P12. In addition to being warmer, water in the mixed layer at all stations along Line P was less saline, and less dense compared to the 1951-1991 averages (Fisheries and Oceans Canada, 2019; see section 2.4). These physical parameters all suggest that during late summer 2019, ocean waters were warm and stratified in regions of the NE Pacific Ocean, similar to conditions observed during other MHWs (see section 2.4). Seawater temperatures were similarly high over most of the La Perouse region. Mixed layer temperatures at all La Perouse stations, except LC06 and LB01, were between ~15-17 °C. Although these temperatures are not unprecedented on the west coast of Vancouver Island, these values are considered to be in the high end of the temperature range. Records from the British Columbia Shore Station Oceanographic Program monitoring on Vancouver Island (Iwabuchi & Gosselin, 2019) show that the maximum SST recorded between 1935 and 2016 on the west coast of Vancouver Island was 16.78 °C when averaged between the two observation stations on Amphirite Point (48°55.272´ N 125°32.468´ W) and Kains Island (50°26.559´ N 128°01.998´ W). These warm temperatures are typical of MHW conditions and are consistent with observations made during other NE Pacific warming events (Amaya et al., 2020; Di Lorenzo & Mantua, 2016; Ross et al., 2021). The overall increase in SST on the west coast of Vancouver Island (Iwabuchi & Gosselin,

2019) coupled with an increase in severity and frequency of MHW events (Oliver et al., 2019) could result in more frequent and higher extreme SSTs around Vancouver Island.

When ambient dissolved nutrient data is plotted for stations from summer 2019, there is an inverse correlation between measured SST and dissolved [$Si(OH)_4$] (R^2=0.85) and [PO_4] (R^2=0.81) in the mixed layer (Figure 3.11). This correlation was weakly observed with [NO_3] but was not significant (R^2=0.15).

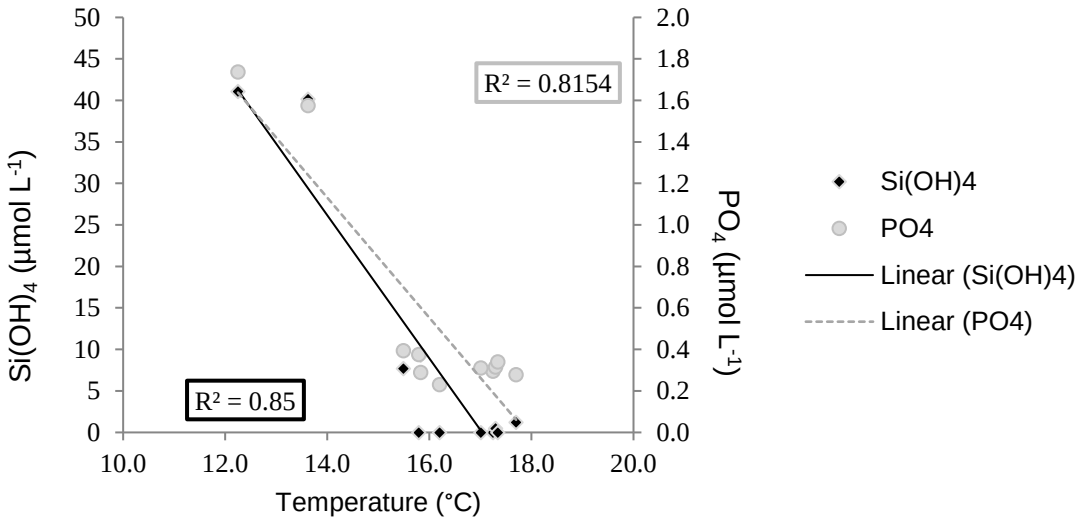

Figure 3.11. Correlation between measured seawater temperature (SST) and dissolved silicic acid ($Si(OH)_4$) and phosphate (PO_4) at major Line P and Le Perouse stations at 5 m in August-September 2019. Dashed grey line is linear regression of PO_4 data and solid line is linear regression of $Si(OH)_4$ data. R^2 value show correlation between nutrient concentration and temperature for $Si(OH)_4$ (black box) and PO_4 (grey box).

The stations that had the lowest temperatures, LC06 and LB01, also had the highest dissolved [$Si(OH)_4$] and [PO_4] of all stations. Similarly, stations with high temperatures had very low [$Si(OH)_4$] and [PO_4]. Stations with colder, nutrient rich water closer to the coast may have had a stronger signal of surface runoff while warmer, low nutrient waters had a signal more typically seen in subtropical oligotrophic oceans (Harris et al., 2009; Frank A. Whitney et al.,

2005). While there was a clear relationship between these two dissolved nutrients and temperature, it is unclear why NO_3 did not show the same relationship. It is well known that NO_3 concentrations have an inverse relationship to temperature in the world's oceans (Strickland, 1970; Suess & Thiede, 1983; Dugdale et. al, 1989) but in 2019 it appeared to be decoupled from SST. However, because the relationship between temperature and nutrients is mediated by biological consumption, changes in primary production can break down this relationship quite easily (Henson et al., 2003). Additionally, it has been previously observed that specifically during spring and summer, the linear relationship between NO_3 and T may not hold (Henson et al., 2003). Thus, during 2019, variations in this relationship may be due to decoupling of the T-NO_3, relationship.

In the summer of 2019, dissolved nutrient concentrations on the west coast of Vancouver island were similar to previous years but along Line P they were among the lowest on record (Boldt, 2020). This decrease in dissolved nutrients to anomalously low levels is a phenomenon that has been observed during warming events in the past (Freeland et al., 1997; Harris et al., 2009; Peña et al., 2019; Peña & Varela, 2007; Whitney et al., 1998) and has also been observed to result in a decrease in both new and total productivity (Harris et al., 2009). During the 2019 MHW, the kinetic experiments performed provided better insights into the extent of NO_3 and $Si(OH)_4$ limitation caused by this widespread, spatial decrease in nutrients.

3.4.3 Nitrate uptake kinetics in the NE Pacific during the 2019 MHW event

In the HNLC region of the NE subarctic Pacific, essential macronutrients like NO_3 are not typically thought to be limiting for phytoplankton growth (Cullen, 1991; Yasunaka et al., 2021). However, observations over the last twenty five years have suggested that dissolved nutrients such as NO_3, and $Si(OH)_4$ may be decreasing over time due to changes in winter mixing and heating of the surface ocean (Freeland et al., 1997; Whitney et al., 1998). This nutrient decrease may be exacerbated by an increase in the frequency of MHW events (Oliver et al., 2019; Xu et al., 2021). In 2015, the NE subarctic Pacific Ocean experienced the most intense MHW of the last 70 years, when stark decrease in dissolved nutrient concentrations and phytoplankton biomass were measured compared to established averages over much of the Line P transect (Peña et al., 2019). Additionally, there was an increase in abundance of pico-phytoplankton (0.2 -2 µm), which are efficient nutrient users and tend to outcompete other phytoplankton in oligotrophic waters (Agawin et al., 2000). Based on these observations, Peña et al. (2019) suggested that phytoplankton assemblages within the nutrient-low zone (~P4-P22) were nutrient-limited (probably by NO_3 or Fe). While it was evident that NO_3 was at anomalously low levels during August-September 2019, kinetic experiments conducted during this thesis revealed that only assemblages at CS02 responded to addition of NO_3. Although [NO_3] were below the LoD at many of the stations, addition of NO_3 to natural assemblages from these stations did not result in any increase in NO_3 uptake. At all stations except CS02, ρ_{amb}:ρ_{max} was well above the 25% threshold that would indicate physiological limitation. Furthermore, the K_m vales that were calculated from kinetic experiments were <0.1 µmol L^{-1} except at LC06. Thus, all evidence collected during the 2019 MHW points to the fact that assemblages were not limited by NO_3 alone.

It is well documented that most oceanic stations along Line P are characterized by higher levels of regenerated productivity, relying more heavily on reduced forms of N such as NH_4 and urea (Varela & Harrison, 1999; Peña & Varela, 2007; Meyer et al., 2022). This is in part due to the fact that the uptake of reduced N (such as NH_4) requires much less Fe than the uptake of NO_3 (Raven, 1988). Additionally, higher temperatures can also lead to more regenerated productivity due to the higher grazing and regeneration of N by zooplankton in warmer waters (Banse, 1995; Peña et al., in review). Many of the stations were characterized by a high abundance of small-celled phytoplankton (<5 µm) which usually dominate when Fe is limiting and preferentially use regenerated forms of N (Marchetti et al., 2006). It is likely that high affinity for NO_3 by any large cells that were present, coupled with the use of recycled N sources allowed assemblages that were observed in this study to grow without physiological N limitation. However, it is also likely that the decrease in total N, from low mixing, could ultimately result in lower annual biomass, even if physiological limitation does not occur (Falkowski et al., 1998).

Examining NO_3 K_m and ρ_{max} values more closely allows for a higher resolution look at nutrient uptake and physiology of assemblages in the study regions At all Line P stations, K_m was <0.01 µmol L^{-1} except P12 (K_m = 0.13 µmol L^{-1}). At all of these stations, the phytoplankton assemblage was dominated by small coccoid cells, which are efficient users of N (mostly recycled). At P12, where K_m was slightly higher, there was an increase in the amount of dinoflagellates, inefficient users of N, and it is possible that their contribution may be the reason that K_m values increased at P12. Among La Perouse stations, LC06 and CS02 had the highest K_m values for NO_3^- uptake of all the stations (4.68, and 0.83 µmol L^{-1} respectively). Both of these stations, similarly to P12, had a significant contribution from dinoflagellates to the total

assemblage. Increases in the abundance of dinoflagellates in an assemblage will likely shift the K_m of the assemblage higher.

The ρ_{max} for NO_3 had a variable distribution over the study region. Along Line P, ρ_{max} varied between ~0.1-0.3 μmol L^{-1} day^{-1} but was generally lower than the Le Perouse stations where ρ_{max} reached a maximum of 1.57 μmol L^{-1} day^{-1}. For all stations in summer 2019, ρ_{max} seemed to be mostly correlated to lower SST and higher biomass. Previous studies have shown that the affinity for NO_3 in mixed assemblages (particularly dominated by diatoms and dinoflagellates) decreases as a function of temperature and duration of a bloom (Fan et al., 2003; Lomas & Glibert, 2000). However, some research has also shown that certain diatoms and mixotrophic dinoflagellates increase their NO_3 uptake at higher temperatures (Berges et al., 2002; Coyne et al., 2021), likely due to the activity of NR. Therefore, while there may be some positive effects of temperature on NR activity, it is likely that the late summer bloom stage contributed to the overall lower observed kinetic efficiency of phytoplankton.

3.4.4 Silicon kinetics in the NE Pacific during the 2019 MHW event

During August-September 2019, there was a clear relationship between $[Si(OH)_4]$, ambient ρSi and the degree of Si limitation in the study region. Ambient ρSi was highest at stations where $[Si(OH)_4]$ were well above detectable concentrations. There was also more pronounced limitation (ie. ρ_{amb}:ρ_{max} was lower) at stations that already had high ambient ρSi. At stations P12, P16, P20, P26, LBP3, LB15, and LG09, there did appear to be some degree of limitation from $Si(OH)_4$. At all of these stations the ρ_{amb}:ρ_{max} was <25% and there was a measurable increase in ρSi even at low levels of enhancement or when there were measurable $[Si(OH)_4]$ in the mixed layer. Particularly at P20, the Si ρ_{max} (0.1 μmol L^{-1} day^{-1}) was more than an order of magnitude higher than the ambient rate (<0.01 μmol L^{-1} day^{-1}). At stations where K_m

could be calculated, the values were nearly always higher than those measured for NO_3. Silicon K_m ranged from 2.33 µmol L^{-1} at LG09 to as high as 18.3 µmol L^{-1} at LB15. These values are considerably higher than those observed where natural phytoplankton assemblages are growing in nutrient-replete waters (Nelson & Brzezinski, 1990; Nelson & Tréguer, 1992) and suggest that most assemblages in the NE Pacific had low $Si(OH)_4$ uptake efficiency.

The low efficiency of $Si(OH)_4$ uptake has implications for how severely future MHWs can affect phytoplankton assemblages. Since Si uptake can become limited even while $Si(OH)_4$ is present at detectable levels in the water column, the likelihood that physiological limitation will occur increases, especially during MHWs when nutrients are not being replenished. So, in these areas, further nutrient depletion that may be caused by MHW events will likely lead to physiological limitation of diatoms for $Si(OH)_4$ and a switch to smaller phytoplankton that do not require Si for growth.

It is well documented that diatoms growing under Fe limitation are more silicified and have a lower affinity for Si (Hutchins & Bruland, 1998; Mosseri et al., 2008; Takeda, 1998). There is also considerable evidence that both Si and Fe play a role in the limitation of diatom growth in many marine HNLC environments (Dugdale et al., 1995; Brzezinski et al., 2022; Hutchins et al., 2001; Mosseri et al., 2008; Rocha et al., 2000). In August-September 2019, diatom growth may have been co-limited by both Si and Fe over much of the Line P transect; a scenario that has already been described in the NE Pacific (Brzezinski et al., 2022). In these areas, Fe limitation would cause affinity for Si to decrease and would also lead to a higher cellular demand for Si (Brzezinski et al., 2022; Hutchins & Bruland, 1998b; Marchetti et al., 2006; Nelson et al., 2001). This increased demand and decreased affinity would mean that K_m would likely be higher than the ambient [$Si(OH)_4$], which would cause nutrient limitation. Thus,

severely low Fe (<0.1 nmol L^{-1}) would limit diatom growth in these areas, which would lead to limitation of overall $Si(OH)_4$ uptake. For the La Perouse stations, where Fe is less likely to be limiting, limitation from Si alone would likely lead to lower Si uptake rates for diatoms. However, for all stations whether Fe limited or not, the consequences of the MHW are similar; lower mixing and more stratified waters lead to lower inventories of $Si(OH)_4$ which could cause a decrease in large diatoms and proliferation of small-celled phytoplankton in the NE Pacific.

Kinetic experiments performed during this study indicated that there did not appear to be any correlation with SST and either ρ_{max} or K_m (Figure 3.12) but both parameters were much more closely correlated with ambient $Si(OH)_4$.

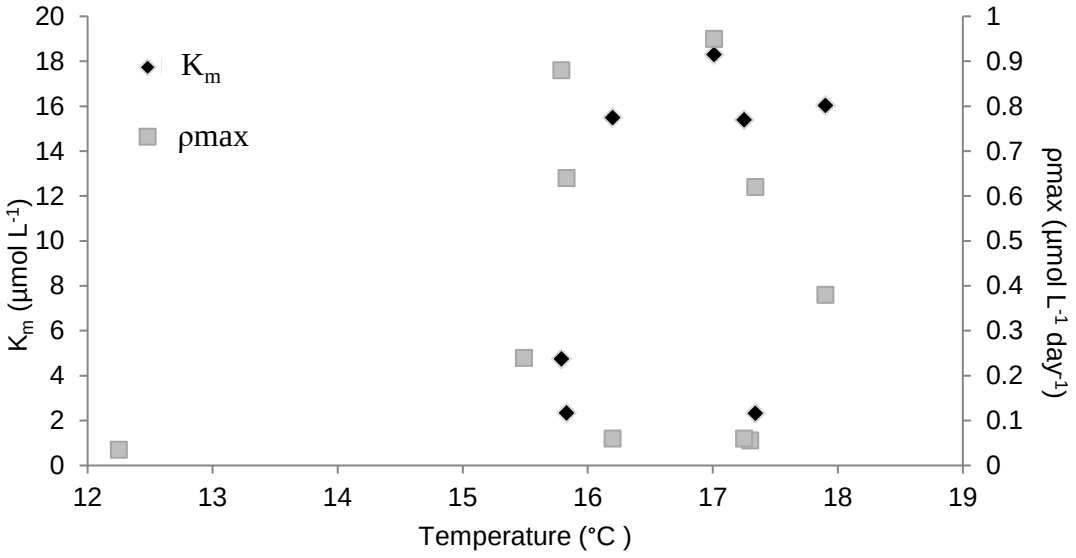

Figure 3.12. Silicon uptake kinetic parameters ρ_{max} and K_m plotted against seawater temperature (°C) at 5 m for all stations in 2019. For stations where ρ_{max} could not be calculated from the Michaelis-Menten model, the ρSi measured at the 20 µmol L^{-1} enrichment was used as ρ_{max}.

This indicates that rate and efficiency of $Si(OH)_4$ uptake are much more closely tied to substrate concentration than temperature in the NE Pacific. Although research is unclear as to if there is a

relationship between temperature and Si uptake (Blank et al.,1986; van Donk & Kilham, 1990; Stapleford & Smith, 1996), it is much more likely that in sub-polar regions where water temperatures are usually <20 °C, $Si(OH)_4$ uptake will be primarily limited by $Si(OH)_4$ concentrations.

3.4.5 Phytoplankton assemblages and biomass

In August-September 2019, the abundance and taxonomic composition of phytoplankton assemblage was spatially variable. Cell abundances were generally >2.5 $x10^6$ at the La Perouse shelf stations and were dominated by dinoflagellates, cilliates, and diatoms. Stations P4-P20 (Line P off-shelf and oceanic stations) were dominated by coccoid cells <5 µm and had very low diatom abundance. These coccoid cells are likely pico and nanoplanktonic Haptophytes, which are generally dominant in the offshore stations of Line P (Peña et al., 2019; Peña & Varela, 2007; Royer et al., 2010). However, there was an increase in diatom abundance at P26 that was also accompanied by an unusual increase in chl-a, PC, PN, and $bSiO_2$. These increases in diatoms and total phytoplankton biomass at P26 have been observed before, during previous MHW events (Peña et al., 2019) and also under Fe fertilization in HNLC regions (Marchetti et al., 2006). During the 2015 MHW event, natural Fe fertilization was not detected at P26 (Taves et al., 2022) and it was suggested that the increase in diatoms may have been influenced by the stability of the water column with a concomitant increase in light availability (Peña et al., 2019). Much like 2015, there was no evidence that natural Fe fertilization occured during summer 2019, and it is likely that diatoms were under Fe limitation (Taves et al., 2022; see section 3.4.4). However, as discussed above, limitation by both Fe and Si can co-occur in the NE Pacific. So, the relative increase of diatoms at P26 may have been the result of higher sustained levels of $Si(OH)_4$ in the mixed layer (7.7 µmol L^{-1}) at P26 relative to the other Line P stations.

The overall distribution of species and cell sizes of phytoplankton in 2019 is consistent with what has been traditionally observed in this region; higher contribution of small-celled phytoplankton to total abundance and biomass along most of Line P, and an increased contribution of larger (>10 μm) diatoms and dinoflagellates at the "on-shelf" stations. (Harris et al., 2009; Harrison et al., 2004; Meyer et al., 2022; Peña & Varela, 2007). However, P26 was unusually productive, having both higher chl-a and nutrient uptake rates than usually expected. In August, diatoms were abundant at P26, accounting for the higher Si uptake and chl-a than at other oceanic stations (Boldt, 2020).

3.5 Conclusions

High seawater temperatures and shallow mixed layers were characteristics of nearly all stations in the NE subarctic Pacific sampled in Aug-Sep 2019. Overall, there was higher mixed layer chl-a, $bSiO_2$, and both ρNO_3 and ρSi at the on-shelf and off-shelf La Perouse stations than at the Line P stations. Kinetic experiments indicated that while most assemblages had high efficiency for NO_3 uptake, the efficiency of $Si(OH)_4$ uptake was much lower. Additionally, enhancement with $Si(OH)_4$ at several stations was not saturated at the 20 μM. This low efficiency, and non-saturation at high levels of $Si(OH)_4$ indicate that while many of these assemblages have a high capacity for Si uptake, they may easily become Si limited during times when nutrient input to the surface waters is low. If MHW events lead to further decreases in deep-water injection and lateral mixing, then assemblages will likely shift towards smaller and non-Si dependent phytoplankton.

Chapter 4: General conclusions

4.1. Summary of results

Measured sea surface temperatures were higher and mixed layer depths were shallower at the majority of stations sampled in the NE Subarctic Pacific in 2019 compared to 2018. In 2019 there was also a considerable decrease in dissolved nutrients in the mixed layer when compared to 2018. Biomass was reduced at most stations or was concentrated at the subsurface chl-max depth instead of distributed through the mixed layer. Overall, NO_3 and C uptake did not seem to differ considerably between years, however the contribution from new and regenerated sources was different. Oceanic stations showed in increase in new productivity in 2019 while P4 had a higher contribution from regenerated sources compared to 2018.

In 2019, P26 was the most anomalous station and was uncharacteristically productive. Compared to the off-shelf station P4, P26 had higher chl-a, higher $bSiO_2$, and higher Si, C and NO_3 uptake rates. Additionally, there was a high contribution from cells >5 µm to chl-a and large diatoms were abundant. P26 also had a higher contribution from new productivity (f-ratio = 0.9) than is normally measured at this station, even with potential overestimates (up to 40%).

Kinetic experiments showed very efficient uptake of NO_3 at most stations (low K_m) but much less efficient uptake of $Si(OH)_4$ (high K_m). Likely, both $Si(OH)_4$ and NO_3 are limiting to some extent, with the former becoming limiting at much higher concnetrations. There is also a strong likelihood that assemblages are using more regenerated forms of N such as ammonium and urea; possibly due to increases in regenerated N sources from zooplankton activity (ie. waste excretion in the euphotic zone).

Overall, there were several unexpected characteristics of primary productivity in 2019 that may be linked to the MHW conditions. An increase in regenerated productivity, changes in the dominant cell size of the community, and the overall biomass changes are all characteristics that have been linked to warming ocean, both globally and locally (Laffoley & Baxter, 2016; Peña et al., 2019; Peña pers. comm.). Along the BC continental margin, results from this study indicate that there is likely to be a reduction in new productivity, increased limitation from $Si(OH)_4$ and changes in the size structure of assemblages. However, even within the study area, these changes seem to be very heterogeneous and may only be very localized. For example, while P4 was observed to have a higher contribution of regenerated productivity, a decrease in biomass, and a decrease in large cells, the opposite was observed at P26. This highlights the importance of high resolution studies and models when predicting productivity changes in future warmer oceans.

4.2 MHW effects in the NE Pacific in 2019

It is well established the MHWs will likely increase in their frequency and severity as climate change progresses, but their effects on global primary production are not well established (Barkhordarian et al., 2022; Oliver et al., 2019; Ross et al., 2021; Xu et al., 2021). In this study, I examined the ecophysiology of primary producers in the subarctic NE Pacific during the 2019 MHW. I found that while the 2019 MHW did not appear to cause large shifts in the ecological paradigms at most stations (e.g. there was limitation by the same nutrients as previously observed, there were similar phytoplankton groups present, water column properties were within the range previously observed), the establishment of MHW conditions led to an intensification of the already well-established ecological processes. In late summer of 2019, there was an overall increase in mixed-layer temperatures, a much more stratified ocean, and a shoaling of the mixed

layer compared to observations from 2018 and to historical records for the region (Crawford et al., 2007; Government of Canada, 2009; Iwabuchi & Gosselin, 2019). Globally, MHW events are well known to cause these kind of physical and chemical changes in marine systems, usually as the result of changes to atmospheric patterns that lead to decreased wind, heat loss from the surface ocean, and mixing (Amaya et al., 2020; Barkhordarian et al., 2022; Di Lorenzo & Mantua, 2016; Xu et al., 2021). These effects were accompanied by anomalously low [NO_3] and [$Si(OH)_4$] in the mixed layer along Line P.

If we examine the magnitude of $Si(OH)_4$ depletion at P26, there is a clear indication that the magnitude of depletion in 2019 was larger than average. In the winter of 2018-2019, $Si(OH)_4$ was ~20 µM in the mixed layer (Government of Canada, 2009) and decreased to ~8 µM by late August. This implies a $Si(OH)_4$ depletion of about 12 µM which is nearly double the average for this region (Brzezinski et al., 2022; Peña & Varela, 2007). This increase in the magnitude of $Si(OH)_4$ depletion could be the result of increased biological uptake as well as a decrease in vertical nutrient injection. The magnitude of NO_3 depletion at P26 was similar to that of $Si(OH)_4$ (~13 µM) and was also nearly double the depletion that was observed at P26 in the previous year (~7 µM) (Government of Canada, 2009). This increased drawdown may have been the result of two factors; decreased input throughout the growing season from mixing and increased biological uptake. It is possible that significant nutrient uptake of both $Si(OH)_4$ and NO_3 started earlier in the season due to increased temperatures. Increased temperatures earlier in the season may result in increased enzyme efficiency and maximum growth rate for many phytoplankton (Cross et al., 2015; Rose & Caron, 2007). Specifically, increased activity of NR and RuBisCO can stimulate blooms to start earlier in the season (Trombetta et al., 2019), which could deplete nutrients in the mixed layer much more quickly and severely than during “typical” blooms.

While $Si(OH)_4$ and Fe are well established controls of primary productivity in the oceanic NE Pacific (Brzezinski et al., 2022; Roche et al., 1996), NO_3 has not traditionally been limiting in this HNLC region. The limitation by $Si(OH)_4$ was evident in the kinetic experiments; $Si(OH)_4$ uptake rates were limited by [$Si(OH)_4$] at the majority of stations, both shelf and oceanic. Additionally, the higher than average $Si(OH)_4$ depletion may indicate that Fe limitation led to higher $Si(OH)_4$ consumption (see section 1.2). While NO_3 limitation did not appear to be extreme (i.e. uptake rates were not strongly affected by enhancement), the lower total inventory of N in the euphotic zone will ultimately mean that the total potential biomass will be lower (Falkowski et al., 1992). Therefore, phytoplankton communities in the NE Pacific in late summer of 2019 may have been subject to combined Fe, Si, and NO_3 limitation during the MHW. While most nutrients become limiting when mixing decreases, Fe is supplied to the NE Pacific by several other mechanisms. While Fe input from Asian-derived aerosols is the main supply of bioavailable Fe (Boyd et al., 1998), there is also evidence that Fe supply from continental margins via eddies is significant to some areas in the NE Pacific Ocean (Lam et al., 2006). The atmospheric characteristics that usually precede and accompany MWHs are similar to those of ENSO which have been shown to influence global dust cycles (Le & Bae, 2022). Because MHWs are usually accompanied by both decreases in mixing and in wind activity, investigating how Fe supply may change during these events is important for understanding effects on primary production. Changes in the input of Fe, the relative proportion of trace metals, and possible increases in the degree of Fe limitation in the future may significantly alter the nutrient cycles in the NE Pacific.

The proportion of new and recycled productivity observed along Line P was similar between 2018 and 2019 at all stations except P4 and P26. At P4, there appeared to be a large

shift towards favoring recycled forms of N while at P26 the opposite trend occurred and an anomalously high contribution of new productivity was observed. It is unclear what may have caused this shift and this warrants further investigation. Increases in [NH_4] are known to inhibit NO_3 uptake (Dortch, 1990; Varela & Harrison, 1999), so it is possible that at P4, higher levels of recycled N than usual in the mixed layer caused a shift away from NO_3-derived production. This increase in recycled N sources could have been the result of increased zooplankton growth and grazing, which are known to increase under higher temperatures (Sommer & Lewendowska, 2011; Lewandowska et al., 2014). At P26, it is less clear why new productivity would have increased during warmer months. Usually, under Fe limitation, recycled forms of N are more favorable so an increase in NO_3-derived production is unexpected. Changes in the *f*-ratio have consequences for C export as new productivity (from NO_3) is usually associated with increased C export from the system. Further investigation should explore both NH_4 and urea uptake during MHWs to determine potential changes in the relative importance of various N species during these events. Additionally, changes in the relationship between primary and secondary production will be important for understanding changes in the potential C export by the planktonic community.

4.3 Areas of future research and unanswered questions

While investigations of biomass, uptake rates, temperature and nutrient distributions during the 2019 MHW event have given us greater insights into phytoplankton dynamics, there are many questions left unanswered. Particularly, there are two potential changes that will have the greatest impact on the function and stability of marine systems in the NE Pacific. Firstly, it is important to address whether phytoplankton blooms begin earlier during MHW events and whether maximum biomass and rates of productivity occur earlier in the season. If the growing

season begins earlier during MHW events, it is likely that secondary production will be effected in some way. Decoupling of phytoplankton, zooplankton, and fish maximum growth rates can have devastating effects on the populations of zooplankton and fish. Moreover, because primary producers are controlled to some extent by microzooplankton grazing (Frost, 1991; Landry et al., 1993; Makareviciute-Fichtner et al., 2021), changes in grazing could also lead to differences in assemblage succession, biomass and stoichiometry of phytoplankton. This could then lead to changes in the biological C pump, recycling of nutrients in the mixed layer, and even to higher frequency of harmful algal blooms. Physiological processes of zooplankton are sensitive to changes in ocean temperature (Richardson, 2008) and MHW conditions seem to favour an increase in gelatinous zooplankton such as Pyrosomes and doliolids (Ratnarajah et al., 2023; O' Loughlin et al., 2020; Brodeur et al., 2019). While increasing temperatures have been observed to lead to a decrease in zooplankton body size (hence negative effects on community export) gelatinous zooplankton can be more efficient grazers on a wider size range of phytoplankton (Pauli eta al., 2021) and an increase in these groups may actually increase export efficiency via fecal pellets (Ratnajarah et al., 2023). Investigating this question will be crucial for understanding future dynamics between phytoplankton and zooplankton.

The second question that should be answered is whether the total biomass of primary producers during a MHW event is less than that of a typical year. For this question, total annual inventories of dissolved N, Si, and Fe should be investigated along with the annual biomass. Similarly to changes in timing, changes in total biomass can have deleterious effects on both the secondary production and the export of C from surface oceans. While the biomass at any given time may be lower for primary producers (Bar-On & Milo, 2019) than for secondary producers, the total primary production over the growing season will ultimately be higher. Calculating the

total gross and net production, by incorporating more frequent measurements of primary productivity, will be integral to understanding changes in ocean ecosystems. Furthermore, if there are changes in the dominant size class of phytoplankton, there may be shifts in the trophic regimes and the efficiency of C export in the NE Pacific which result in a system with lower net primary production (Sarmiento et al., 2004; Chust et al., 2014).

While this study conducted kinetics experiments of nutrient uptake by phytoplankton assemblages during the late summer of 2019, during a MHW, a more thorough investigation, during winter, spring, and earlier summer will yield a more complete view on nutrient limitation and the efficiency of nutrient uptake for the region. Specifically, an incorporation of NH_4 and urea into kinetic experiments will provide insight into whether other forms of N are important in these systems, and if there is a shift in the relative contribution from each N source during MHWs. This will provide a better understanding of how assemblages may be responding to changes in temperature and whether a greater stratification of the water column coupled with more zooplankton activity is leading to an increase in recycled N use in surface waters in these systems.

MHW events are known to be increasing in both severity and frequency globally and as the oceans warm, they will likely become a more common part of future oceanographic systems (Barkhordarian et al., 2022; Cheung & Frölicher, 2020; Oliver et al., 2019; Shanks et al., 2020; Xu et al., 2021). Additionally, observations that are made during current MHWs could give us insight into how biological and chemical cycles might be affected under the warmer ocean conditions projected for both climate scenarios ICPP 4.5 and ICPP 8.5. This warrants special consideration on how both primary producers and the trophic levels they support will be affected during these events. Considering the heterogeneous nature of ocean systems and the diversity of

primary and secondary producers, there is a need for much higher resolution observation and monitoring. In particular, the development of novel methods to measure primary productivity, such as single turnover active fluorometry (STAF) and the fast repetition rate fluorometry (FRRf) will be valuable tools for future monitoring programs, particularly when used alongside methods to measure secondary production. Large-scale studies that incorporate repeated measurements of kinetic parameters, nutrient inventories, biomass, and phytoplankton and zooplankton production should prove extremely useful in determining how and why primary producers may be impacted by severe oceanic warming in the future, and will help improve ocean and climate models.

Bibliography

Agawin, N. S. R., Duarte, C. M., & Agustí, S. (2000). Nutrient and temperature control of the contribution of picoplankton to phytoplankton biomass and production. *Limnology and Oceanography*, *45*(3), 591–600. https://doi.org/10.4319/lo.2000.45.3.0591

Allen, J. T., Brown, L., Sanders, R., Mark Moore, C., Mustard, A., Fielding, S., et al. (2005). Diatom carbon export enhanced by silicate upwelling in the northeast Atlantic. *Nature*, *437*(7059), 728–732. https://doi.org/10.1038/nature03948

Amaya, D. J., Miller, A. J., Xie, S.-P., & Kosaka, Y. (2020). Physical drivers of the summer 2019 North Pacific marine heatwave. *Nature Communications*, *11*(1), 1903. https://doi.org/10.1038/s41467-020-15820-w

Baeyens, W., Gao, Y., Davison, W., Galceran, J., Leermakers, M., Puy, J., et al. (2018). In situ measurements of micronutrient dynamics in open seawater show that complex dissociation rates may limit diatom growth. *Scientific Reports*, *8*(1), 16125. https://doi.org/10.1038/s41598-018-34465-w

Baines S.B., Twining B. S., Brzezinski M. A., Nelson D. M., & Fisher N. S. (2010). Causes and biogeochemical implications of regional differences in silicification of marine diatoms. *Global Biogeochemical Cycles*, *24*(4). https://doi.org/10.1029/2010GB003856

Banse, K., 1995. Zooplankton: pivotal role in the control of ocean production: I. Biomass and production. *ICES Journal of marine Science*, *52*(3-4), pp.265-277.

Bar-On, Y.M. and Milo, R., 2019. The biomass composition of the oceans: a blueprint of our blue planet. *Cell*, *179*(7), pp.1451-1454.

Barkhordarian, A., Nielsen, D. M., & Baehr, J. (2022). Recent marine heatwaves in the North Pacific warming pool can be attributed to rising atmospheric levels of greenhouse gases.

Communications Earth & Environment, *3*(1), 1–12. https://doi.org/10.1038/s43247-022-00461-2

Barwell-Clarke, J., & Whitney, F. A. (1996). *Institute of Ocean Sciences nutrient methods and analysis*. Fisheries and Oceans Canada.

Batten, S. D., & Crawford, W. R. (2005). The influence of coastal origin eddies on oceanic plankton distributions in the eastern Gulf of Alaska. *Deep Sea Research Part II: Topical Studies in Oceanography*, *52*(7), 991–1009. https://doi.org/10.1016/j.dsr2.2005.02.009

Beevers, L., & Hageman, R. H. (1969). Nitrate Reduction in Higher Plants. *Annual Review of Plant Physiology*, *20*(1), 495–522. https://doi.org/10.1146/annurev.pp.20.060169.002431

Behrenfeld, M. J., O'Malley, R. T., Siegel, D. A., McClain, C. R., Sarmiento, J. L., Feldman, G. C., et al. (2006). Climate-driven trends in contemporary ocean productivity. *Nature*, *444*(7120), 752–755. https://doi.org/10.1038/nature05317

Benthuysen, J., Feng, M., & Zhong, L. (2014). Spatial patterns of warming off Western Australia during the 2011 Ningaloo Niño: Quantifying impacts of remote and local forcing. *Continental Shelf Research*, *91*, 232–246. https://doi.org/10.1016/j.csr.2014.09.014

Berges, J. A., Varela, D. E., & Harrison, P. J. (2002). Effects of temperature on growth rate, cell composition and nitrogen metabolism in the marine diatom Thalassiosira pseudonana (Bacillariophyceae). *Marine Ecology Progress Series*, *225*, 139–146. https://doi.org/10.3354/meps225139

Bishop, J. K. B., Davis, R. E., & Sherman, J. T. (2002). Robotic Observations of Dust Storm Enhancement of Carbon Biomass in the North Pacific. *Science*, *298*(5594), 817–821. https://doi.org/10.1126/science.1074961

Blank, G. S., Robinson, D. H., & Sullivan, C. W. (1986). Diatom Mineralization of Silicic Acid. Viii. Metabolic Requirements and the Timing of Protein Synthesis1. *Journal of Phycology*, *22*(3), 382–389. https://doi.org/10.1111/j.1529-8817.1986.tb00039.x

Bock, N., Subramaniam, A., Juhl, A. R., Montoya, J., & Duhamel, S. (2022). Quantifying Per-Cell Chlorophyll a in Natural Picophytoplankton Populations Using Fluorescence-Activated Cell Sorting. *Frontiers in Marine Science*, *9*. Retrieved from https://www.frontiersin.org/articles/10.3389/fmars.2022.850646

Boldt, J. L. (2020). *State of the physical, biological and selected fishery resources of Pacific Canadian marine ecosystems in 2019*. P. C. Chandler, & S. A. King (Eds.). Fisheries and Oceans Canada- Pêches et Océans Canada.

Bonachela, J. A., Klausmeier, C. A., Edwards, K. F., Litchman, E., & Levin, S. A. (2016). The role of phytoplankton diversity in the emergent oceanic stoichiometry. *Journal of Plankton Research*, *38*(4), 1021–1035. https://doi.org/10.1093/plankt/fbv087

Bond, N. A., Cronin, M. F., Freeland, H., & Mantua, N. (2015). Causes and impacts of the 2014 warm anomaly in the NE Pacific. *Geophysical Research Letters*, *42*(9), 3414–3420. https://doi.org/10.1002/2015GL063306

Boyd, P., Muggli, D., Varela, D., Goldblatt, R., Chretien, R., Orians, K., & Harrison, P. (1996). In vitro iron enrichment experiments in the NE subarctic Pacific. *Marine Ecology Progress Series*, *136*, 179–193. https://doi.org/10.3354/meps136179

Boyd, P. W., Wong, C. S., Merrill, J., Whitney, F., Snow, J., Harrison, P. J., & Gower, J. (1998). Atmospheric iron supply and enhanced vertical carbon flux in the NE subarctic Pacific: Is there a connection? *Global Biogeochemical Cycles*, *12*(3), 429–441. https://doi.org/10.1029/98GB00745

Bristow, L. A., Mohr, W., Ahmerkamp, S., & Kuypers, M. M. M. (2017). Nutrients that limit growth in the ocean. *Current Biology*, *27*(11), R474–R478. https://doi.org/10.1016/j.cub.2017.03.030

Brodeur, R. D., Auth, T. D. & Phillips, A. J. (2019) Major shifts in pelagic micronekton and macrozooplankton community structure in an upwelling ecosystem related to an unprecedented marine heatwave. *Frontiers in Maine Science* https://doi.org/10.3389/fmars.2019.00212

Brown, M. T., Lippiatt, S. M., Lohan, M. C., & Bruland, K. W. (2012). Trace metal distributions within a Sitka eddy in the northern Gulf of Alaska. *Limnology and Oceanography*, *57*(2), 503–518. https://doi.org/10.4319/lo.2012.57.2.0503

Brzezinski, M., Villareal, T., & Lipschultz, F. (1998). Silica production and the contribution of diatoms to new and primary production in the central North Pacific. *Marine Ecology Progress Series*, *167*, 89–104. https://doi.org/10.3354/meps167089

Brzezinski, M. A., & Nelson, D. M. (1986). A solvent extraction method for the colorimetric determination of nanomolar concentrations of silicic acid in seawater. *Marine Chemistry*, *19*(2), 139–151. https://doi.org/10.1016/0304-4203(86)90045-9

Brzezinski, M. A., & Nelson, D. M. (1989). Seasonal changes in the silicon cycle within a Gulf Stream warm-core ring. *Deep Sea Research Part A. Oceanographic Research Papers*, *36*(7), 1009–1030. https://doi.org/10.1016/0198-0149(89)90075-7

Brzezinski, M. A., & Nelson, D. M. (1995). The annual silica cycle in the Sargasso Sea near Bermuda. *Deep Sea Research Part I: Oceanographic Research Papers*, *42*(7), 1215–1237. https://doi.org/10.1016/0967-0637(95)93592-3

Brzezinski, M. A., & Phillips, D. R. (1997). Evaluation of 32Si as a Tracer for Measuring Silica Production Rates in Marine Waters. *Limnology and Oceanography*, *42*(5), 856–865.

Brzezinski, M. A., Varela, D. E., Jenkins, B. D., Buck, K. N., Kafrissen, S. M., & Jones, J. L. (2022). The upper ocean silicon cycle of the subarctic Pacific during the EXPORTS field campaign. *Elementa: Science of the Anthropocene*, *10*(1), 00087. https://doi.org/10.1525/elementa.2021.00087

Button, D. K. (1983). Differences between the kinetics of nutrient uptake by micro-organisms, growth and enzyme kinetics. *Trends in Biochemical Sciences*, *8*(4), 121–124. https://doi.org/10.1016/0968-0004(83)90232-3

Carpenter, E. J., Remsen, C. C., & Watson, S. W. (1972). Utilization of Urea by Some Marine Phytoplankters1. *Limnology and Oceanography*, *17*(2), 265–269. https://doi.org/10.4319/lo.1972.17.2.0265

Chen, K., Zhou, M., Zhong, Y., Waniek, J. J., Shan, C., & Zhang, Z. (2022). Effects of Mixing and Stratification on the Vertical Distribution and Size Spectrum of Zooplankton on the Shelf and Slope of the Northern South China Sea. *Frontiers in Marine Science*, *9*. Retrieved from https://www.frontiersin.org/articles/10.3389/fmars.2022.870021

Chen, Z., Shi, J., Liu, Q., Chen, H., & Li, C. (2021). A Persistent and Intense Marine Heatwave in the Northeast Pacific During 2019–2020. *Geophysical Research Letters*, *48*(13), e2021GL093239. https://doi.org/10.1029/2021GL093239

Cheung, W. W. L., & Frölicher, T. L. (2020). Marine heatwaves exacerbate climate change impacts for fisheries in the northeast Pacific. *Scientific Reports*, *10*(1), 6678. https://doi.org/10.1038/s41598-020-63650-z

Chust, G., Allen, J.I., Bopp, L., Schrum, C., Holt, J., Tsiaras, K., Zavatarelli, M., Chifflet, M., Cannaby, H., Dadou, I. and Daewel, U., 2014. Biomass changes and trophic amplification of plankton in a warmer ocean. *Global Change Biology*, *20*(7), pp.2124 2139.

Climate Change 2001: The Scientific Basis: Contribution of Working Group I - Google Books. (n.d.). Retrieved November 23, 2022.

Coyne, K. J., Salvitti, L. R., Mangum, A. M., Ozbay, G., Main, C. R., Kouhanestani, Z. M., & Warner, M. E. (2021). Interactive effects of light, CO2 and temperature on growth and resource partitioning by the mixotrophic dinoflagellate, Karlodinium veneficum. *PLOS ONE*, *16*(10), e0259161. https://doi.org/10.1371/journal.pone.0259161

Crawford, W., Galbraith, J., & Bolingbroke, N. (2007). Line P ocean temperature and salinity, 1956–2005. *Progress in Oceanography*, *75*(2), 161–178. https://doi.org/10.1016/j.pocean.2007.08.017

Crawford, W. R., & Thomson, R. E. (1991a). Physical oceanography of the western Canadian continental shelf. *Continental Shelf Research*, *11*(8), 669–683. https://doi.org/10.1016/0278-4343(91)90073-F

Crawford, W. R., & Thomson, R. E. (1991b). Physical oceanography of the western Canadian continental shelf. *Continental Shelf Research*, *11*(8), 669–683. https://doi.org/10.1016/0278-4343(91)90073-F

Cross, W. F., Hood, J. M., Benstead, J. P., Huryn, A. D., & Nelson, D. (2015). Interactions between temperature and nutrients across levels of ecological organization. *Global Change Biology*, *21*(3), 1025–1040. https://doi.org/10.1111/gcb.12809

Taves, R.C., Janssen, J.D., Peña, A.M., Ross, A., Simpson, K., Crawford, W., & Cullen, J.T. (2022). Relationship between surface dissolved iron inventories and net community production during a marine heatwave in the subarctic northeast Pacific. *Environmental Science: Processes & Impacts*, *24*(9), 1460–1473. https://doi.org/10.1039/D2EM00021K

Cullen, J. J. (1991). Hypotheses to explain high-nutrient conditions in the open sea. *Limnology and Oceanography*, *36*(8), 1578–1599. https://doi.org/10.4319/lo.1991.36.8.1578

Cullen, J. T., Chong, M., & Ianson, D. (2009). British Columbian continental shelf as a source of dissolved iron to the subarctic northeast Pacific Ocean. *Global Biogeochemical Cycles*, *23*(4). https://doi.org/10.1029/2008GB003326

Cushing, D. H. (1990). Plankton Production and Year-class Strength in Fish Populations: an Update of the Match/Mismatch Hypothesis. In J. H. S. Blaxter & A. J. Southward (Eds.), *Advances in Marine Biology* (Vol. 26, pp. 249–293). Academic Press. https://doi.org/10.1016/S0065-2881(08)60202-3

Dagenais-Bellefeuille, S., & Morse, D. (2013). Putting the N in dinoflagellates. *Frontiers in Microbiology*, *4*, 369. https://doi.org/10.3389/fmicb.2013.00369

D'Alelio, D., Libralato, S., Wyatt, T., & Ribera d'Alcalà, M. (2016). Ecological-network models link diversity, structure and function in the plankton food-web. *Scientific Reports*, *6*, 21806.

De La Rocha, C.L., Hutchins, D.A., Brzezinski, M.A., & Zhang, Y. 2000. Effects of iron and zinc deficiency on elemental composition and silica production by diatoms. *Marine Ecology Progress Series*, *195*, 71-79.

Di Lorenzo, E., & Mantua, N. (2016). Multi-year persistence of the 2014/15 North Pacific marine heatwave. *Nature Climate Change*, *6*(11), 1042–1047. https://doi.org/10.1038/nclimate3082

van Donk, E., & Kilham, S. S. (1990). Temperature Effects on Silicon- and Phosphorus-Limited Growth and Competitive Interactions Among Three Diatoms1. *Journal of Phycology*, *26*(1), 40–50. https://doi.org/10.1111/j.0022-3646.1990.00040.x

Dortch, Q. (1990). The interaction between ammonium and nitrate uptake in phytoplankton. *Marine Ecology Progress Series*, *61*, 183–201. https://doi.org/10.3354/meps061183

Ducklow, H., Steinberg, D., & Buesseler, K. (2001). Upper Ocean Carbon Export and the Biological Pump. *Oceanography*, *14*(4), 50–58. https://doi.org/10.5670/oceanog.2001.06

Dugdale, R. C., & Wilkerson, F. P. (1986). The use of 15N to measure nitrogen uptake in eutrophic oceans; experimental considerations1,2. *Limnology and Oceanography*, *31*(4), 673–689. https://doi.org/10.4319/lo.1986.31.4.0673

Dugdale, R.C., Morel, A., Bricaud, A., & Wilkerson, F.P. 1989. Modeling new production in upwelling centers: a case study of modeling new production from remotely sensed temperature and color. *Journal of Geophysical Research -Oceans*, *94* (C12): 18 119-18 132.

Dugdale, R.C., & Wilkerson, F. P. (1998). Silicate regulation of new production in the equatorial Pacific upwelling. *Nature*, *391*(6664), 270–273. https://doi.org/10.1038/34630

Dugdale, R.C., Wilkerson, F. P., & Minas, H. J. (1995). The role of a silicate pump in driving new production. *Deep Sea Research Part I: Oceanographic Research Papers*, *42*(5), 697–719. https://doi.org/10.1016/0967-0637(95)00015-X

Durant, J. M., Molinero, J.-C., Ottersen, G., Reygondeau, G., Stige, L. C., & Langangen, Ø. (2019). Contrasting effects of rising temperatures on trophic interactions in marine ecosystems. *Scientific Reports*, *9*(1), 15213. https://doi.org/10.1038/s41598-019-51607-w

Edwards, K. F., Litchman, E., & Klausmeier, C. A. (2013). Functional traits explain phytoplankton community structure and seasonal dynamics in a marine ecosystem. *Ecology Letters*, *16*(1), 56–63. https://doi.org/10.1111/ele.12012

Eppley, R. W., & Peterson, B. J. (1979). Particulate organic matter flux and planktonic new production in the deep ocean. *Nature*, *282*(5740), 677–680. https://doi.org/10.1038/282677a0

Falkowski, P. G. (1994). The role of phytoplankton photosynthesis in global biogeochemical cycles. *Photosynthesis Research*, *39*(3), 235–258. https://doi.org/10.1007/BF00014586

Falkowski, P. G., Greene, R. M., & Geider, R. J. (1992). Physiological Limitations on Phytoplankton Productivity in the Ocean. *Oceanography*, *5*(2), 84–91.

Falkowski, P. G., Barber, R. T., & Smetacek, V. (1998). Biogeochemical Controls and Feedbacks on Ocean Primary Production. *Science*, *281*(5374), 200–206. https://doi.org/10.1126/science.281.5374.200

Falkowski, P. G., Laws, E. A., Barber, R. T., & Murray, J. W. (2003). Phytoplankton and Their Role in Primary, New, and Export Production. In *Ocean Biogeochemistry* (pp. 99–121). Springer, Berlin, Heidelberg. https://doi.org/10.1007/978-3-642-55844-3_5

Fan, C., Glibert, P. M., & Burkholder, J. M. (2003). Characterization of the affinity for nitrogen, uptake kinetics, and environmental relationships for Prorocentrum minimum in natural blooms and laboratory cultures. *Harmful Algae*, *2*(4), 283–299. https://doi.org/10.1016/S1568-9883(03)00047-7

Field, C. B., Behrenfeld, M. J., Randerson, J. T., & Falkowski, P. (1998). Primary Production of the Biosphere: Integrating Terrestrial and Oceanic Components. *Science, 281*(5374), 237–240. https://doi.org/10.1126/science.281.5374.237

Fiksen, Ø., Follows, M. J., & Aksnes, D. L. (2013). Trait-based models of nutrient uptake in microbes extend the Michaelis-Menten framework. *Limnology and Oceanography, 58*(1), 193–202. https://doi.org/10.4319/lo.2013.58.1.0193

Finkel, Z. V., Beardall, J., Flynn, K. J., Quigg, A., Rees, T. A. V., & Raven, J. A. (2010). Phytoplankton in a changing world: cell size and elemental stoichiometry. *Journal of Plankton Research*, *32*(1), 119–137. https://doi.org/10.1093/plankt/fbp098

Fisher, N. S., & Cowdell, R. A. (1982). Growth of marine planktonic diatoms on inorganic and organic nitrogen. *Marine Biology*, *72*(2), 147–155. https://doi.org/10.1007/BF00396915

Franco, A., Ianson, D., Ross, T., Hamme, R.C., Honahan, A.H., Christian, J.R., Davelaar, M., Johnson, W.K., Miller, L.A., Robert, M., and Tortell, P.D. (2022) Anthropogenic climatic contributions to observed carbon system trends in the Northeast Pacific. *Global Biogeochemical Cycles*, 35(7). e2020GB006829

Freeland, H. (2007). A short history of Ocean Station Papa and Line P. *Progress in Oceanography*, *75*(2), 120–125. https://doi.org/10.1016/j.pocean.2007.08.005

Freeland, H., Denman, K., Wong, C. S., Whitney, F., & Jacques, R. (1997). Evidence of change in the winter mixed layer in the Northeast Pacific Ocean. *Deep Sea Research Part I: Oceanographic Research Papers*, *44*(12), 2117–2129. https://doi.org/10.1016/S0967-0637(97)00083-6

Freeland, H. J., Crawford, W. R., & Thomson, R. E. (1984). Currents along the pacific coast of Canada. *Atmosphere-Ocean*, *22*(2), 151–172. https://doi.org/10.1080/07055900.1984.9649191

Frost, B. W. (1991). The role of grazing in nutrient-rich areas of the open sea. *Limnology and Oceanography*, *36*(8), 1616–1630. https://doi.org/10.4319/lo.1991.36.8.1616

Gao, Y., Smith, G. J., & Alberte, R. S. (2000). Temperature dependence of nitrate reductase activity in marine phytoplankton: biochemical analysis and ecological implications. *Journal of Phycology*, *36*(2), 304–313. https://doi.org/10.1046/j.1529-8817.2000.99195.x

Gargett, A. E. (1991). Physical processes and the maintenance of nutrient-rich euphotic zones. *Limnology and Oceanography*, *36*(8), 1527–1545. https://doi.org/10.4319/lo.1991.36.8.1527

Garrabou, J., Coma, R., Bensoussan, N., Bally, M., Chevaldonné, P., Cigliano, M., et al. (2009). Mass mortality in Northwestern Mediterranean rocky benthic communities: effects of the 2003 heat wave. *Global Change Biology*, *15*(5), 1090–1103. https://doi.org/10.1111/j.1365-2486.2008.01823.x

Government of Canada, F. and O. (2009, May 12). Fisheries and Oceans Canada | Pacific Region | Line-P Time-Series Program. Retrieved October 24, 2019, from http://www.waterproperties.ca/linep/

Greene Richard M., Geider Richard J., & Falkowski Paul G. (2003). Effect of iron limitation on photosynthesis in a marine diatom. *Limnology and Oceanography*, *36*(8), 1772–1782. https://doi.org/10.4319/lo.1991.36.8.1772

Hama, T., Miyazaki, T., Ogawa, Y., Iwakuma, T., Takahashi, M., Otsuki, A., & Ichimura, S. (1983). Measurement of photosynthetic production of a marine phytoplankton population

using a stable 13C isotope. *Marine Biology*, *73*(1), 31–36. https://doi.org/10.1007/BF00396282

Hamme, R. C., Webley, P. W., Crawford, W. R., Whitney, F. A., DeGrandpre, M. D., Emerson, S. R., et al. (2010). Volcanic ash fuels anomalous plankton bloom in subarctic northeast Pacific. *Geophysical Research Letters*, *37*(19). https://doi.org/10.1029/2010GL044629

Harris, S. L., Varela, D. E., Whitney, F. W., & Harrison, P. J. (2009). Nutrient and phytoplankton dynamics off the west coast of Vancouver Island during the 1997/98 ENSO event. *Deep Sea Research Part II: Topical Studies in Oceanography*, *56*(24), 2487–2502. https://doi.org/10.1016/j.dsr2.2009.02.009

Harrison, P. J., Boyd, P. W., Varela, D. E., Takeda, S., Shiomoto, A., & Odate, T. (1999). Comparison of factors controlling phytoplankton productivity in the NE and NW subarctic Pacific gyres. *Progress in Oceanography*, *43*(2), 205–234. https://doi.org/10.1016/S0079-6611(99)00015-4

Harrison, Paul J., Whitney, F. A., Tsuda, A., Saito, H., & Tadokoro, K. (2004). Nutrient and Plankton Dynamics in the NE and NW Gyres of the Subarctic Pacific Ocean. *Journal of Oceanography*, *60*(1), 93–117. https://doi.org/10.1023/B:JOCE.0000038321.57391.2a

Hein, Pedersen, F, M., & Sand-Jensen. (1995). Size-dependent nitrogen uptake in micro- and macroalgae. *Marine Ecology Progress Series*, *118*, 247–253. https://doi.org/10.3354/meps118247

Helbling, E. W., Buma, A. G. J., Boelen, P., van der Strate, H. J., Giordanino, M. V. F., & Villafañe, V. E. (2011). Increase in Rubisco activity and gene expression due to elevated temperature partially counteracts ultraviolet radiation–induced photoinhibition in the

marine diatom Thalassiosira weissflogii. *Limnology and Oceanography*, *56*(4), 1330–1342. https://doi.org/10.4319/lo.2011.56.4.1330

Henson S. A., Sanders R., Allen J. T., Robinson I. S., & Brown L. 2003. Seasonal constraints on the estimation of new production from space using temperature-nitrate relationships. *Geophysical Research Letters, 30*(17): 1 912-1 915.

Hickey, B. M., & Banas, N. S. (2008). Why is the Northern End of the California Current System So Productive? *Oceanography*, *21*(4), 90–107.

Hildebrand, M. (2003). Biological processing of nanostructured silica in diatoms. *Progress in Organic Coatings*, *47*(3), 256–266. https://doi.org/10.1016/S0300-9440(03)00142-5

Hildebrand, M., Volcani, B. E., Gassmann, W., & Schroeder, J. I. (1997). A gene family of silicon transporters. *Nature*, *385*(6618), 688–689. https://doi.org/10.1038/385688b0

Hobday, A. J., Alexander, L. V., Perkins, S. E., Smale, D. A., Straub, S. C., Oliver, E. C. J., et al. (2016). A hierarchical approach to defining marine heatwaves. *Progress in Oceanography*, *141*, 227–238. https://doi.org/10.1016/j.pocean.2015.12.014

Hollowed, A. B., Barange, M., Beamish, R. J., Brander, K., Cochrane, K., Drinkwater, K., et al. (2013). Projected impacts of climate change on marine fish and fisheries. *ICES Journal of Marine Science*, *70*(5), 1023–1037. https://doi.org/10.1093/icesjms/fst081

Holmes, R. M., Aminot, A., Kérouel, R., Hooker, B. A., & Peterson, B. J. (1999). A simple and precise method for measuring ammonium in marine and freshwater ecosystems. *Canadian Journal of Fisheries and Aquatic Sciences*, *56*(10), 1801–1808. https://doi.org/10.1139/f99-128

Hutchins, D. A., Sedwick, P. N., DiTullio, G. R., Boyd, P. W., Quéguiner, B., Griffiths, F. B., & Crossley, C. (2001). Control of phytoplankton growth by iron and silicic acid availability

in the subantarctic Southern Ocean: Experimental results from the SAZ Project. *Journal of Geophysical Research: Oceans*, *106*(C12), 31559–31572. https://doi.org/10.1029/2000JC000333

Hutchins, D. A., & Bruland, K. W. (1998a). Iron-limited diatom growth and Si:N uptake ratios in a coastal upwelling regime. *Nature*, *393*(6685), 561–564. https://doi.org/10.1038/31203

Hutchins, David A., & Bruland, K. W. (1998b). Iron-limited diatom growth and Si:N uptake ratios in a coastal upwelling regime. *Nature*, *393*(6685), 561–564. https://doi.org/10.1038/31203

Ianson, D., Allen, S. E., Harris, S. L., Orians, K. J., Varela, D. E., & Wong, C. S. (2003). The inorganic carbon system in the coastal upwelling region west of Vancouver Island, Canada. *Deep Sea Research Part I: Oceanographic Research Papers*, *50*(8), 1023–1042. https://doi.org/10.1016/S0967-0637(03)00114-6

Ianson, D., Völker, C., Denman, K. L., Kunze, E., & Steiner, N. (2012). The effect of vertical and horizontal dilution on fertilized patch experiments. *Global biogeochemical cycles*, *26*(3).

Iwabuchi, B. L., & Gosselin, L. A. (2019). Long-term trends and regional variability in extreme temperature and salinity conditions experienced by coastal marine organisms on Vancouver Island, Canada. *Bulletin of Marine Science*, *95*(3), 337–354. https://doi.org/10.5343/bms.2018.0051

Kemp, A. E. S., Pike, J., Pearce, R. B., & Lange, C. B. (2000). The “Fall dump” — a new perspective on the role of a “shade flora” in the annual cycle of diatom production and export flux. *Deep Sea Research Part II: Topical Studies in Oceanography*, *47*(9), 2129–2154. https://doi.org/10.1016/S0967-0645(00)00019-9

Krause, J. W., Brzezinski, M. A., & Jones, J. L. (2011). Application of low-level beta counting of 32Si for the measurement of silica production rates in aquatic environments. *Marine Chemistry*, *127*(1), 40–47. https://doi.org/10.1016/j.marchem.2011.07.001

Krause, J. W., Brzezinski, M. A., Villareal, T. A., & Wilson, C. (2012). Increased kinetic efficiency for silicic acid uptake as a driver of summer diatom blooms in the North Pacific subtropical gyre. *Limnology and Oceanography*, *57*(4), 1084–1098. https://doi.org/10.4319/lo.2012.57.4.1084

Kristiansen, S., & Hoell, E. E. (2002). The importance of silicon for marine production*. *Hydrobiologia*, *484*(1), 21–31. https://doi.org/10.1023/A:1021392618824

Kroger, N. & Poulsen, N. (2008). Biochemistry and Molecular Genetics of Silica Biomineralization in Diatoms. *Handbook of Biomineralization*. https://doi.org/10.1002/9783527619443.ch3

Laffoley, D. and Baxter, J.M. eds., 2016. *Explaining ocean warming: Causes, scale, effects and consequences*. Gland, Switzerland: IUCN.

Lam, P. J., Bishop, J. K. B., Henning, C. C., Marcus, M. A., Waychunas, G. A., & Fung, I. Y. (2006). Wintertime phytoplankton bloom in the subarctic Pacific supported by continental margin iron. *Global Biogeochemical Cycles*, *20*(1). https://doi.org/10.1029/2005GB002557

Landry, M. R., Monger, B. C., & Selph, K. E. (1993). Time-dependency of microzooplankton grazing and phytoplankton growth in the subarctic Pacific. *Progress in Oceanography*, *32*(1), 205–222. https://doi.org/10.1016/0079-6611(93)90014-5

Le, T., & Bae, D. H. (2022). Causal influences of El Niño–Southern Oscillation on global dust activities. *Atmospheric Chemistry and Physics*, *22*(8), 5253–5263. https://doi.org/10.5194/acp-22-5253-2022

Levitus, S., United States, & National Oceanic and Atmospheric Administration. 1982. *Climatological atlas of the world ocean*.

Lewandowska, A.M., Hillebrand, H., Lengfellner, K. and Sommer, U. 2014. Temperature effects on phytoplankton diversity—The zooplankton link. *Journal of sea research*, *85*, pp.359 364.

Lindemann, C., Fiksen, Ø., Andersen, K. H., & Aksnes, D. L. (2016). Scaling Laws in Phytoplankton Nutrient Uptake Affinity. *Frontiers in Marine Science*, *3*. Retrieved from https://www.frontiersin.org/articles/10.3389/fmars.2016.00026

Lippiatt, S. M., Brown, M. T., Lohan, M. C., & Bruland, K. W. (2011). Reactive iron delivery to the Gulf of Alaska via a Kenai eddy. *Deep Sea Research Part I: Oceanographic Research Papers*, *58*(11), 1091–1102. https://doi.org/10.1016/j.dsr.2011.08.005

Lobban, C. S., & Harrison, P. J. (1994). *Seaweed Ecology and Physiology*. Cambridge: Cambridge University Press. https://doi.org/10.1017/CBO9780511626210

Lomas, M. W., & Glibert, P. M. (2000). Comparisons of Nitrate Uptake, Storage, and Reduction in Marine Diatoms and Flagellates. *Journal of Phycology*, *36*(5), 903–913. https://doi.org/10.1046/j.1529-8817.2000.99029.x

Lozier, M. S., Dave, A. C., Palter, J. B., Gerber, L. M., & Barber, R. T. (2011). On the relationship between stratification and primary productivity in the North Atlantic. *Geophysical Research Letters*, *38*(18). https://doi.org/10.1029/2011GL049414

Lund, J. W. G., Kipling, C., & Le Cren, E. D. (1958). The inverted microscope method of estimating algal numbers and the statistical basis of estimations by counting. *Hydrobiologia*, *11*(2), 143–170. https://doi.org/10.1007/BF00007865

MacIsaac, J. J., & Dugdale, R. C. (1969). The kinetics of nitrate and ammonia uptake by natural populations of marine phytoplankton. *Deep Sea Research and Oceanographic Abstracts*, *16*(1), 45–57. https://doi.org/10.1016/0011-7471(69)90049-7

Makareviciute-Fichtner, K., Matthiessen, B., Lotze, H. K., & Sommer, U. (2021). Phytoplankton nutritional quality is altered by shifting Si:N ratios and selective grazing. *Journal of Plankton Research*, *43*(3), 325–337. https://doi.org/10.1093/plankt/fbab034

Maldonado, M. T., Boyd, P. W., Harrison, P. J., & Price, N. M. (1999). Co-limitation of phytoplankton growth by light and Fe during winter in the NE subarctic Pacific Ocean. *Deep Sea Research Part II: Topical Studies in Oceanography*, *46*(11), 2475–2485. https://doi.org/10.1016/S0967-0645(99)00072-7

Malviya, S., Scalco, E., Audic, S., Vincent, F., Veluchamy, A., Poulain, J., et al. (2016). Insights into global diatom distribution and diversity in the world's ocean. *Proceedings of the National Academy of Sciences*, *113*(11), E1516–E1525. https://doi.org/10.1073/pnas.1509523113

Marbà, N., & Duarte, C. M. (2010). Mediterranean warming triggers seagrass (Posidonia oceanica) shoot mortality. *Global Change Biology*, *16*(8), 2366–2375. https://doi.org/10.1111/j.1365-2486.2009.02130.x

Marchetti, A., Maldonado, M. T., Lane, E. S., & Harrison, P. J. (2006). Iron requirements of the pennate diatom Pseudo-nitzschia: Comparison of oceanic (high-nitrate, low-chlorophyll

waters) and coastal species. *Limnology and Oceanography*, *51*(5), 2092–2101. https://doi.org/10.4319/lo.2006.51.5.2092

Marchetti, A., Sherry, N. D., Kiyosawa, H., Tsuda, A., & Harrison, P. J. (2006). Phytoplankton processes during a mesoscale iron enrichment in the NE subarctic Pacific: Part I—Biomass and assemblage. *Deep Sea Research Part II: Topical Studies in Oceanography*, *53*(20), 2095–2113. https://doi.org/10.1016/j.dsr2.2006.05.038

Martin, J. H., & Fitzwater, S. E. (1988). Iron deficiency limits phytoplankton growth in the north-east Pacific subarctic. *Nature*, *331*(6154), 341–343. https://doi.org/10.1038/331341a0

Martin-Jézéquel, V., Hildebrand, M., & Brzezinski, M.A. (2003). Silicon metabolism in diatoms: Implications for growth.*Journal of Phycology*, *35*(5), 821-840.

Meyer, M. G., Gong, W., Kafrissen, S. M., Torano, O., Varela, D. E., Santoro, A. E., et al. (2022). Phytoplankton size-class contributions to new and regenerated production during the EXPORTS Northeast Pacific Ocean field deployment. *Elementa: Science of the Anthropocene*, *10*(1), 00068. https://doi.org/10.1525/elementa.2021.00068

Mills, K. E., Pershing, A. J., Brown, C. J., Chen, Y., Chiang, F.-S., Holland, D. S., et al. (2013). Fisheries Management in a Changing Climate: Lessons from the 2012 Ocean Heat Wave in the Northwest Atlantic. *Oceanography*, *26*(2), 191–195.

Morel F.M.M. (1986) Trace metals - phytoplankton interactions: an overview. In: Laserre P, Martin JM (eds). Biogeochemical processes at the land-sea boundary. Elsevier, Amsterdam, pp 177- 189.

Mosseri, J., Quéguiner, B., Armand, L., & Cornet-Barthaux, V. (2008). Impact of iron on silicon utilization by diatoms in the Southern Ocean: A case study of Si/N cycle decoupling in a

naturally iron-enriched area. *Deep Sea Research Part II: Topical Studies in Oceanography*, *55*(5), 801–819. https://doi.org/10.1016/j.dsr2.2007.12.003

Mulvenna, P. F., & Savidge, G. (1992). A modified manual method for the determination of urea in seawater using diacetylmonoxime reagent. *Estuarine Coastal and Shelf Science*, *34*, 429–438. https://doi.org/10.1016/S0272-7714(05)80115-5

Nelson, D. M., & Brzezinski, M. A. (1990). Kinetics of silicic acid uptake by natural diatom assemblages in two Gulf Stream warm-core rings. *Marine Ecology Progress Series*, *62*(3), 283–292.

Nelson, D. M., & Tréguer, P. (1992). Role of silicon as a limiting nutrient to Antarctic diatoms: evidence from kinetic studies in the Ross Sea ice-edge zone. *Marine Ecology Progress Series*, *80*(2/3), 255–264.

Nelson, D. M., Brzezinski, M. A., Sigmon, D. E., & Franck, V. M. (2001). A seasonal progression of Si limitation in the Pacific sector of the Southern Ocean. *Deep Sea Research Part II: Topical Studies in Oceanography*, *48*(19), 3973–3995. https://doi.org/10.1016/S0967-0645(01)00076-5

Nelson David M., Tréguer Paul, Brzezinski Mark A., Leynaert Aude, & Quéguiner Bernard. (2012). Production and dissolution of biogenic silica in the ocean: Revised global estimates, comparison with regional data and relationship to biogenic sedimentation. *Global Biogeochemical Cycles*, *9*(3), 359–372. https://doi.org/10.1029/95GB01070

Nielsen, J. M., Rogers, L. A., Brodeur, R. D., Thompson, A. R., Auth, T. D., Deary, A. L., et al. (2021). Responses of ichthyoplankton assemblages to the recent marine heatwave and previous climate fluctuations in several Northeast Pacific marine ecosystems. *Global Change Biology*, *27*(3), 506–520. https://doi.org/10.1111/gcb.15415

Noh, K. M., Lim, H.-G., & Kug, J.-S. (2022). Global chlorophyll responses to marine heatwaves in satellite ocean color. *Environmental Research Letters*, *17*(6), 064034. https://doi.org/10.1088/1748-9326/ac70ec

O' Loughlin, J. H. O. et al. (2020) Implications of *Pyrosoma atlanticum* range expansion on phytoplankton standing stocks in the Northern California Current. *Progress in Oceanography* **188**, 1–9.

Obayashi, Y., Tanoue, E., Suzuki, K., Handa, N., Nojiri, Y., & Wong, C. S. (2001). Spatial and temporal variabilities of phytoplankton community structure in the northern North Pacific as determined by phytoplankton pigments. *Deep Sea Research Part I: Oceanographic Research Papers*, *48*(2), 439–469. https://doi.org/10.1016/S0967-0637(00)00036-4

Oliver, E. C. J., Burrows, M. T., Donat, M. G., Sen Gupta, A., Alexander, L. V., Perkins-Kirkpatrick, S. E., et al. (2019). Projected Marine Heatwaves in the 21st Century and the Potential for Ecological Impact. *Frontiers in Marine Science*, *6*. Retrieved from https://www.frontiersin.org/articles/10.3389/fmars.2019.00734

Pauli, N.C., Flintrop, C.M., Konrad, C., Pakhomov, E.A., Swoboda, S., Koch, F., Wang, X.L., Zhang, J.C., Brierley, A.S., Bernasconi, M. and Meyer, B., (2021). Krill and salp faecal pellets contribute equally to the carbon flux at the Antarctic Peninsula. *Nature Communications*, *12*(1), p.7168.

Peña, M. A., & Varela, D. E. (2007). Seasonal and interannual variability in phytoplankton and nutrient dynamics along Line P in the NE subarctic Pacific. *Progress in Oceanography*, *75*(2), 200–222. https://doi.org/10.1016/j.pocean.2007.08.009

Peña, M. A., Nemcek, N., & Robert, M. (2019). Phytoplankton responses to the 2014–2016 warming anomaly in the northeast subarctic Pacific Ocean. *Limnology and Oceanography*, *64*(2), 515–525. https://doi.org/10.1002/lno.11056

Pomeroy, L. R. (1974). The Ocean's Food Web, A Changing Paradigm. *BioScience*, *24*(9), 499–504. https://doi.org/10.2307/1296885

Quéguiner, B. 2001. Biogenic silica production in the Australian sector of the Subantarctic Zone of the Southern Ocean in late summer 1998. *Journal of Geophysical Research*, *106*(C12), 31,627-31,636.

Ratnarajah, L., Abu-Alhaija, R., Atkinson, A. *et al.* (2023). Monitoring and modelling marine zooplankton in a changing climate. *Nat Commun* **14**, 564 https://doi.org/10.1038/s41467-023-36241-5

Raven, J. A. (1988). The iron and molybdenum use efficiencies of plant growth with different energy, carbon and nitrogen sources. *New Phytologist*, *109*(3), 279–287. https://doi.org/10.1111/j.1469-8137.1988.tb04196.x

Ribalet, F., Marchetti, A., Hubbard, K. A., Brown, K., Durkin, C. A., Morales, R., et al. (2010). Unveiling a phytoplankton hotspot at a narrow boundary between coastal and offshore waters. *Proceedings of the National Academy of Sciences*, *107*(38), 16571–16576. https://doi.org/10.1073/pnas.1005638107

Richardson, A.J. (2008). In hot water: zooplankton and climate change, *ICES Journal of Marine Science*, 65(3), 79–295, https://doi.org/10.1093/icesjms/fsn028

Rocha, C. L. D. L., Hutchins, D. A., Brzezinski, M. A., & Zhang, Y. (2000). Effects of iron and zinc deficiency on elemental composition and silica production by diatoms. *Marine Ecology Progress Series*, *195*, 71–79. https://doi.org/10.3354/meps195071

Roche, J. L., Boyd, P. W., McKay, R. M. L., & Geider, R. J. (1996). Flavodoxin as an in situ marker for iron stress in phytoplankton. *Nature*, *382*(6594), 802–805. https://doi.org/10.1038/382802a0

Rose, J. M., & Caron, D. A. (2007). Does low temperature constrain the growth rates of heterotrophic protists? Evidence and implications for algal blooms in cold waters. *Limnology and Oceanography*, *52*(2), 886–895. https://doi.org/10.4319/lo.2007.52.2.0886

Ross, T., Jackson, J., & Hannah, C. (2021). The Northeast Pacific: Update on marine heatwave status and trends. *PICES Press*, *29*(1), 46–48.

Royer, S.-J., Levasseur, M., Lizotte, M., Arychuk, M., Scarratt, M. G., Wong, C. S., et al. (2010). Microbial dimethylsulfoniopropionate (DMSP) dynamics along a natural iron gradient in the northeast subarctic Pacific. *Limnology and Oceanography*, *55*(4), 1614–1626. https://doi.org/10.4319/lo.2010.55.4.1614

Salisbury, F.B. & Ross, C.W. (1978) Plant physiology. Wadsworth Publishing Company, Belmont, California.

Sarmiento, J. L., Slater, R., Barber, R., Bopp, L., Doney, S. C., Hirst, A. C., et al. (2004). Response of ocean ecosystems to climate warming. *Global Biogeochemical Cycles*, *18*(3). https://doi.org/10.1029/2003GB002134

Shanks, A. L., Rasmuson, L. K., Valley, J. R., Jarvis, M. A., Salant, C., Sutherland, D. A., et al. (2020). Marine heat waves, climate change, and failed spawning by coastal invertebrates. *Limnology and Oceanography*, *65*(3), 627–636. https://doi.org/10.1002/lno.11331

Smetacek, V., Klaas, C., Strass, V. H., Assmy, P., Montresor, M., Cisewski, B., et al. (2012). Deep carbon export from a Southern Ocean iron-fertilized diatom bloom. *Nature*, *487*(7407), 313–319. https://doi.org/10.1038/nature11229

Sommer, U., & Lewandowska, A. 2011. Climate change and the phytoplankton spring bloom: warming and overwintering zooplankton have similar effects on phytoplankton. *Global Change Biology, 17* (1) pp. 154-162

Stoecker, D., Taniguchi, A., & Michaels, A. (1989). Abundance of autotrophic, mixotrophic and heterotrophic planktonic ciliates in shelf and slope waters. *Marine Ecology-Progress Series - MAR ECOL-PROGR SER*, *50*, 241–254. https://doi.org/10.3354/meps050241

Street, J. H., & Paytan, A. (2005). Iron, phytoplankton growth, and the carbon cycle. *Metal Ions in Biological Systems*, *43*, 153–193. https://doi.org/10.1201/9780824751999.ch7

Strickland J. D. 1970. The Ecology of the Plankton Off La Jolla, California, in the Period April Through September, 1967. University of California Press, California, USA. p.1-22.

Strickland, J. D., & Parsons, T. R. 1972. A Practical Handbook of Seawater Analysis. 2nd edition. Ottawa, Canada, Fisheries Research Board of Canada, 310pp. (Bulletin Fisheries Research Board of Canada, Nr. 167 (2nd ed)). DOI: http://dx.doi.org/10.25607/OBP-179

Suess E., & Thiede J. 1983. Coastal Upwelling Its Sediment Record. Springer US, New York, USA. p.61-83.

Tabata, S. (1975). The general circulation of the Pacific Ocean and a brief account of the oceanographic structure of the North Pacific Ocean Part I - circulation and volume transports. *Atmosphere*, *13*(4), 133–168. https://doi.org/10.1080/00046973.1975.9648394

Takeda, S. (1998). Influence of iron availability on nutrient consumption ratio of diatoms in oceanic waters. *Nature*, *393*(6687), 774–777. https://doi.org/10.1038/31674

Taylor, F., & Haigh, R. (1996). Spatial and temporal distributions of microplankton during the summers of 1992–1993 in Barkley Sound, British Columbia, with emphasis on harmful species. *Canadian Journal of Fisheries and Aquatic Sciences*, *53*(10), 2310–2322. https://doi.org/10.1139/f96-181

Thamatrakoln, K., & Hildebrand, M. (2008). Silicon Uptake in Diatoms Revisited: A Model for Saturable and Nonsaturable Uptake Kinetics and the Role of Silicon Transporters. *Plant Physiology*, *146*(3), 1397–1407. https://doi.org/10.1104/pp.107.107094

Thomson, R. E. (1981). *Oceanography of the British Columbia coast*. Ottawa: Dept. of Fisheries and Oceans.

Timmermans, K.R., Stolte, W. & de Barr, H.J.W. (1994). Iron-mediated effects on nitrate reductase in marine phytoplankton. *Marine Biology*, *121*, 389-396.

Tréguer, P., Nelson, D. M., Van Bennekom, A. J., DeMaster, D. J., Leynaert, A., & Quéguiner, B. (1995). The Silica Balance in the World Ocean: A Reestimate. *Science*, *268*(5209), 375–379.

Tréguer, P. J., & De La Rocha, C. L. (2013). The World Ocean Silica Cycle. *Annual Review of Marine Science*, *5*(1), 477–501. https://doi.org/10.1146/annurev-marine-121211-172346

Trombetta, T., Vidussi, F., Mas, S., Parin, D., Simier, M., & Mostajir, B. (2019). Water temperature drives phytoplankton blooms in coastal waters. *PLOS ONE*, *14*(4), e0214933. https://doi.org/10.1371/journal.pone.0214933

Varela, D. E., & Harrison, P. J. (1999). Seasonal variability in nitrogenous nutrition of phytoplankton assemblages in the northeastern subarctic Pacific Ocean. *Deep Sea*

Research Part II: Topical Studies in Oceanography, *46*(11), 2505–2538. https://doi.org/10.1016/S0967-0645(99)00074-0

Wafar, M. V. M., Le Corre, P., & L'Helguen, S. (1995). *f*-Ratios calculated with and without urea uptake in nitrogen uptake by phytoplankton. *Deep Sea Research Part I: Oceanographic Research Papers*, *42*(9), 1669–1674. https://doi.org/10.1016/0967-0637(95)00066-F

Wernberg, T., Smale, D. A., Tuya, F., Thomsen, M. S., Langlois, T. J., de Bettignies, T., et al. (2013). An extreme climatic event alters marine ecosystem structure in a global biodiversity hotspot. *Nature Climate Change*, *3*(1), 78–82. https://doi.org/10.1038/nclimate1627

Whitney, F., Wong, C., & Boyd, P. (1998). Interannual variability in nitrate supply to surface waters of the Northeast Pacific Ocean. *Marine Ecology Progress Series*, *170*, 15–23. https://doi.org/10.3354/meps170015

Whitney, F. A, & Freeland, H. J. (1999). Variability in upper-ocean water properties in the NE Pacific Ocean. *Deep Sea Research Part II: Topical Studies in Oceanography*, *46*(11), 2351–2370. https://doi.org/10.1016/S0967-0645(99)00067-3

Whitney, F. A., & Welch, D. W. (2002). Impact of the 1997–1998 El Niño and 1999 La Niña on nutrient supply in the Gulf of Alaska. *Progress in Oceanography*, *54*(1), 405–421. https://doi.org/10.1016/S0079-6611(02)00061-7

Whitney, Frank A., Crawford, D. W., & Yoshimura, T. (2005). The uptake and export of silicon and nitrogen in HNLC waters of the NE Pacific Ocean. *Deep Sea Research Part II: Topical Studies in Oceanography*, *52*(7–8), 1055–1067. https://doi.org/10.1016/j.dsr2.2005.02.006

Wildman, S. G. (2002). Along the trail from Fraction I protein to Rubisco (ribulose bisphosphate carboxylase-oxygenase). *Photosynthesis Research*, *73*(1–3), 243–250. https://doi.org/10.1023/A:1020467601966

Wyatt, A., Resplandy, L., & Marchetti, A. (2022). Ecosystem impacts of marine heat waves in the Northeast Pacific. *EGUsphere*, 1–24. https://doi.org/10.5194/egusphere-2022-17

Xu, T., Newman, M., Capotondi, A., & Di Lorenzo, E. (2021). The Continuum of Northeast Pacific Marine Heatwaves and Their Relationship to the Tropical Pacific. *Geophysical Research Letters*, *48*(2), 2020GL090661. https://doi.org/10.1029/2020GL090661

Yamaguchi, R., Rodgers, K. B., Timmermann, A., Stein, K., Schlunegger, S., Bianchi, D., et al. (2022). Trophic level decoupling drives future changes in phytoplankton bloom phenology. *Nature Climate Change*, *12*(5), 469–476. https://doi.org/10.1038/s41558-022-01353-1

Yamamoto, T., Kishigami, T., & Nakagawa, H. (2017). Uptake kinetics of nitrate, ammonia and phosphate by the dinoflagellate Heterocapsa circularisquama isolated from Hiroshima Bay, Japan. *Phycological Research*, *65*(4), 333–339. https://doi.org/10.1111/pre.12193

Yasunaka, S., Mitsudera, H., Whitney, F., & Nakaoka, S. (2021). Nutrient and dissolved inorganic carbon variability in the North Pacific. *Journal of Oceanography*, *77*(1), 3–16. https://doi.org/10.1007/s10872-020-00561-7

Yentsch, C. S., & Menzel, D. W. (1963). A method for the determination of phytoplankton chlorophyll and phaeophytin by fluorescence. *Deep Sea Research and Oceanographic Abstracts*, *10*(3), 221–231. https://doi.org/10.1016/0011-7471(63)90358-9

Young, J. N., Heureux, A. M. C., Sharwood, R. E., Rickaby, R. E. M., Morel, F. M. M., & Whitney, S. M. (2016). Large variation in the Rubisco kinetics of diatoms reveals

diversity among their carbon-concentrating mechanisms. *Journal of Experimental Botany*, *67*(11), 3445–3456. https://doi.org/10.1093/jxb/erw163

Zhang, H.-R., Wang, Y., Xiu, P., Qi, Y., & Chai, F. (2021). Roles of Iron Limitation in Phytoplankton Dynamics in the Western and Eastern Subarctic Pacific. *Frontiers in Marine Science*, *8*. Retrieved from https://www.frontiersin.org/articles/10.3389/fmars.2021.735826

Zhu, Z., Qu, P., Fu, F., Tennenbaum, N., Tatters, A. O., & Hutchins, D. A. (2017). Understanding the blob bloom: Warming increases toxicity and abundance of the harmful bloom diatom Pseudo-nitzschia in California coastal waters. *Harmful Algae*, *67*, 36–43. https://doi.org/10.1016/j.hal.2017.06.004

Appendix I

Appendix I includes additional data that are not presented in the results section (2.4) of Chapter 2 of this thesis.

Table A1. Physical properties of the water column from main stations along the Line P transect in September 2018.

Criuse	Lat	Long	Station	Depth	Temp.	MLD	Salinity	Dissolved Oxygen
	N	W		m	°C	m	PSU	mL L^{-1}
Line P	48.66	-126.66	P4	2	15.34	13	32.2	6.27
Line P	48.66	-126.66	P4	5	15.32	13	32.2	6.31
Line P	48.66	-126.66	P4	10	15.14	13	32.2	6.3
Line P	48.66	-126.66	P4	15	14.6	13	32.2	6.22
Line P	48.66	-126.66	P4	35	10.25	13	32.4	5.99
Line P	48.66	-126.66	P4	75	8.6	13	32.9	3.92
Line P	48.97	-130.66	P12	2	16.6	43	32.3	5.69
Line P	48.97	-130.66	P12	5	16.6	43	32.3	5.71
Line P	48.97	-130.66	P12	8	16.6	43	32.3	5.71
Line P	48.97	-130.66	P12	15	16.6	43	32.3	5.7
Line P	48.97	-130.66	P12	45	13.6	43	32.4	6.2
Line P	48.97	-130.66	P12	60	10.1	43	32.5	6.82
Line P	49.28	-134.67	P16	2	15.7	26	32.3	5.82
Line P	49.28	-134.67	P16	5	15.7	26	32.3	5.82
Line P	49.28	-134.67	P16	15	15.7	26	32.3	5.81
Line P	49.28	-134.67	P16	20	15.7	26	32.3	5.84
Line P	49.28	-134.67	P16	40	10.9	26	32.4	7.01
Line P	49.28	-134.67	P16	75	7.21	26	32.4	6.49
Line P	49.57	-138.67	P20	2	15.2	28	32.3	5.95
Line P	49.57	-138.67	P20	7	15.2	28	32.3	5.97
Line P	49.57	-138.67	P20	15	15.2	28	32.3	5.93

Line P	49.57	-138.67	P20	25	15.1	28	32.5	5.98
Line P	49.57	-138.67	P20	65	6.8	28	32.5	6.63
Line P	49.57	-138.67	P20	80	6.39	28	32.5	6.41
Line P	50.29	-144.37	P26	2	13.9	33	32.3	6.16
Line P	50.29	-144.37	P26	5	13.9	33	32.3	6.16
Line P	50.29	-144.37	P26	15	14	33	32.3	6.13
Line P	50.29	-144.37	P26	25	14	33	32.3	6.14
Line P	50.29	-144.37	P26	50	8.74	33	32.4	7.02
Line P	50.29	-144.37	P26	80	6.38	33	32.5	6.87

Table A2. Dissolved nutrients from the euphotic zone at the five main stations along the Line P transect in September 2018.

Station	Depth	NO3	PO_4	$SiOH_4$	NH_4	Urea
	m	µmol L^{-1}	µmol L^{-1}	µmol L^{-1}	µmol L^{-1}	µmol L^{-1}
P4	2	0.9	0.42	8	0.02039	< 0.1
P4	5	0.9	0.44	7.9	0.00281	< 0.1
P4	10	1	0.42	7.7	0.02835	< 0.1
P4	15	1.8	0.5	7.6	0.26472	< 0.1
P4	35	7.8	0.95	10	0.72615	< 0.1
P4	75	15.8	1.35	16	0.00000	< 0.1
P12	2	<0.1	0.32	1.3	0.00486	< 0.1
P12	5	<0.1	0.32	1.3	0.00000	< 0.1
P12	8	<0.1	0.32	1.3	0.00136	< 0.1
P12	15	<0.1	0.32	1.3	0.00000	< 0.1
P12	45	0.2	0.43	1.3	0.01534	< 0.1
P12	60	3.2	0.71	3.6	0.81564	< 0.1
P16	2	<0.1	0.38	0.1	0.02653	< 0.1
P16	5	<0.1	0.37	0.2	0.03807	< 0.1
P16	15	0.2	0.4	0.2	0.03020	< 0.1
P16	20	<0.1	0.39	0.2	0.03145	< 0.1
P16	40	2.8	0.66	1	0.53394	< 0.1
P16	75	11.2	1.15	9.1	0.00000	< 0.1
P20	2	5.2	0.74	4.8	2.86730	< 0.1
P20	7	5.2	0.74	4.7	6.26437	< 0.1
P20	15	5.2	0.74	4.6	0.10572	< 0.1
P20	25	5.1	0.75	4.8	0.14769	0.13
P20	65	12.4	1.25	13	0.02220	< 0.1
P20	80	13.9	1.32	14.9	0.00000	< 0.1
P26	2	7.9	0.86	16.4	0.05840	< 0.1
P26	5	8	0.87	16.3	0.05097	< 0.1
P26	15	7.9	0.86	16.3	0.05466	< 0.1

P26	25	8	0.86	16.3	0.06323	< 0.1
P26	50	10.6	1.08	15.7	0.44659	< 0.1
P26	80	15.5	1.33	18.7	0.03990	< 0.1

Table A3. Particulate data from the euphotic zone at the five main stations along the Line P transect in September 2018.

Station	Depth	bSiO2	Chl-a Total	Chl-a >5 µm	Chl-a <5 µm	PC	PC	PN
	m	µM	µg L^{-1}	µg L^{-1}	µg L^{-1}	µg L^{-1}	µM	µM
P4	2	0.27	1.09	0.07	0.85	381.42	31.75	5.26
P4	5	0.29	0.94	0.05	0.82	361.99	30.14	4.79
P4	10	0.28	1.17	0.16	0.96	369.88	30.79	5.05
P4	15	0.36	1.17	0.09	0.98	290.87	24.22	3.71
P4	35	0.35	0.47	0.03	0.32	293.21	24.41	3.70
P4	75	0.11	0.06	0.02	0.05	263.64	21.95	3.27
P12	2	0.10	0.18	0.03	0.13	100.66	8.38	0.99
P12	5	0.23	0.99	0.08	0.96	104.48	8.70	1.05
P12	8	0.07	0.14	0.05	0.10	92.68	7.72	0.92
P12	15	0.06	0.19	0.05	0.10	227.55	18.95	1.05
P12	45	0.10	0.65	0.11	0.41	115.20	9.60	1.15
P12	60	0.09	0.45	0.12	0.27	110.03	9.16	1.24
P16	2	0.10	0.14	0.03	0.11	101.15	8.42	1.57
P16	5	0.11	0.16	0.02	0.10	93.89	7.82	2.14
P16	15	0.12	0.15			108.18	9.01	1.07
P16	20	0.11	0.15			108.29	9.02	1.16
P16	40	0.07	0.22	0.07	0.12	112.02	9.33	1.35
P16	75	0.09	0.15	0.02	0.11	109.71	9.14	2.13
P20	2	0.39	0.21	0.08	0.09	103.57	8.62	1.55
P20	7	0.27	0.22	0.09	0.12	99.69	8.30	1.23
P20	15	0.28	0.22	0.08	0.10	104.03	8.70	1.56
P20	25	0.31	0.26	0.07	0.11	123.36	10.27	1.17
P20	65	0.15	0.23	0.04	0.15	108.84	9.06	1.12
P20	80	0.15	0.17	0.03	0.12	105.49	8.78	1.60
P26	2	0.57	0.30	0.11	0.17	130.56	10.87	1.99
P26	5	0.54	0.37	0.09	0.17	133.39	11.11	2.61

P26	15	0.29	0.34	0.09	0.16	132.32	11.02	1.80
P26	25	0.32	0.28	0.10	0.21	133.97	11.16	1.48
P26	50	0.34	0.24	0.06	0.20	122.78	10.22	1.84
P26	80	0.44	0.14	0.02	0.13	121.72	10.14	1.50

Table A4. Carbon (ρC), nitrate (NO_3), ammonium (ρNH_4), urea (ρUrea-N), and silicon (ρSi) uptake rates from the euphotic zone at the five main stations along the Line P transect in September 2018.

Station	Depth	ρC	ρNO_3	ρNH_4	ρUrea-N	ρSi
	m	μmol C L^{-1} day^{-1}	μmol NO_3 L^{-1} day^{-1}	μmol NH_4 L^{-1} day^{-1}	μmol Urea L^{-1} day^{-1}	μmol Si L^{-1} day^{-1}
P4	2	6.23	0.80	0.14	0.46	1.11
P4	5	6.11	0.81	0.14	0.46	0.85
P4	10	5.89	0.76	0.15	0.00	0.98
P4	15	4.82	1.23	0.29	0.40	0.70
P4	35	0.46	0.09	0.07	0.03	1.29
P4	75	0.06	0.00	0.01	0.02	1.67
P12	2	0.48	0.15	0.14	0.14	0.19
P12	5	0.51	0.15	0.14	0.16	0.07
P12	8	0.45	0.12	0.15	0.13	0.14
P12	15	0.41	0.14	0.29	0.12	0.04
P12	45	0.36	0.02	0.07	0.11	0.04
P12	60	0.02	0.03	0.01	0.01	0.10
P16	2	0.84	0.10	0.15	0.13	0.02
P16	5	0.85	0.09	0.17	0.12	0.03
P16	15	0.84	0.12	0.15	0.12	0.04
P16	20	0.73	0.07	0.16	0.10	0.04
P16	40	0.07	0.03	0.04	0.01	0.21
P16	75	0.00	0.06	0.01	0.01	1.85
P20	2	0.83	0.10	1.17	0.09	0.48
P20	7	0.80	0.11	2.45	0.07	0.50
P20	15	0.89	0.09	0.11	0.08	0.53
P20	25	0.80	0.10	0.11	0.06	0.47
P20	65	0.11	0.05	0.03	0.03	0.86
P20	80	0.00	0.02	0.01	0.01	0.56

P26	2	0.91	0.06	0.08	0.06	3.00
P26	5	0.89	0.06	0.09	0.06	3.08
P26	15	0.83	0.05	0.06	0.05	2.25
P26	25	1.01	0.07	0.08	0.06	4.62
P26	50	0.09	0.00	0.03	0.01	4.74
P26	80	0.01	0.00	0.01	0.00	4.40

Appendix II

Appendix II includes additional data that is not presented in the results section (3.3) of Chapter 3.

Table A5. Particulate carbon (PC) and nitrogen (PN), and carbon (ρC) and nitrate (ρNO_3) uptake rates from mixed layer at 5 m and at the chl-max depth in August-September 2019. ρC and ρNO_3 are presented as both depth specific (μmol L^{-1} day^{-1}) and integrated (mmol m^{-2} day^{-1}) uptake rates.

Stn	Depth	PN	PC	PC	ρNO_3	Int. ρNO_3	ρC	ρC	Int. ρC
	m	μM	μg L^{-1}	μM	μM day^{-1}	mmol m^{-2} day^{-1}	μg L^{-1} day^{-1}	μM day^{-1}	mg m^{-2} day^{-1}
P4	5	1.04	97.04	8.07	0.07	1.35	10.18	0.84	265.34
P4	37	1.31	100.9	8.41	0.02		6.40	0.53	
P12	5	0.89	85.20	7.09	0.05	1.83	11.87	0.99	706.03
P12	39	2.46	196.1	16.35	0.06		29.66	2.47	
P16	5	1.47	136.2	11.33	0.06	0.95	8.25	0.69	139.53
P16	34	2.31	169.1	14.10	0.01		1.37	0.11	
P20	5	0.90	90.10	7.50	0.06	1.49	8.04	0.67	300.54
P20	39	2.08	167.0	13.92	0.03		9.64	0.80	
P26	5	2.23	177.5	14.77	0.26	4.09	24.10	2.01	360.00
P26	35	2.05	160.6	13.4	0.01		0.00	0	
LB15	5	1.05	110.2	9.17	0.14	3.14	10.87	0.91	306.20
LB15	48	0.98	86.78	7.22	0.01		3.37	0.28	
LC06	5	3.27	228.19	19.0	0.66	2.47	59.31	4.94	215.95
LC06	12	1.83	117.9	9.82	0.05		2.40	0.20	
LG09	5	1.26	134.4	11.18	0.47	7.68	12.60	1.05	260.85
LG09	37	1.67	125.1	10.41	0.01		3.70	0.31	
LBP3	5	2.14	195.2	16.30	0.10	2.36	25.54	2.13	487.99
LBP3	25	3.38	266.6	22.18	0.13		23.26	1.94	
CS02	5	3.80	364.8	30.35	0.06	3.57	0.00	0	49.94
CS02	17	4.45	257.4	21.42	0.54		8.32	0.69	

Table A6. Chlorophyll-a size fractions from stations sampled in August-September 2019. Samples were collected from 5 m and the chl-max depth at each station.

Station	Depth	Chl-a >20 µm	Chl-a 5-20 µm	Chl-a <5 µm
	m	µg L^{-1}	µg L^{-1}	µg L^{-1}
P4	5	0	0.01	0.07
	37	0.06	0.04	0.19
P12	5	0	0.01	0.09
	39	0.03	0.07	0.53
P16	5	0	0.01	0.15
	34	0.01	0.07	0.61
P20	5	0	0.01	0.13
	39	0.31	0.2	0.44
P26	5	0.02	0.06	0.39
	34	0.23	0.25	0.5
LB01	5	0.29	0.62	1.46
	0	0.5	1.21	2.62
LB15	5	0.03	0.02	0.17
	48	0.052	0.07	0.39
LC06	5	0.39	0.24	0.86
	12	0.26	0.11	0.66
LG09	5	0.04	0.04	0.22
	37	0.11	0.11	0.52
LBP3	5	0.01	0	0.02
	25	3.39	0.23	0.21
CS02	5	0.07	0.14	1
	17	0.083	0.2	1.45

Table A7. Silicon (Si) and nitrate (NO_3) kinetic experiments data. Specific (V) and absolute (ρ) uptake rates were measured at ambient nutrient values and at each enrichment level for each station.

Stn-Enrichment	V-Si	ρSi	V-NO_3	ρNO_3
	hr^{-1}	μM day^{-1}	hr^{-1}	μM day^{-1}
LB15-Ambient	0.001	0.013	0.006	0.135
LB15-1uM	0.004	0.089	0.005	0.143
LB15-2uM	0.005	0.122	0.004	0.140
LB15-3uM	0.006	0.152	0.005	0.142
LB15-4uM	0.007	0.187	0.005	0.180
LB15-8uM	0.009	0.236	0.005	0.157
LB15-12uM	0.014	0.365	0.005	0.191
LB15-20uM	0.018	0.518	0.007	0.175
LG09-Ambient	0.002	0.039	0.011	0.660
LG09-1uM	0.010	0.266	0.008	0.586
LG09-2uM	0.013	0.343	0.008	0.542
LG09-3uM	0.011	0.287	0.008	0.581
LG09-4uM	0.013	0.330	0.007	0.534
LG09-8uM	0.016	0.416	0.008	0.516
LG09-12uM	0.019	0.525	0.007	0.596
LG09-20uM	0.022	0.620	0.008	0.622
LC06-Ambient	0.027	1.206	0.020	0.470
LC06-1uM	0.028	1.229	0.009	0.341
LC06-2uM	0.028	1.206	0.006	0.245
LC06-3uM	0.031	1.393	0.007	0.246
LC06-4uM	0.035	1.665	0.005	0.243
LC06-8uM	0.036	1.596	0.006	0.204
LC06-12uM	0.034	1.513	0.006	0.221
LC06-20uM	0.035	1.645	0.006	0.182
LBP3-Ambient	0.001	0.016	0.002	0.104
LBP3-1uM	0.010	0.173	0.003	0.143
LBP3-2uM	0.018	0.317	0.003	0.134

LBP3-3uM	0.019	0.359	0.002	0.122
LBP3-4uM	0.022	0.430	0.003	0.169
LBP3-8uM	0.028	0.597	0.004	0.190
LBP3-12uM	0.015	0.276	0.003	0.131
LBP3-20uM	0.038	0.936	0.003	0.154
CS02-Ambient	0.026	0.635	0.001	0.059
CS02-1uM	0.020	0.443	0.007	0.640
CS02-2uM	0.023	0.559	0.006	0.642
CS02-3uM	0.019	0.440	0.004	0.570
CS02-4uM	0.022	0.510	0.007	0.718
CS02-8uM	0.023	0.549	0.006	0.731
CS02-12uM	0.029	0.735	0.007	0.700
CS02-20uM	0.023	0.533	0.008	0.749
P4-Ambient	0.002	0.008	0.003	0.066
P4-1uM	0.003	0.010	0.004	0.162
P4-2uM	0.002	0.007	0.003	0.103
P4-3uM	0.003	0.013	0.005	0.156
P4-4uM	0.004	0.015	0.005	0.175
P4-8uM	0.007	0.027	0.004	0.141
P4-12uM	0.000	0.001	0.005	0.153
P4-20uM	0.017	0.079	0.004	0.119
P12-Ambient	0.001	0.003	0.002	0.049
P12-1uM	0.001	0.004	0.003	0.077
P12-2uM	0.001	0.002	0.002	0.070
P12-3uM	0.000	0.002	0.002	0.071
P12-4uM	0.005	0.023	0.003	0.068
P12-8uM	0.001	0.003	0.002	0.073
P12-12uM	0.012	0.056	0.003	0.077
P12-20uM	0.005	0.023	0.002	0.110
P16-Ambient	0.000	0.000	0.002	0.058
P16-1uM	0.001	0.008	0.002	0.110

P16-2uM	0.002	0.018	0.003	0.118
P16-3uM	0.000	0.002	0.002	0.105
P16-4uM	0.003	0.022	0.002	0.096
P16-8uM	0.001	0.007	0.003	0.104
P16-12uM	0.001	0.004	0.003	0.132
P16-20uM	0.011	0.100	0.003	0.102
P20-Ambient	0.002	0.001	0.003	0.061
P20-1uM	0.015	0.007	0.004	0.128
P20-2uM	0.032	0.019	0.004	0.142
P20-3uM	0.034	0.021	0.004	0.146
P20-4uM	0.037	0.025	0.003	0.123
P20-8uM	0.061	0.057	0.004	0.136
P20-12uM	0.067	0.066	0.005	0.139
P20-20uM	0.086	0.114	0.004	0.089
P26-Ambient	0.008	0.108	0.005	0.261
P26-1uM	0.010	0.134	0.005	0.273
P26-2uM	0.011	0.149	0.005	0.274
P26-3uM	0.013	0.172	0.005	0.280
P26-4uM	0.011	0.144	0.005	0.273
P26-8uM	0.015	0.214	0.005	0.273
P26-12uM	0.014	0.197	0.005	0.278
P26-20uM	0.017	0.242	0.004	0.233